Understanding the Static and Transient Behavior of Organic Electrochemical Transistors

Shin Ya Chen

A dissertation

submitted in partial fulfillment of the

requirements for the degree of

Doctor of Philosophy

University of Washington

2023

Reading Committee:

David S. Ginger, Chair

Dianne J. Xiao

Samson A. Jenekhe

Program Authorized to Offer Degree:

Molecular Engineering and Sciences

University of Washington

Abstract

Understanding the Static and Transient Behavior of Organic Electrochemical Transistors

Shin Ya Chen

Chair of the Supervisory Committee:
Professor David S. Ginger
Department of Chemistry

An organic electrochemical transistor (OECT) is a type of transistor with both ionic and electronic carriers involved in device operation. Recently, OECTs have emerged as promising candidates for both neuromorphic computing and biosensing applications as they exhibit direct response to biologically relevant ions, neurotransmitters, and metabolites. Moreover, the typically soft and flexible nature of organic semiconductors opens the possibility of the implementation of OECTs in both brain-machine interfaces and implantable biosensors. Nevertheless, deeper understanding of static and transient behavior of OECTs is necessary to unleash the full potential of OECTs for all the promising real-world applications aforementioned. Here, we first study the impact of the polymer side chain on the transconductance and the speed of OECT devices. Specifically, we show higher transconductance and faster kinetics if more polar function groups are on the side chain, or

if the polar functional group is farther away from the polymer backbone. Next, we elucidate why accumulation mode organic electrochemical transistors turn off much faster than they turn on, which is a phenomenon prevalent in published studies yet cannot be explained by existing models. We further identify that ion transport is limiting the device's operation speed and provide guides for engineering faster OECTs from both device and materials perspectives. Last, we synthesize new polymers and characterize their OECT performance. We verify that higher polymer crystallinity indeed reduces the OECT electronic carrier mobility. Together, these studies help to expand our understanding of the static and transient behavior of OECTs.

TABLE OF CONTENTS

LIST OF FIGURES

LIST OF TABLES

ACKNOWLEDGEMENTS

I would like to first express my gratitude to the members of my Supervisory Committee: Dr. David S. Ginger (chair), Dr. Chinmayee Subban, Dr. Dianne J. Xiao, Dr. Karl F. Bohringer and Dr. Samson A. Jenekhe. Their expertise, advice, and support have been invaluable throughout my scientific training.

I would also like to acknowledge my advisors throughout my PhD time, Dr. Qiuming Yu (now at Cornell University), Dr. David S. Ginger and Dr. Christine K. Luscombe (now at Okinawa Institute of Science and Technology). Under Dr. Yu's guidance, I had my first lesson on how to think like a trained scientist and completed my master's degree in molecular engineering at the University of Washington. Under both Dr. Ginger and Dr. Luscombe's supervision, my critical thinking and research skills were further polished, and my first author research work was successfully delivered. More importantly, I would like to express my gratitude again to Dr. Ginger and Dr. Luscombe for agreeing to become my advisors after I finished my master's degree and decided to continue my PhD journey, which happened to be the outbreak of SARS-CoV-2 pandemic, a very difficult time for everyone.

Thanks to all the current and former members in the Yu lab, Christine lab and Ginger lab who have overlapped my time here. Special thanks to Dr. Erjin Zheng (Yu lab) for fruitful discussions in my early year when I knew nothing and was trying to build and characterize the OECT, Dr. Jonathan

W. Onorato and Dr. Nadzeya A. Kukhta (Christine Lab) for teaching me organic synthesis and helping me troubleshooting my failed reactions, Prof. Connor G. Bischak, Dr. Lucas Q. Flagg, Prof. Dean A. Waldow, Ramsess Quezada and Dr. Rajiv Giridharagopal (Ginger lab) for fruitful discussions on OMIECs characterizations and experiment techniques including AFM and GIWAXS. Lastly, a big thank you to my Ginger lab partner, Jiajie Guo, much of the work could not have been accomplished without her help and suggestions.

Words cannot adequately express the depth of my gratitude for my family. Thanks to my parents, my grandparents, my sister, and my brother in law for their constant encouragement and understanding, which have made it possible for me to pursue my passion and achieve the milestone of completing my PhD.

Thanks to my amazing friends here, Jiajie, Hao, Rene, Gloria, Ethan, Erjing, Yangwei, Xudong, Fangyuan, Muammer, Luke, Changkun and many others for being my academic buddies, party buddies and game buddies. I am grateful for their presence in my life.

Lastly, I would like to thank my significant other, Huiyun, for taking good care of me all these years. She is always there for me, patiently supporting me through all the ups and downs. I still remember the time in my early years when I was struggling so much and she helped me troubleshoot my experiment designs, even though her major is in biology and knows little about transistors. Her constant belief in me, especially in the SARS-CoV-2 pandemic period, has given me the strength to finish my PhD.

DEDICATION

This dissertation is dedicated to my parents, Szu Hsien Chen and Ming Chuan Li.

Chapter 1. INTRODUCTION

1.1 MOTIVATION

Organic electrochemical transistors (OECTs) are currently being explored in numerous applications including bioelectronics,[1–4] logic circuit elements,[5,6] and neuromorphic devices.[7–10] These intriguing applications are possible thanks to OECT's features including high amplification capability, low operation potential,[11] flexible operation environments (electrolyte or gel)[2] and multiple conducting states.[12] Nevertheless, current understanding of the OECT operation mechanism is still limited, as the interplay between channel organic materials, electrons, ions, and solvent are complex. Redox reactions of channel polymer (key process of OECT operation) and the possible undesired side reactions (with water and oxygen involved) further increase the analysis difficulty. Here, we seek to understand the complex interactions between these factors in the hope that our findings will help the commercialization of OECT based applications one step forward.

Below describes the outline of the dissertation. In Chapter 1, the background of OECTs including the choice of channel material, electrochemical doping and dedoping of channel organic semiconductors and the OECT operation principles are introduced. In Chapter 2, we study the impact of the side chain structure on the OECT performance. In Chapter 3, we investigate the transient behavior of accumulation mode OECT devices. We then discuss the synthesis and characterizations of new OECT materials in Chapter 4. We summarize the findings and provide future directions in Chapter 5.

1.2 Organic Mixed Ionic-Electronic Conductors

Organic mixed ionic-electronic conductors (OMIECs) are organic materials with the capability of conducting both ionic and electronic carriers. OMIECs typically comprise an electron conducting motif and an ion conducting motif as shown in Figure 1.1. OMIECs could be accomplished by either blending organic semiconductors (often times π-conjugated polymers, hereafter refer as conjugated polymers) with ion conducting polymers, adopting block copolymer structure, or synthesizing conjugated polymers with ion conducting side chains. Film morphology may vary significantly with different strategies. To date, most of the OECT channel materials fall into the category of type I, II, V and VI in Figure 1.1. Type III and IV materials are relatively rare due to synthetic difficulty. In this dissertation, we mainly investigate OECT performance of type VI OMIECs.

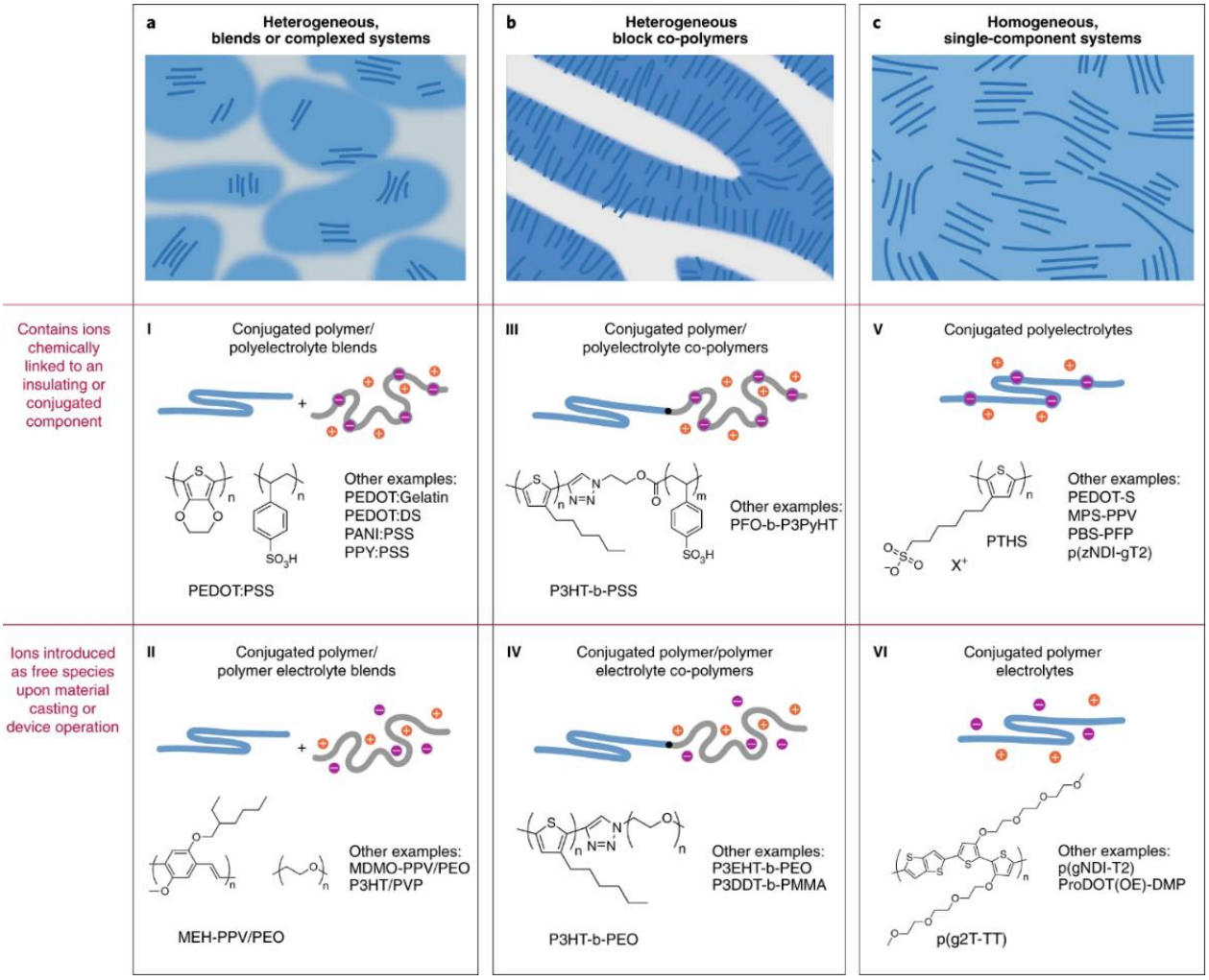

Figure 1-1. Material classes of OMIECs.

Adapted with permission.[13] Copyright 2019, Springer Nature.

Since the OMIECs conduct both ions and electrons, the processes involved in OMIECs could be categorized as electronic transport, ionic transport and ionic-electronic coupled interactions as shown in Figure 1.2. The conjugated structure of polymer backbone provides electronic transport, which occurs either through hopping or band-like transport. Electronic carrier hopping appears with relatively localized charge carrier and is the dominant electronic transport pathway in amorphous domain or in low doping regime (Figure 1.2.a). Band-like transport could occur when doping level increased and the charge carrier is relatively delocalized (Figure 1.2.b). When doping

level increased, both pathways are possible and thus the dependency of electronic carrier mobility on electronic carrier density (Figure 1.2.c). Ionic transports in OMIECs are possible through ion hopping via polar side chains, polymer solvation or Grotthuss mechanism (Figure 1.2 g-i). Ionic-electronic coupling describes the injected electronic carrier being compensated by the counterion to maintain the charge neutrality (Figure 1.2 d-e). Detailed description of charge injection and electrochemical doping of conjugated polymer could be found in section 1.3. Processes illustrated in Figure 1.2.a-c, d-e and g-h are closely related to the OECT operation.

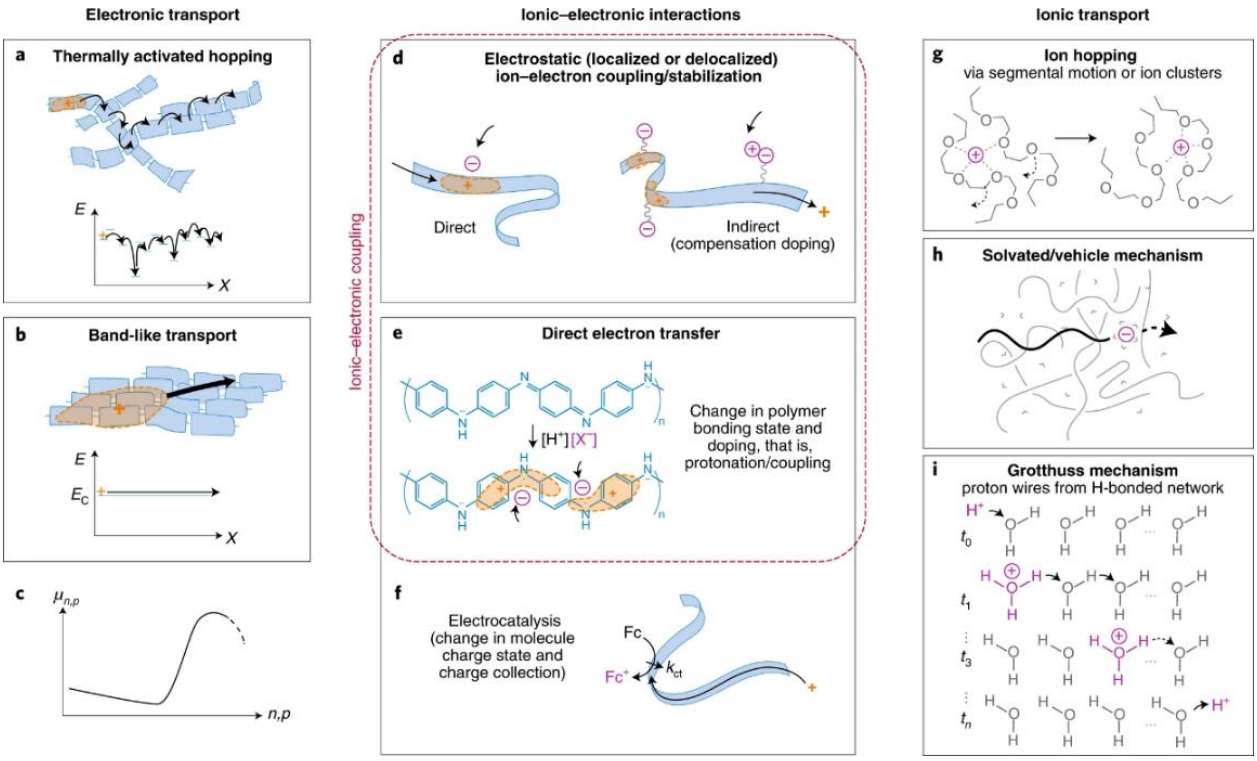

Figure 1-2. Processes in OMIECs.

Adapted with permission.[13] Copyright 2019, Springer Nature.

Figure 1.3 shows the typical configurations of OMIEC-based devices. Blue, yellow, and grey layers in the figure represent OMIECs, metal electrode (typically gold) and the substrate (commonly glass or silicon), respectively. The counter electrodes are typically Ag/AgCl pellet,

metal electrode or other OMIECs. OMIECs show great potential in applications including sensors, energy storage, display, and computing. In this dissertation, we will focus on OECTs and apply electrochemical impedance spectroscopy (EIS) and spectroelectrochemistry (similar to electrochromic) for characterizing OMIECs performance.

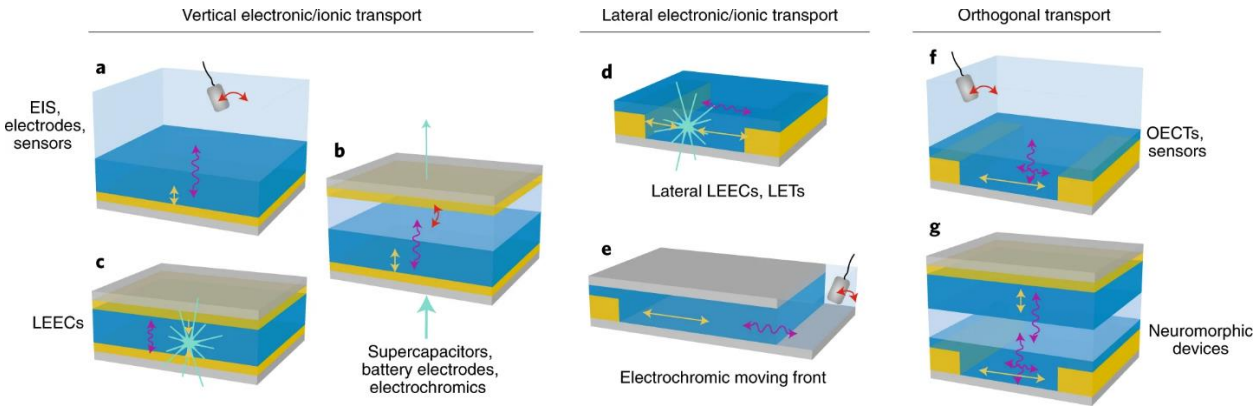

Figure 1-3. Typical configurations of OMIEC-based devices. Adapted with permission.[13] Copyright 2019, Springer Nature.

1.3 Electrochemical Doping of Organic Mixed Ionic-Electronic Conductors

Most OMIECs contain conjugated structure (alternated single and double bond) and fall into the category of organic semiconductors. The direct differences between insulators, semiconductors, and conductors (like metal) are bandgap (E_g) and conductivity (σ). Semiconductors typically have bandgap < 5eV and conductivity in the range of 10^{-7} ~ 10^{0} S/cm. More electrons could reach the conduction band and contribute to the conductivity with smaller bandgap. The number of electrons in the conduction band at a given temperature, or the distribution of the electronic carriers, is commonly described by Fermi-Dirac statistics. Figure 1.4 shows the bandgap of thiophene molecule(s) becomes smaller with increasing repeating unit (which could be described using molecular orbital theory), and the evolution from a relatively insulating material (a single thiophene unit) to a semiconducting material (three or more thiophene repeating units). As the bandgap becomes smaller, they start to absorb visible light and thus the solution switches from colorless to yellow and orange. Detailed discussions on Fermi-Dirac statistics and molecular orbital theory could be found in the textbook of semiconductor physics and general/physical chemistry, respectively.

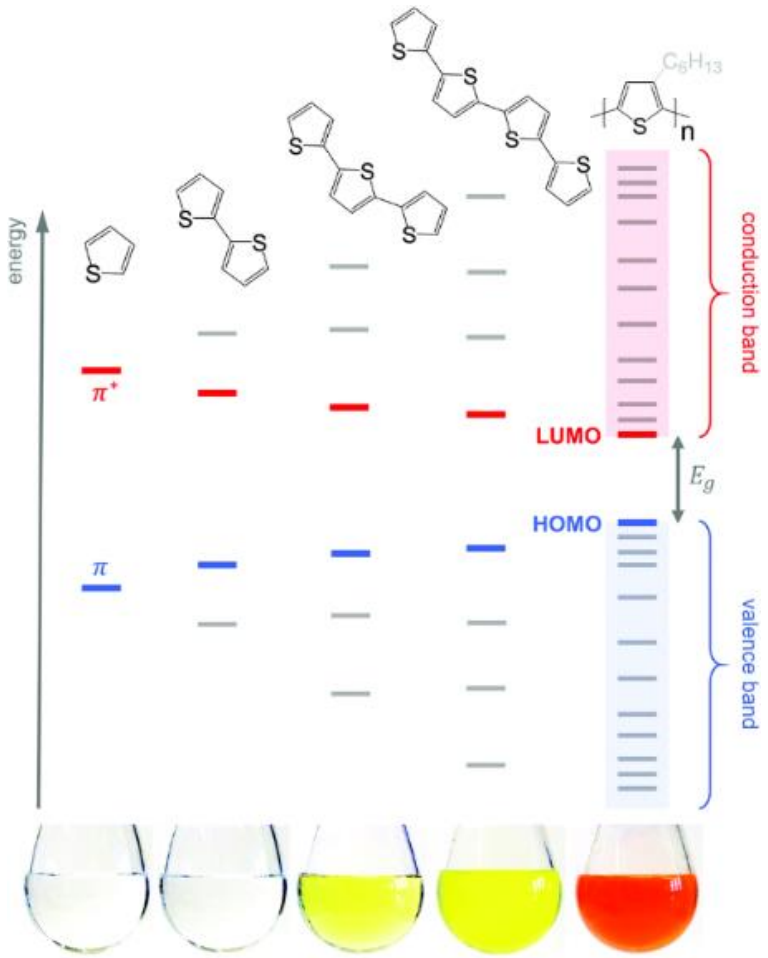

Figure 1-4. Evolution of the bandgap with increasing number of thiophene repeat units. Adapted with permission.[14] Copyright 2016 Royal Society of Chemistry.

Doping is an effective approach to increase the conductivity of semiconductors, with the semiconductors being oxidized (electron removed, p-doping) or reduced (electron added, n-doping). The generated electrons (n) or holes (p) increase the carrier density and thus the conductivity. In inorganic semiconductors like silicon, doping is typically achieved via thermal diffusion, ion implementation, chemical vapor deposition (CVD) or physical vapor deposition (PVD). For organic semiconductors, chemical doping (molecular doping/vapor doping) and electrochemical doping are the two most commonly used doping methods. Chemical doping is relatively straightforward for implementation and is suitable for applications like e-textiles or

thermoelectrics, where reversible doping/dedoping is not necessarily required. In contrast, electrochemical doping has the benefits of more easily controlled doping levels and capability of switching between different doping levels via potential. These features are especially intriguing for transistor and neuromorphic applications.

Figure 1.5 shows an example of p-type electrochemical doping of organic semiconductors (or conjugated polymer/OMIECs) in a two-electrode cell system. In the neutral state, ions mostly reside in electrolyte, with few/some entering the polymer film along with the solvent due to the film passive swell. Passive swelling level of polymer depends on the solvent-polymer compatibility. When the oxidation bias is applied, holes (at gold surface) and electrons (at Pt mesh surface) are induced, and the transport of anions and holes into the film starts to occur. When the oxidation bias is on hold and the system reaches steady, the holes injected into the film are compensated by the anions from the electrolyte to maintain charge neutrality, and the polymer (P) is oxidized: $P + h^+ \rightarrow P^+$. On the Pt mesh end, the induced electrons are compensated by the cations in the electrolyte. If a Ag/AgCl pellet is used instead of the Pt mesh, the following reaction occurs: $AgCl + e^- \rightarrow Ag + Cl^-$. Overall, p-type electrochemical doping of organic semiconductors (or conjugated polymer/OMIECs) involves these four steps (on the polymer end): (1) applying oxidative bias (2) anion injection and transport (3) hole injection and transport (4) hole compensated by anion. Importantly, the exact sequence of steps (2) - (4) are likely polymer and ion dependent and are poorly understood. We note that the solvent involved in electrochemical doping could be either water or organic solvents like acetonitrile. The major difference between these two solvents is ion solubility (i.e., KCl cannot be dissolved in most organic solvents) and the electrolyte potential window (water potential window is smaller). In most of the OECT studies to date, water is the choice of the solvent as most biological relevant ions are soluble in water.

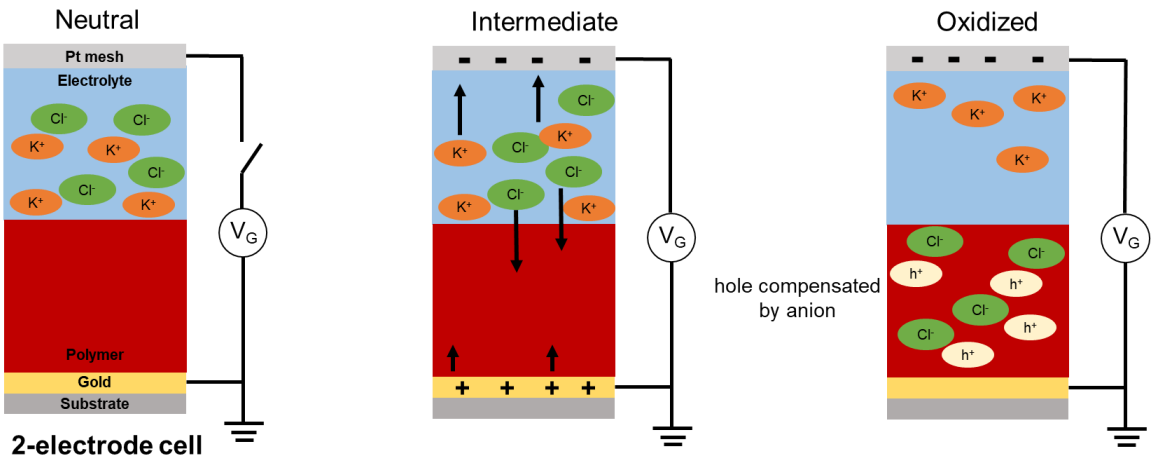

Figure 1-5. Schematics of electrochemical doping of organic semiconductors.

Figure 1.6 shows an example chemical structure and band struture change of p-doping of organic semiconductors (or conjugated polymer/OMIECs). Doping introduces new electronics states (polaron and bipolaron) in the bandgap of the polymer and narrows the bandgap. Polaron represents the electronic charge (i.e., injected hole) and the distortion of the polymer backbone. Bipolaron occurs typically in higher doping levels, where two injected electronic charges share the same distortion of polymer backbone.

Since the electrochemical doping of polymer involves changes including color (narrower bandgap), mass (injected ions and solvent), charge (injected electronic carrier), polymer ordering and film conductivity, techniques below are commonly used for electrochemical doping characterizations:

A. Color: UV-Vis and IR

B. Mass/thickness: QCM and AFM

C. Electronic charge: EIS and coulometry

D. Polymer ordering: XRD and GIWAXS

E. Conductivity: OECT and 4-line method

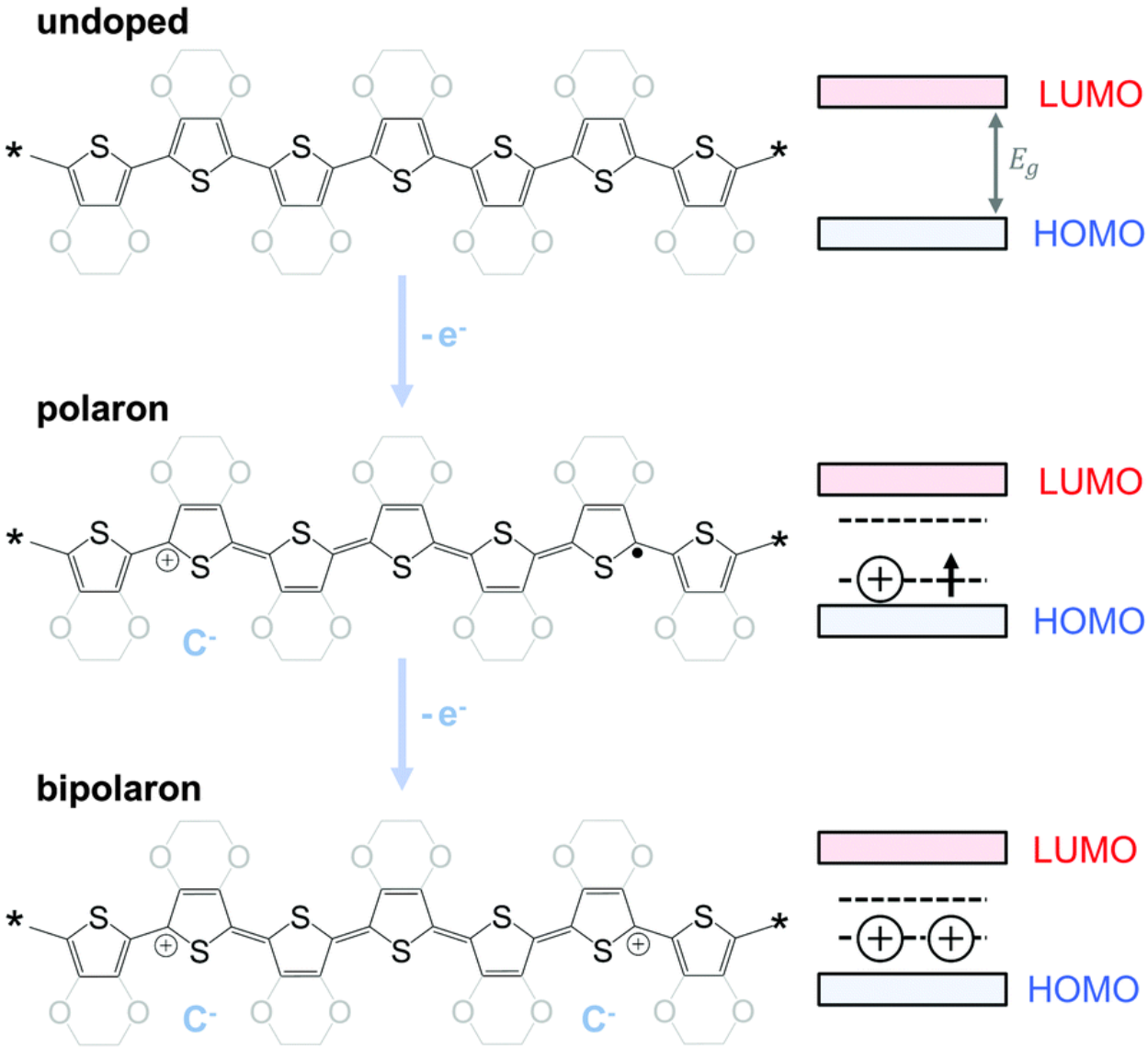

Figure 1-6. Schematic of p-type doping and the band structure evolution. Adapted with permission.[14] Copyright 2016 Royal Society of Chemistry.

1.4 Organic Electrochemical Transistors

OECT Device Architecture

Figure 1.7 shows the classic OECT device architecture (top gate / bottom contact). Similar to all transistors, OECT is a three-electrode device with source (grounded) and drain electrode connected by the channel material (OMIECs/organic semiconductors/conjugated polymers), and the gate electrode is immersed in the electrolyte. Akin to field-effect transistors (FETs), in OECTs, output current (drain current, I_D) is a function of voltage signal at gate (V_G), or the magnitude of I_D is controlled by V_G. A typical OECT has channel width (W), length (L) and thickness (d) to be 100 μm, 10 μm and 100 nm, respectively, and the thickness of bottom metal electrode (mostly gold/chromium or gold/titanium) is ~ 100 nm. Recently, new OECT device architectures including top gate / top contact, coplanar and vertical have emerged and showed promising features including claimed higher reproducibility (top gate / top contact),[15] applicable as planar bioelectronics (coplanar)[3,16] and smaller device footprint (vertical).[5,17–19] Appendix C and Appendix D show the OECT device fabrication protocol via photolithography and printing, respectively.

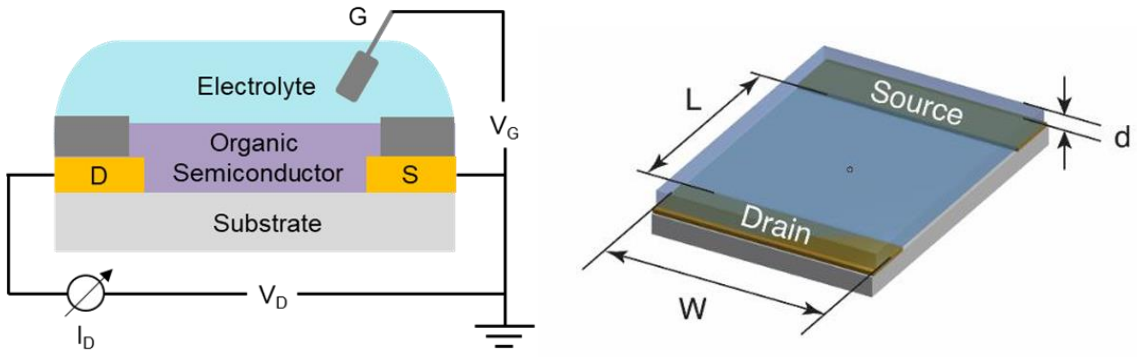

Figure 1-7. Side and top view of OECT device schematics.

OECT Operation Principle

The operation principle of OECT is described as follows: the magnitude of I_D, or channel conductivity of an OECT is modulated by the electrochemical gate potential, which controls the doping level (redox state) of the conjugated polymer channel. Importantly, in contrast to conventional FTEs, OECTs exhibit volumetric doping: the gate voltage changes the conductivity of the entire volume of the transistor channel, rather than just the surface layer (Figure 1.8), and counterions injected from the electrolyte provide charge compensation for injected electronic carriers.[20] We note that in reality, the boundary of electrolyte-gated OFET (EG-OFET) and OECT could be vague and depends on the choice of polymer, ion and operation potential as demonstrated by Laiho et al.[21] The other classical examples are transistor devices based on poly(3-hexylthiophene) (P3HT) or conjugated polymers with more hydrophobic side chains. These transistors exhibit volumetric doping and act as OECTs with bulky, chaotropic anions like $TFSI^-$ or PF_6^-. In contrast, with kosmotropic anion like Cl^-, these transistors show mainly interfacial doping or mixed interfacial/volumetric doping and act more like EG-OFETs.[22–25]

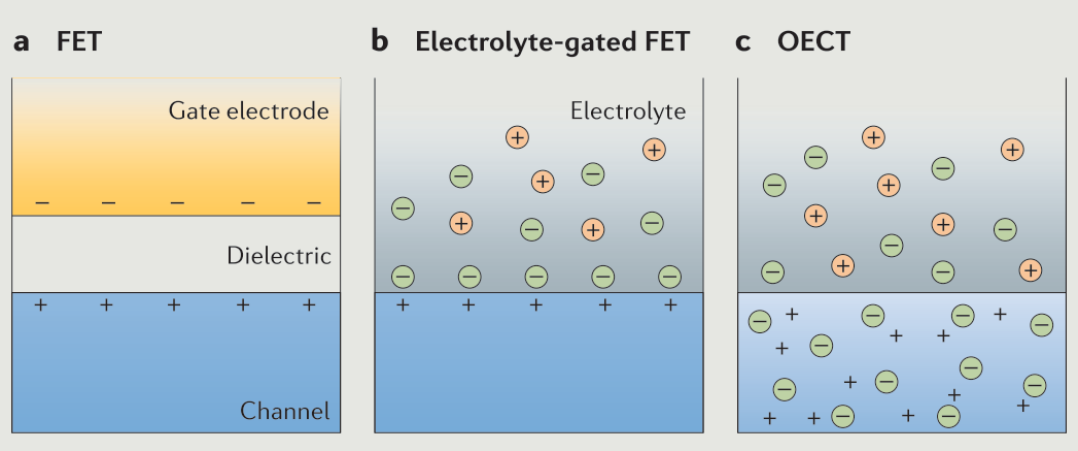

Figure 1-8. Comparison of transistor device schematics.
Adapted with permission.[26] Copyright 2017 Springer Nature.

Based on the OMIECs selection, OECT could operate in either depletion mode or accumulation mode (Figure 1.9). In depletion mode, the OMIECs are in doped state without gate bias applied (intrinsically doped), meaning it is in on-state when no gate potential applied. In contrast, the accumulation mode OECTs are turned on when gate potential is applied. Most of the OMIECs reported to date operated in accumulation mode, except poly(3,4-ethylenedioxythiophene):poly(styrene sulfonate) (PEDOT:PSS), which typically operates in depletion mode. PEDOT:PSS is one of the most used OECT materials since its commercial availability, relatively good stability and moderate OECT performance. From the application perspective, accumulation mode materials are sometimes more favorable because of their lower energy consumption, particularly for in vivo bioelectronics and neuromorphic computing.

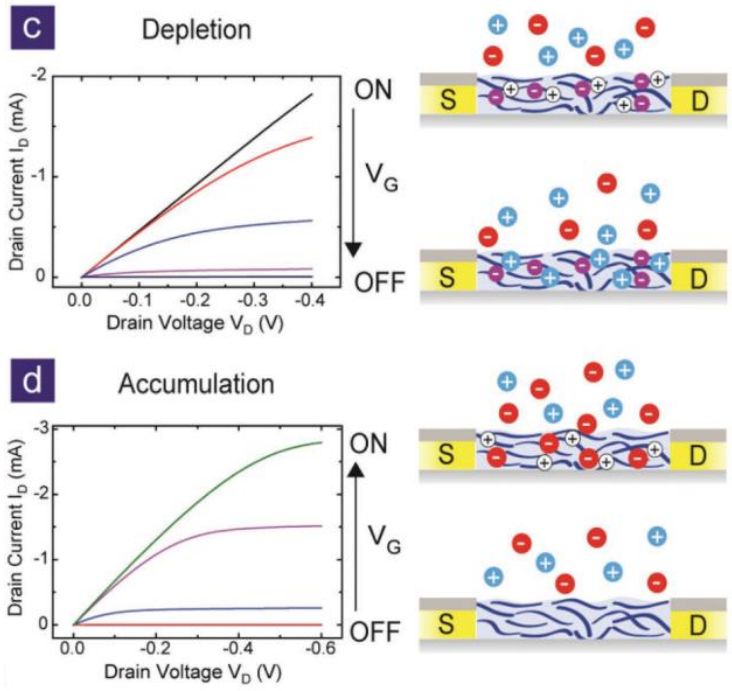

Figure 1-9. Comparison of OECT operation modes (p-type).
Adapted with permission.[27] Copyright 2018 John Wiley and Sons.

OECT Characterizations

To characterize the steady-state performance of OECT devices, output curve (Figure 1-10 A) and transfer curve (Figure1-10 B-C) are standard measurements similar to characterizing FETs. To compare the OMIECs performance as OECT materials without being affected by transistor dimensions or operation potentials, Inal and colleagues proposed using the product of electronic carrier mobility (μ) and the volumetric capacitance (C^*) as a steady-state figure of merit to evaluate different OECT materials.[28,29] The μC^* product captures the steady-state ionic/electronic transport process under device operation. The expected relationship between the μC^* product and g_m in the transistor saturation regime is given in Eq. 1:[28,29]

$$g_m \cong \mu C^* \cdot \frac{Wd}{L} \cdot (V_T - V_G) \ (Saturation) \qquad (1)$$

Figure 1-10 D shows the extraction of μC^* values by measuring the g_m of several OECTs and performing a linear regression between g_m and $(Wd/L) \cdot (V_G - V_T)$, as the channel width (W), length (L), channel active layer thickness (d), threshold voltage (V_T) and V_G are known. Threshold voltage extraction is demonstrated in Figure 1-10 B.

The product of electronic carrier mobility (μ) and the volumetric capacitance (C^*), μC^* and threshold voltage (V_T) are the crucial steady-state metrics when selecting OECT channel materials. In general, higher μC^* and lower $|V_T|$ are desired. An effective strategy to increase the material μC^* is to tether polar side chains like ethylene glycol onto the conjugated backbone to improve the C^*. Nevertheless, issues like lower mobility (trade-off between μ and C^*)[30,31] or poor operation stability[32] could occur if the polymer film is too hydrophilic. The state of art p-type OECT accumulation mode material, p(g2T2-g4T2) exhibits $\mu C^* \sim 522$ F $cm^{-1}V^{-1}s^{-1}$ and $V_T \sim 0.02$ V,[33]

while the state of art n-type OECT accumulation mode material, P(gTDPP2FT) exhibits μC^* ~ 42 F $cm^{-1}V^{-1}s^{-1}$ and V_T ~ 0.65 V.[34] The state of art p-type OECT depletion mode material, Crys-P(SE) exhibits μC^* ~ 1500 F $cm^{-1}V^{-1}s^{-1}$.[35] We note that there is no n-type OECT depletion mode material yet, likely related to the intrinsic instability of doped n-type organic semiconductors in the ambient condition. A complete μC^* and V_T values for the up to date OECT materials could be found in a recent review paper written by Tropp et al.[36]

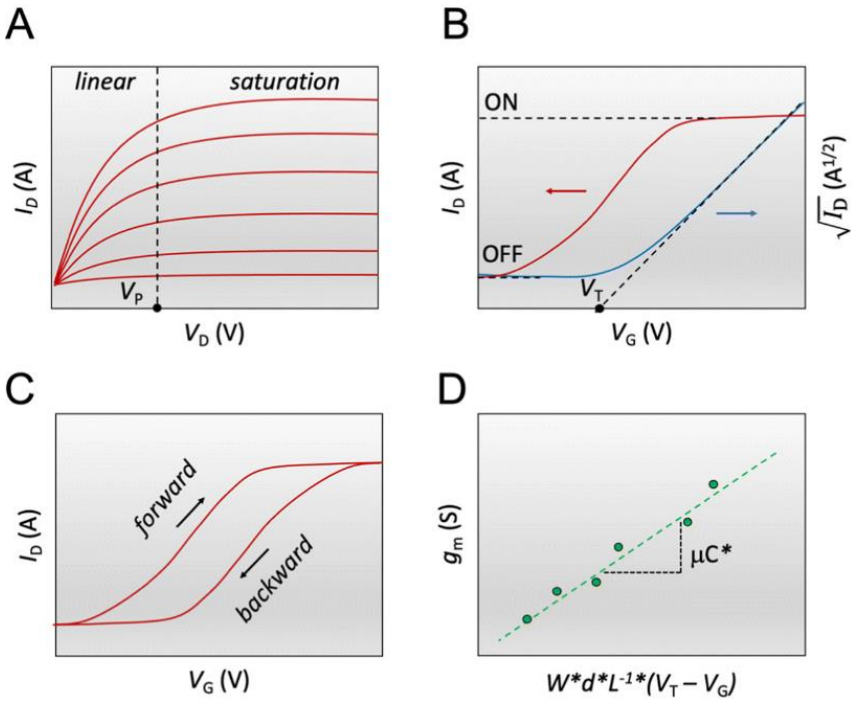

Figure 1-10. Steady-state OECT characterizations.
Adapted with permission.[19] Copyright 2023 Royal Society of Chemistry.

Figure 1-11 shows the transient OECT characterization. Based on the behavior of PEDOT:PSS OECTs (depletion mode), the pioneering Bernards model considers the transient behavior of an OECT as the characteristic of charging or discharging a capacitor.[37] Assuming

charging or discharging occurs uniformly along the channel polymer, they proposed that I_D to have a single exponential response when switching between two steady-states, as shown in Eq. 2:

$$I_D(t, V_G) = I_{ss}(V_G) + \Delta I_{ss}\left(1 - f\frac{\tau_e}{\tau_i}\right) \cdot e^{-t/\tau_i} \qquad (2)$$

where I_{SS} is the steady-state channel current, and ΔI_{SS} is the current difference between two different steady-states. f determines the ratio of I_{GS} and I_{GD}. τ_e is the electronic charge transit time and τ_i is the product of $R_S \cdot C_{Ch}$. The R_S is the electrolyte resistance and the C_{Ch} is the channel capacitance.[37] They demonstrated the I_D response to be either a monotonic decay or a spike-and-recovery depending on the ratio between $f\tau_e$ and τ_i, with device switching speed determined by τ_i (Figure 1-10 A).[37] We note that with Bernards equation, one would expect similar transistor turn-on and turn-off times.

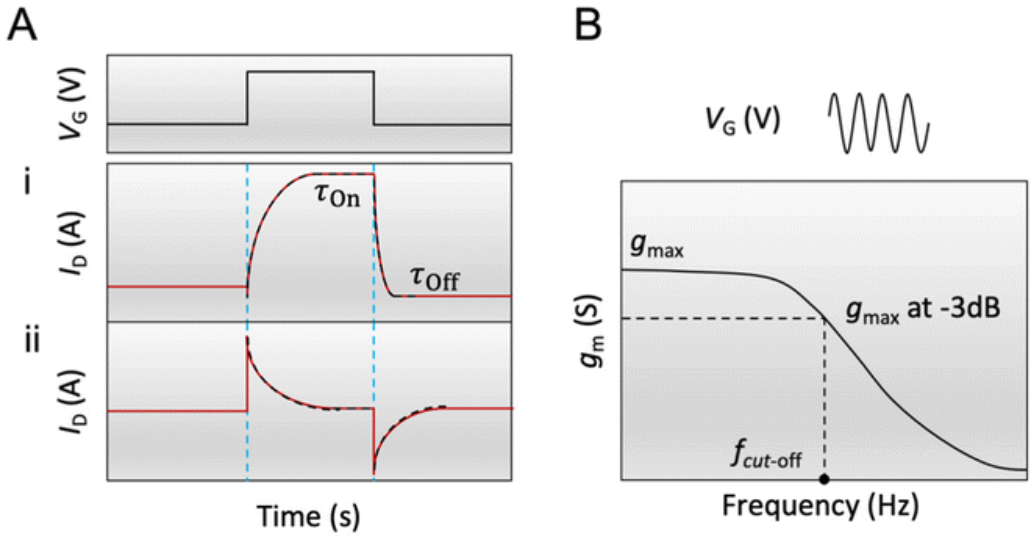

Figure 1-11. Transient OECT characterizations.
Adapted with permission.[19] Copyright 2023 Royal Society of Chemistry.

Figure 1-11 B shows the frequency characteristics of OECTs. When the applied gate potential is switched too fast between on and off states, i.e., $f > f_{cut\text{-}off}$, the transistor will not be able to response fully and thus results in lower transconductance. Rivnay et al first applied the impedance matching method to determine the OECT turn-on time ($\tau_{on} = 1 / 2\pi f_c$).[38] Impedance matching method has been relatively rare reported when characterizing OECT transient behavior, though it is standard for other types of transistors like FETs.

In general, current understanding of the OECT transient behavior is lagging behind compared to the steady-state behavior. Notably, operation speed could be dramatically different for materials with similar μC^*.[39] Comparing the operation speed of OECT materials in the published studies could be complex and difficult due to several reasons: (1) The operation speed is doping level dependent yet there is no universal standard for what the " on-state doping level" is. (2) Device dimension (W, d & L), distance between gate and channel, and overlap area between polymer and metal electrode could all affect device operation speed. (3) Potential different transient behavior for the same material in different cycles due to either film hydration or cycling instability. (4) OECT operation speed is ion concentration and ion species dependent, yet there is no standard electrolyte when testing operation speed. Common electrolytes are 0.1 M NaCl, 0.1M KCl and 1X PBS buffer. (5) Some studies only report the device turn-on time. We expect more exciting works in the field to come and elucidate the complex OECT transient behavior.

Detailed descriptions of other common OECT channel material characterization techniques including electrochemical impedance spectrum (EIS, for C^*), quartz crystal microbalance with dissipation and electrochemistry module (eQCM-D, for swelling),[40] moving front experiments and AFMs (for ion mobility and ion motion), and spectroelectrochemistry (SpecEChem, for doping level and electronic band structure) could be found in reviews by Ohayon et al.[19] and Wu et al.[41]

Summary

To sum up, a brief introduction on OECT device architectures, OECT operation principle and OECT characterizations are presented in this section, which are closely relevant to the dissertation content. Other interesting and important topics including OECT device cycling stability[42] and OECT applications[4,26,27] could be found in recent OECT reviews.

1.5 SUMMARY

In Chapter 1, we first introduce OMIECs, which are organic materials that conduct both ions and electrons and could be used as OECT active layers. We then discuss the electrochemical doping of organic semiconductors, in which electronic carriers are injected into organic semiconductors when oxidation/reduction potential is applied. Electrochemical doping of organic semiconductors is the most crucial process of OECT operation. Last, a brief description on OECT device architectures, OECT operation principle, and OECT characterizations are presented. We hope this information is sufficient to help readers to understand the following three original research works in Chapter 2, Chapter 3 and Chapter 4.

Chapter 2. IMPACT OF VARYING SIDE CHAIN STRUCTURE ON ORGANIC ELECTROCHEMICAL TRANSISTOR PERFORMANCE: A SERIES OF OLIGOETHYLENE GLYCOL-SUBSTITUTED POLYTHIOPHENES

Adapted with permission from S. E. Chen, L. Q. Flagg, J. W. Onorato, L. J. Richter, J. Guo, C. K. Luscombe and D. S. Ginger, J. Mater. Chem. A, 2022, 10, 10738[25]. Copyright 2022 Royal Society of Chemistry.

2.1 INTRODUCTION

Conjugated polymers with mixed ionic-electronic conduction properties, or organic mixed ionic-electronic conductors (OMIECs), are promising materials being explored in the fields of bioelectronics,[1,3] neuromorphic computing,[9,43] and energy storage.[44] In the field of bioelectronics and neuromorphic computing, organic electrochemical transistors (OECTs) provide a device configuration that can transduce small changes in an ionic flux into large changes in electrical current.[26,27,45] An OECT is a three-terminal device with source and drain electrodes connected by a channel active layer (conjugated polymer), and with an electrolyte solution in between the channel active layer and the gate electrode. The working principle of an OECT (in accumulation mode) involves the injection of polarons from the source electrode into the channel driven by the gate potential bias (V_G) and a concomitant change in electrolyte balance in the polymer film (both anion injection and cation expulsion for p-type material) to maintain charge neutrality.[20] This coupled process of electrochemical charging (commonly referred to as "electrochemical doping") results in the volume of the polymer film filled with charged polarons, which are in turn charge-compensated by ions from the electrolyte. The density of electronic carriers (polarons) in the active

channel, and hence the magnitude of the electrical current that flows through the channel (I_D) is modulated by V_G. The resulting change in drain current I_D that is achieved by a given change in V_G is reported as the transconductance ($g_m \equiv \boldsymbol{\partial I_D / \partial V_G}$). As a class of transistors, OECTs offer several attractive properties including high g_m (≈ mS), low device operation voltages (< |1 V|), and the ability to transduce ionic action potentials (voltages) in biological environments ranging from neurons in the brain[4,26] to carnivorous plants.[2]

To compare the performance of different OMIECs as an OECT active layer in a manner that is unaffected by factors such as transistor device geometry and operation voltage, Inal and colleagues proposed using the product of electronic carrier mobility (μ) and the volumetric capacitance (C^*) as a figure of merit to evaluate different OECT materials.[28,29] The μC^* product captures the steady-state ionic/electronic transport process under device operation. The expected relationship between the μC^* product and g_m in the transistor saturation regime is given in Eq. 1:[28,29]

$$g_m \cong \mu C^* \cdot \frac{Wd}{L} \cdot (V_T - V_G) \qquad (1)$$

The value of μC^* can thus be extracted by measuring the g_m of different OECTs and performing a linear regression between g_m and $(Wd/L) \cdot (V_G - V_T)$, as the channel width (W), length (L), channel active layer thickness (d), threshold voltage (V_T) and V_G are known. The μC^* of the classical OECT material Poly(3,4-ethylenedioxythiophene): polystyrenesulfonate (PEDOT:PSS) without any pre or postprocessing is ≈ 50 F cm^{-1} V^{-1} s^{-1}.[29] This is a relatively high value that results from a combination of high electronic mobility and moderate volumetric capacitance. PEDOT:PSS is the most widely used OECT material because of its commercial availability, operational stability and

relatively high OECT performance. Typically, an OECT with PEDOT:PSS active layer is operated in depletion mode, meaning the I_D is at on-state when no V_G applied. Depletion mode OECT is less desirable in applications requiring low-power consumption.

Over the last few years, researchers have been searching for new polymers with improved OECT performance.[13,46] Desirable targets include materials with high μC^* products,[33,47–49] those that can operated in accumulation mode,[33,50–52] and those that show faster kinetics.[43,53,54] Among different synthetic approaches, the strategy of modifying the polymer side chains has been applied extensively on different conjugated backbones with the goal of realizing new OMIECs that operate as accumulation mode OECTs with μC^* comparable to or higher than PEDOT:PSS. Notably, conferring conjugated polymers with fully glycolated side chain has become a ubiquitous strategy to enable higher μC^*.[33,55–57]

Previously, we compared the OECT performance of a polythiophene with fully alkylated side chain, poly(3-hexylthiophene-2,5-diyl) (P3HT), and a polythiophene with fully glycolated side chain, poly(3-{[2-(2-methoxyethoxy)ethoxy]methyl}thiophene-2,5-diyl) (P3MEEMT).[24] While P3MEEMT shows a higher μC^* product than P3HT, the mobility of P3MEEMT, like other polymers with ethylene glycol side chains, showed a complex relationship between polymer crystallinity, dry hole mobility, and hole mobility in the hydrated OECT.[24,52,58] Thus, given the known trade-offs between morphology, ion injection, and carrier mobility,[59] it is interesting to consider if there is room to compromise between degree of hydration and crystallinity, to achieve a beneficial compromise between the large volumetric capacitance and favorable kinetics achievable with readily hydrated polymers with high ethylene glycol (EG) content, and favorable ordering and hole mobility of hydrophobic P3HT with only alkyl chains.

Recently, Luscombe and co-workers reported the synthesis of a related family of polythiophenes with varying degrees of ethylene glycol (EG) content in the side chains, as well as varying positions that are suitable for testing this hypothesis.[60] They characterized the performance of these materials as polymer electrolytes for Li-ion batteries, hypothesizing that ionic, electronic, and balanced conduction could be improved by meticulously varying EG unit content and position in the polythiophene side chain. They found further that both ionic and electronic conductivity could be improved by increasing the oxygen atom distance from the polythiophene backbone.[60] Here, we explore the performance of these materials in OECT applications, with the goal of testing if it is possible to achieve a more optimal compromise between volumetric capacitance, kinetics, and carrier mobility in hydrated OECTs. Specifically, we test the OECT performance of three reduced-oxygen-content side chain polymers in both chaotropic and kosmotropic electrolytes and compare the results to the aforementioned reference polymer, P3MEEMT. This study emphasizes the very different nature of OMIECs operated in dry and hydrated states and bridges the gap between our understanding of conjugated homopolymers with pure alkyl and fully glycolated side chain in terms of their OECT performance.

2.2 Results and Discussions

2.2.1 OECT Device Performance

We first studied the performance of the reduced-oxygen-content side chain polymers in OECTs. Figure 2-1a shows the OECT device structure used for testing. Figure 2-1b shows the chemical structures of the reduced-oxygen-content side chain polymers studied. Poly(3-(methoxyethoxybutyl)thiophene), or P3APPT, has two oxygen atoms on the side chain farther from the polythiophene backbone. Poly(3-(methoxyheptyl)thiophene), or P3AAPT, possesses one oxygen atom on the side chain farther from the polymer backbone. Poly(3-(heptoxymethyl)thiophene), or P3PAAT, has one oxygen atom on the side chain closer to polythiophene backbone. The polymers were synthesized via Kumada Catalyst Transfer Polymerization (KCTP), and all polymers have similar number average molecular mass ($M_n \approx 10$ kg/mol), degree of polymerization (DP ≈ 50) and dispersities (Đ < 2). Table 2-1 summarizes the polymer properties. The details of the polymer synthesis have been described previously.[60] Figure 2-1c and Figure 2-1d show the typical OECT transfer curves (W = 4000 μm, L = 10 μm) in KCl and KPF_6 solutions, respectively. We measured for V_G only up to -0.7 V (vs. Ag/AgCl) because exceeding this value could lead to rapid device degradation and even water electrolysis. P3APPT, with two oxygen atoms on the side chain, exhibits higher I_D and g_m compared to P3AAPT and P3PAAT in both KCl and KPF_6 solutions. This result indicates that more oxygen content on the side chain results in better OECT performance. Interestingly, comparing the polymers with only one oxygen per side chain, P3AAPT shows a higher I_D and g_m compared to P3PAAT in KPF_6 solution, indicating that an oxygen atom farther from the polymer backbone is more beneficial for OECT operation. Both P3APPT and P3AAPT OECT devices demonstrate higher I_D and g_m when measured with the chaotropic PF_6^- anion compared to the kosmotropic Cl^- anion, a result which is

in agreement with our previous studies.[23,24] We did not observe any OECT performance of P3PAAT in KCl solution: the magnitude of I_D measured was equivalent or smaller than the gate current (I_G) (Figure A2a). This result means barely any current flows through the channel (from source electrode to drain electrode), and the device is not yet turned on. We believe that the inability to observe transistor behavior of P3PAAT with KCl as the electrolyte is because, in that case, the |threshold voltage| is > 0.7 V (vs Ag/AgCl), such that material degradation or water electrolysis occurs before the device turns on. In contrast, with a lower threshold voltage, P3PAAT becomes a working OECT device with KPF_6 (Figure A2b). This result again emphasizes the importance of the choice of counterion for OECT operation.

To compare the performance of polymers with reduced oxygen content on the side chains to the reference polymer, P3MEEMT, we calculated the μC^* of polymers in both electrolytes using Eq. 1. Figure A3 shows the resulting μC^* fitting results while Figure A4 and Figure A5 show the output curves and confirm that the transfer curves were measured in the saturation region (V_D = -0.6 V), and it is thus feasible to apply Eq. 1 to compute μC^*. We noticed that the max g_m was not reached in KCl solution prior to the onset of irreversible electrochemical processes around ≈ -0.8 V (vs. Ag/AgCl). To maintain a fair comparison, we calculated μC^* with g_m obtained at $|V_G| - |V_T|$ ≈ 0.13 V for all cases. Figure 2-2a shows the μC^* of four polymers in both KCl and KPF_6 solutions. With the kosmotropic Cl^- anion, we found that μC^* is very sensitive to both side chain oxygen content and position. We show that there is a positive correlation between μC^* and side chain oxygen atom content in KCl solution. For the chaotropic PF_6^- anion, we observed a similar μC^* trend as with the Cl^- anion, albeit with less sensitivity of the μC^* value to the side chain oxygen content, a result which could be explained by the more hydrophobic nature of the PF_6^- anion. We also noticed that a higher μC^* was obtained with the chaotropic PF_6^- anion compared to

kosmotropic Cl^- anion for all four polymers. Overall, we show higher μC^* with more oxygen atoms on the side chain, or if the oxygen atom is farther from the polymer backbone in both KCl and KPF_6 solutions.

Previously, Luscombe and co-workers have demonstrated that P3APPT, as polymer electrolyte for LiTFSI salt, exhibits higher electronic conductivity and comparable ionic conductivity to fully-glycolated P3MEEMT.[60] The fact that P3MEEMT is still a better OECT active layer with higher μC^* compared to P3APPT indicates the very different nature of polymer/ion interaction in dry and hydrated states. And it is thus necessary to apply different design strategy for various OMIECs applications.

Figure 2-2b shows the threshold voltage (V_T) of the polymers in both solutions while Figure A6, Figure A7 and Figure A8 show the determination of V_T. To measure V_T, we took the intersection of the tangent line of plots of $\sqrt{\boldsymbol{I_D}}$ curve (with maximum slope) and the x-axis in the $\sqrt{\boldsymbol{I_D}}$ vs. V_G plots. A smaller $|V_T|$ is generally preferred for accumulation mode OECTs as the device can be turned on at lower gate voltage. Interestingly, we found the V_T of P3MEEMT, P3APPT and P3AAPT are all ≈ -0.56 V (vs Ag/AgCl) with Cl^- as the counterion. When replacing the Cl^- with PF_6^-, we observed the expected decrease of V_T for all three polymers. In addition, we found an even lower V_T of P3APPT and P3AAPT compared to P3MEEMT with PF_6^- counterion. One possible explanation is the higher crystallinity of P3APPT and P3AAPT films in the undoped state compared to P3MEEMT,[60] which enables easier hole injection to start electrochemical doping process. While with Cl^- anion, which has higher hydration number and is very sensitive to side chain hydrophilicity during doping, we hypothesize that opposite factors are at play: easier polaron injection because of the higher film crystallinity at undoped state (lower V_T), but harder Cl^- anion injection due to the lower side chain hydrophilicity (higher V_T). And the V_T of P3MEEMT,

P3APPT and P3AAPT are thus all similar in KCl solution. Overall, our results clearly demonstrate that V_T is sensitive to both counterion and polymer side chain hydrophilicity, and that using the chaotropic anions (PF_6^- and $TFSI^-$) lowers the V_T compared to the kosmotropic Cl^- anion.

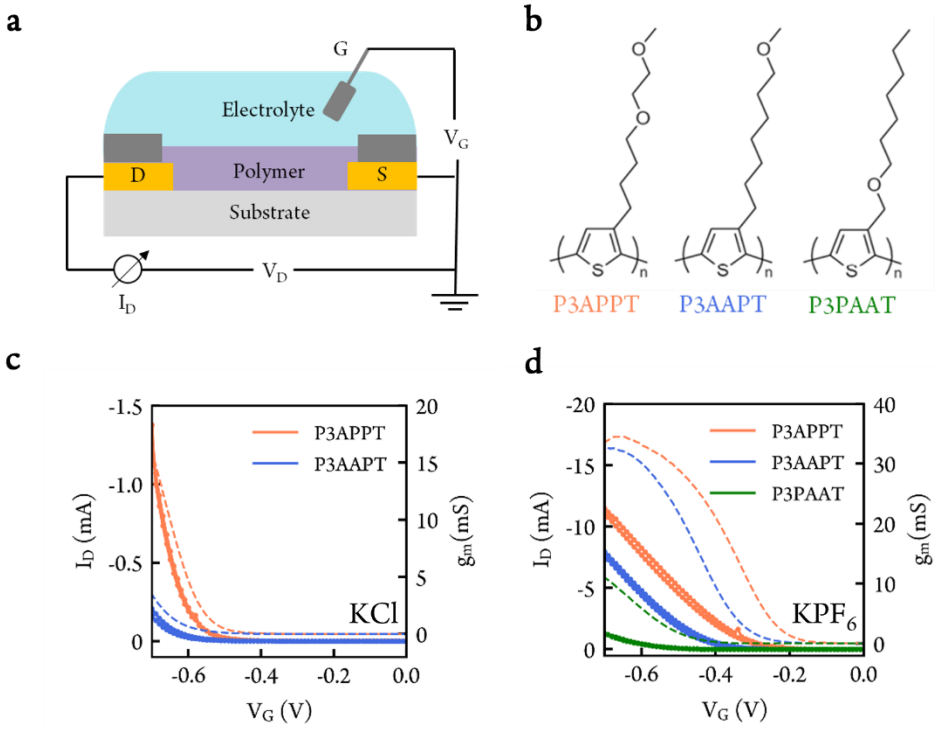

Figure 2-1. OECT performance of polymers.

(a) OECT device schematic. S and D represent source and drain electrode, respectively. An insulating layer (dark grey) was applied on top of gold electrode to prevent direct contact between gold and electrolyte. A Ag/AgCl pellet was used as gate electrode (G). (b) Chemical structure of reduced-oxygen-content side chain polymers. An example OECT transfer curve (dot line) and transconductance (dash line) of reduced-oxygen-content side chain polymers in 100 mmol/L (c) $KCl_{(aq)}$ and (d) $KPF6_{(aq)}$. Transistor channel width/length = 4000 μm /10 μm. V_D = -0.6 V for all measurements.

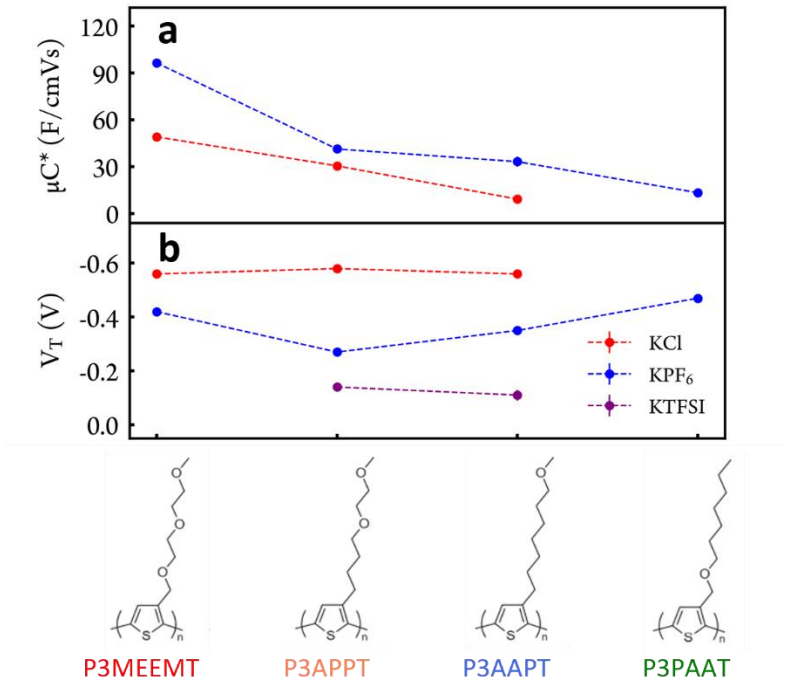

Figure 2-2. Polymer μC^* and V_T comparison.

(a) OECT material figure of merit μC^* and (b) OECT threshold voltage (V_T) in 100 mmol/L $KCl_{(aq)}$ (red), $KPF_{6(aq)}$ (blue) and KTFSI (purple). Dash lines are guide for the eye.

Table 2-1. Polymer Properties

	P3MEEMT	P3APPT	P3AAPT	P3PAAT
M_n (kg/mol)	11.2	10.5	12.4	9.1
Đ	1.46	1.51	1.38	1.91
Optical gap (eV) [a]	2.07	1.92	1.89	2.22
Film thickness (nm)	≈ 80	≈ 77	≈ 95	≈ 94

a. See Figure A1.

2.2.2 EIS and QCM-D Characterizations

To understand the reason behind the observed μC^* trend, we next utilized electrochemical impedance spectroscopy (EIS) to measure the volumetric capacitance C^* of the polymers. Briefly, the impedance of the polymer (gold/polymer/electrolyte) was measured through a small alternating current (AC) perturbation applied on top of a constant direct current (DC) doping bias. The impedance results were then fitted to an equivalent circuit, and the C^* was determined as the capacitor value divided by the polymer film volume. Figure A9 and Figure A10 show Nyquist plots and Bode plots of all four polymers in both KCl and KPF_6 solutions, respectively. For the reference P3MEEMT polymer, we observed only one quarter-circle in the Nyquist plot (Figure 2-3b) and one phase peak (at ≈ 1 Hz) in the Bode plot (Figure 2-3b). This result indicates only one capacitor component in the system, and a simplified Randles circuit (Figure 2-3a) is adequate to describe the polymer/electrolyte system.[61,62] In a simplified Randles circuit, resistance 1 (R_1) and resistance 2 (R_2) are usually interpreted to represent the solution resistance and polymer resistance, while CPE_1 represents the counterion-polaron pairs either throughout the bulk polymer film (i.e. volumetric capacitance in an OECT) or at the polymer/electrolyte interface (i.e., double layer capacitance in an electrolyte-gated organic field-effect transistor).[26] Note that we used a constant phase element (CPE) instead of a pure capacitor in the equivalent circuit. CPE is a common equivalent electrical circuit component representing an imperfect capacitor. More details about the use of the CPE and the conversion of the CPE to capacitance is described in supplemental information.

As the side chain hydrophilicity decreases, we begin to recognize two quarter/semi-circles in the Nyquist plots and two phase peaks in the Bode plots for P3APPT and P3AAPT in both KCl and KPF_6 solutions (Figure 2-3c, Figure 2-3d, Figure A9 and Figure A10). We thus applied the

Kovac's circuit (Figure 2-3a) as the equivalent circuit because of the existence of two capacitor components in the system.[62,63] CPE_2 is typically 1 to 2 orders of magnitude larger than CPE_1 in our results. The position of the CPE_2 phase peak is smaller than 1 Hz, while the position of CPE_1 phase peak is typically larger than 100 Hz. We used CPE_2 for further C^* calculations. The two capacitor components could indicate "the inhomogeneous counterion-polaron pair formation" phenomenon proposed for polymer/electrolyte systems. One possible explanation of this phenomenon is that both double layer capacitance (interfacial doping) and volumetric capacitance (volumetric doping) coexist in the polymer/electrolyte system of some range of conditions.[21,59] This situation could arise if domains with different hydrophilicity and stiffness existed in the polymer film. The interfacial doping occurs in more hydrophobic and stiffer region, while the volumetric doping appears in more hydrophilic and softer domain, and CPE_1 and CPE_2 represent double layer capacitor and volumetric capacitor, respectively. The 1 to 2 order(s) of magnitude difference between CPE_1 and CPE_2 supports the theory.

Alternatively, CPE_1 might represent counterion-polaron pairs formed at the crystallite/amorphous interface while CPE_2 could represent counterion-polaron pairs formed within crystalline domains when ions penetrate the crystallites at lower frequency. Previously, Thomas et al. have suggested electrochemical doping (formation of counterion-polaron pair) of poly(3-hexylthiophene) (P3HT) starts first at the crystallite/amorphous interface, followed by ion injection into the crystallites and eventually doping occurred within the crystallites.[64] Guardado et al. demonstrated counterions only penetrate the P3HT crystallites at lower frequency and tend to stay in the amorphous regions at higher frequency.[65] This explanation makes sense with the context of our data. For the reference polymer, P3MEEMT, because ions can penetrate the crystallites and approach the polymer backbone more easily due to its more hydrophilic side chain, the doping of

P3MEEMT tends to occur simultaneously at crystallite/amorphous interface and within crystallites. And thus, only one capacitor component (CPE_2) is observed. As the side chain hydrophilicity decreases, the reduced-oxygen-content side chain polymers behave more like P3HT, and the doping tends to be faster at crystallite/amorphous interface, and slower within crystallites. Our previous study supports this hypothesis and shows the P3MEEMT lamellar spacing expands already when in contact with aqueous solution (easier for ion injection), while P3HT lamellar spacing only expands after a doping bias applied.[24]

For P3PAAT in KPF_6 solution (Figure A9h and Figure A10h), we also observed two capacitor components in the impedance spectrum. In contrast, for P3PAAT in KCl solution (Figure A9g and Figure A10g), we found only one smaller capacitor component with a phase peak at ≈ 100 Hz (CPE_1), indicating either only double layer capacitance exists in the polymer/electrolyte system or only counterion-polaron pairs mainly at crystalline/amorphous interface exist. We note that similar C^* results were obtained from fitting the wider range of impedance spectrum (10^5 Hz to 10^{-1} Hz) with Kovac's circuit (this work) and from fitting the impedance spectrum only at lower frequency (10^1 to 10^{-1} Hz) with RC (or R-CPE) circuit. The latter method has been commonly used in the literature.[50,66]

Figure 2-4a shows the volumetric capacitance (C^*) of polymers in KCl, KPF_6 and KTFSI solutions as determined via the EIS fits to the Kovac's equivalent circuit show in Figure 2-3, Figure A9, Figure A10 and Figure A11. The C^* is obtained at a fixed potential above threshold ($|V_{doping}| - |V_T|$) of 0.13 V (vs. Ag/AgCl) for all cases. For the kosmotropic Cl^- anion, we found C^* is very sensitive to oxygen content and position on the side chain: we obtain larger C^* values where there are more oxygens on the side chain, or if the oxygen atom is farther from polythiophene backbone. Consistent with previous reports for hydrophobic polymers like P3HT,[23,67] we find that using more

chaotropic anions like PF_6^- and $TFSI^-$ results in higher C^* overall. While the use of chaotropic anions decreasing the overall sensitivity of the C^* to the side chain structure, the same general trend holds, with P3MEEMT having the highest C^* and P3PAAT having the lowest C^*, regardless of the counter anion species. Figure A12 shows the charge injected in each polymer during three consecutive cyclic voltammetry (CV) scans in both KCl and KPF_6 solutions. Figure A13 shows the positive correlation between C^* and normalized charge injected during CV scan and verifies the C^* trend shown in Figure 2-4a. Table A1 summarizes the V_T and C^* results of P3APPT and P3AAPT in 100 mmol/L $KTFSI_{(aq)}$.

We further measured passive swelling of the polymers via quartz crystal microbalance with dissipation mode (QCM-D). Passive swelling tracks the polymer film thickness change upon in contact with aqueous solution (with no potential bias applied). We followed a standard procedure commonly used in the field.[33,58,68] In brief, the mass change of polymer film in between air and aqueous solution is determined from the vibrational frequency change of the quartz crystal using the Sauerbrey equation.[69] Figure 2-4b shows the passive swelling level of all four polymers in deionized (DI) water. We did not observe significant differences between the passive swelling levels for the polymers in DI water, in KCl, or in KPF_6 solutions. P3MEEMT has the highest passive swelling level (≈ 121 %), which agrees with our previous measurement through atomic force microscopy (AFM) ($105 \pm 30\%$).[24] P3APPT (≈ 55 %) and P3AAPT (≈ 57 %) have similar passive swelling levels. P3PAAT exhibits the lowest passive swelling (≈ 14.5 %). Comparing the passive swelling levels of P3AAPT and P3PAAT, it is clear that the oxygen atom on the farther end of side chain enables more water molecules to diffuse into polymer film, in spite of the higher crystallinity of P3AAPT compared to P3PAAT.[60] This result agrees with the previous MD and dry film studies, as an extended solvation domain is created due to the cooperative effect between the

EG units on the farther end of side chain of the adjacent polymer backbones.[60] Notably, the passive swelling level is correlated to the C^* in this family of polymers, which is reasonable as more anions could migrate into the film and compensate the polaron if larger solvation domains exists in the polymer film.

Figure 2-4c shows the water contact angle results of the four polymers. We found the trend of water contact angle agrees with the trend of passive swelling level, and is anticorrelated with C^* when using Cl^- anion. Among the four polymers, P3MEEMT is the most hydrophilic polymer with the lowest water contact angle ($46.51 \pm 3.66°$) and P3PAAT is the most hydrophobic polymer with the highest water contact angle ($101.53 \pm 2.14°$). The water contact angle of P3APPT ($71.37 \pm 0.32°$) and P3AAPT ($77.10 \pm 4.16°$) are similar. Figure A14 shows the contact angle measurement images of the four polymers.

Comparing the trends of μC^* and C^*, we conclude that the C^* is the dominant factor controlling the variation of OECT figure of merit across this family of polymers. This conclusion is also consistent with our observation of relatively constant hole mobilities across this family (Figure A15 shows the OECT hole mobility of the polymers). Even though P3APPT and P3AAPT have higher crystallinity in the dry film compared to P3MEEMT, [60] we did not observe significant difference in OECT hole mobility. This result, while surprising for a dry FET, is reasonable for an OECT, as the polymer film is in a hydrated state and the hole mobility is dependent on the doping level.[13,64] In summary, more oxygen content on the side chain, or having an oxygen atom on the farther end of the side chain creates larger solvation domains and results in more passive swelling and higher C^*, accounting for the predominant differences in the μC^* product for different members of this family of polymers.

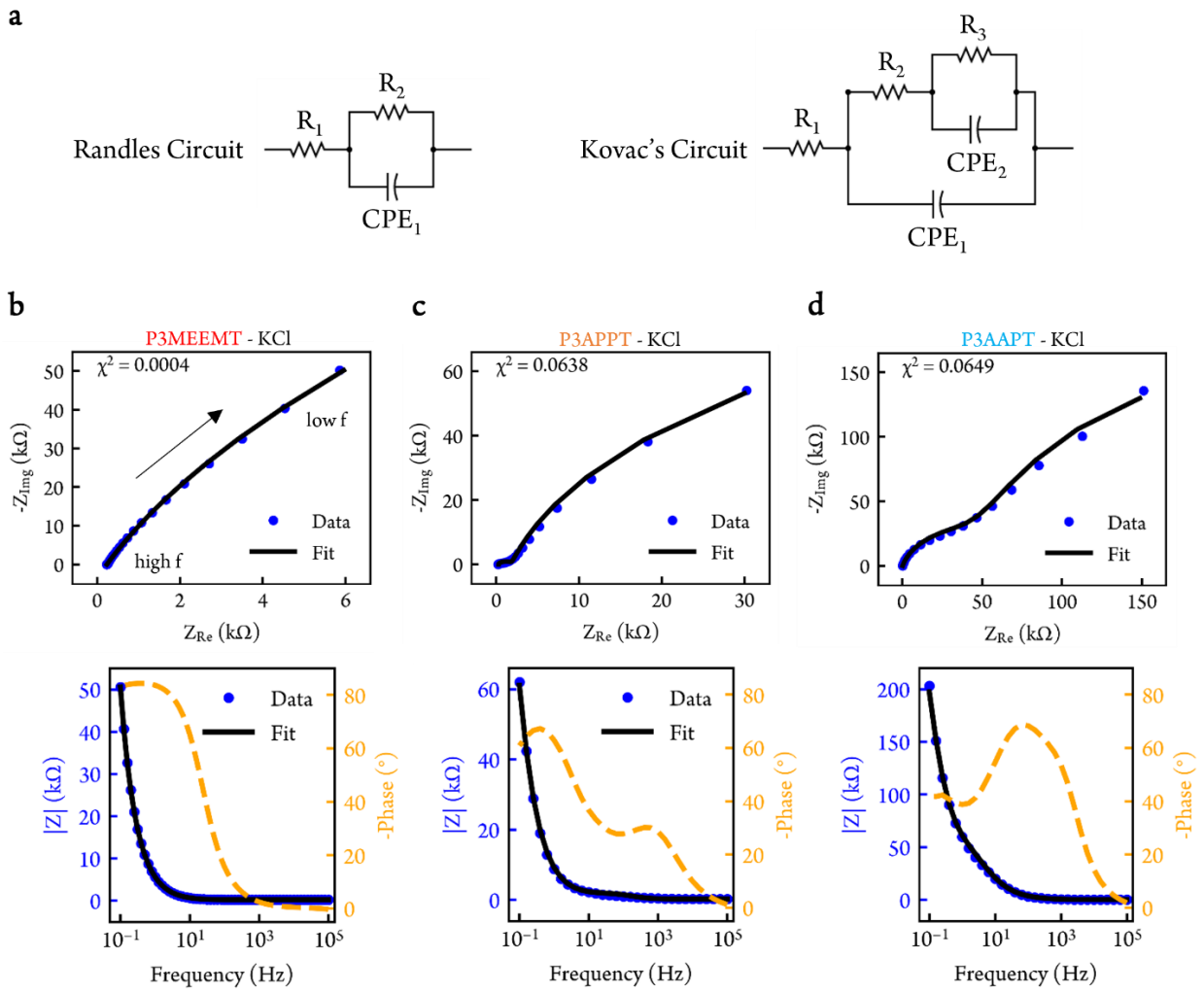

Figure 2-3. Polymer EIS results.

(a) Randles circuit (left) and Kovac's circuit (right). Resistor (R) and constant phase element (CPE). Nyquist plot (top) and Bode plot (bottom) of (b) P3MEEMT (c) P3APPT and (d) P3AAPT in 100 mmol/L $KCl_{(aq)}$.

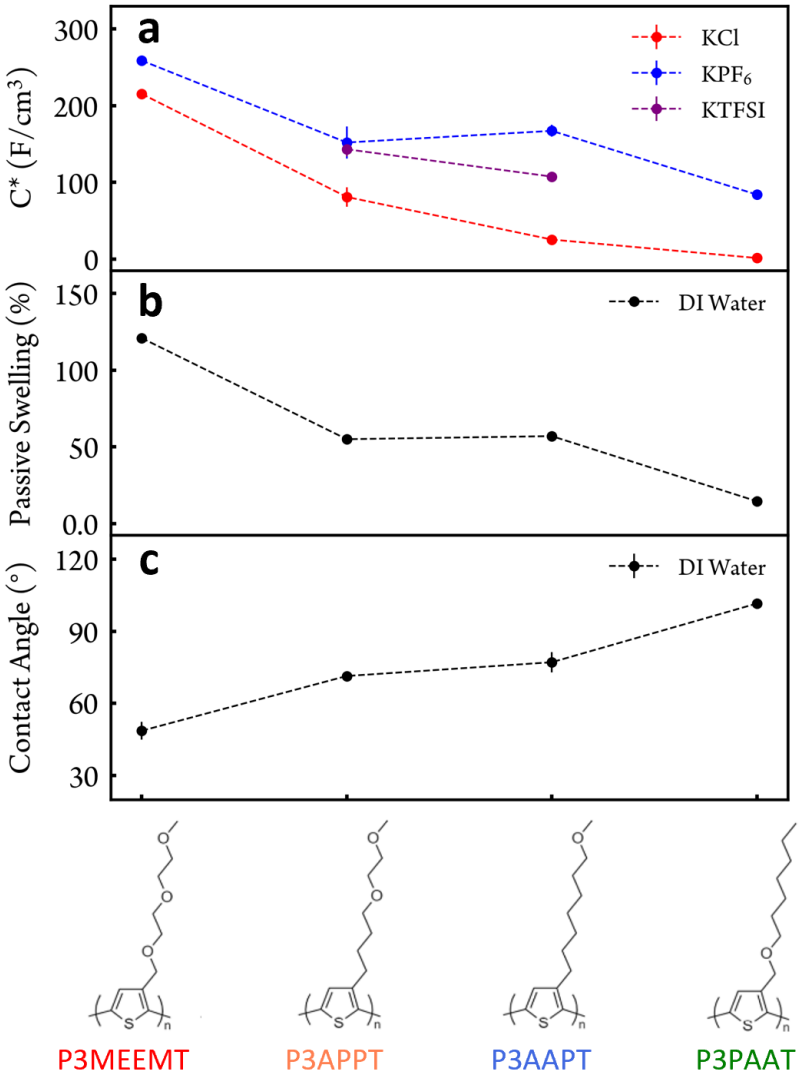

Figure 2-4. Polymer C^*, swelling and contact angle comparison.

(a) Volumetric capacitance C^* in 100 mmol/L $KCl_{(aq)}$ (red), $KPF_{6(aq)}$ (blue) and KTFSI (purple). (b) Passive swelling of polymers in DI water. We did not observe significant difference of passive swelling in $KCl_{(aq)}$, $KPF_{6(aq)}$ or DI water. (c) Water contact angle of polymers. Dash lines are guide for the eye.

2.2.3 Spectroelectrochemistry and Electrochemical Doping and Dedoping Kinetics

Figure A16 and Figure A17 show the UV-vis absorption spectra of the four polymers in KCl and KPF_6 solutions, respectively, under different doping potentials. We thoroughly dedoped the polymer films between each doping cycle. We found the π-π^* peak absorbance decreasing and the polaron peak absorbance increasing as the potential bias applied, vice versa when the dedoping bias was applied. This phenomenon indicates reversible doping and dedoping of polymers within the water potential window. We measured the π-π^* peak at ≈ 530 nm for both P3APPT and P3AAPT, ≈ 480 nm for P3MEEMT and ≈ 460 nm for P3PAAT. A broad polaron peak is at ≈ 750 nm for all 4 polymers. A vibronic progression feature is observed for both P3APPT and P3AAPT in the neutral and slightly doped states, which suggests increased planarization and ordering of polymer backbone as reported by Onorato et al.[60] In contrast, we did not observe the vibronic progression feature in P3MEEMT and P3PAAT, likely because the oxygen atom closer to the polymer backbone lowers the along-backbone ordering. Upon increasing the doping bias, the ratio between the 0-0 and 0-1 vibronic features increases for both P3APPT and P3AAPT, consistent with H-type aggregates (mainly in crystalline domain) being doped prior to other regions of the film.[64,70] This observation is similar to Thomas et al.'s results with P3HT, in which they concluded the counterion-polaron pair first formed at crystalline amorphous interface, within crystalline region and lastly in amorphous domain.[64] Our spectroelectrochemistry results thus support the notion of the formation of an inhomogeneous distribution of counterion-polaron pairs within the polymer film.

Figure A18 shows the comparison of the polaron and π-π^* peak absorbance change upon doping in KCl and KPF_6 solutions. Consistent with the impedance measurements discussed above, it is clear that higher doping levels are achieved for all polymers with chaotropic PF_6^- as the counter

anion compared to kosmotropic Cl^- as the counter anion. We also observed the π-π^* and polaron peak absorbance start to change at lower potential biases with PF_6^- as the counter anion, indicating the lower doping threshold of PF_6^- anion compared to Cl^- anion. This result verifies our earlier contention that the chaotropic counter anion lowers the doping threshold and enables higher doping level of the polymers, in agreement with our EIS and OECT results.

Interestingly, we observe an isosbestic point in the UV-Vis spectra of the three reduced-oxygen-content side chain polymers in KCl solution (Figure A16). The isosbestic point implies the clear conversion of polymer between neutral state and doped state. In contrast, in P3MEEMT, we observed slightly red shift of π-π^* peak and we did not observe the isosbestic point. We also did not observe an isosbestic point for all polymers in KPF_6 solution (Figure A17). Table A2 summarizes polythiophene derivatives with isosbestic points observed in the spectroelectrochemistry. We suspect the occurrence of an isosbestic point is related to either larger distance between counter anion and polaron or the abrupt polymer structure change upon electrochemical doping. Further investigation on this phenomenon is undergoing in our lab.

To investigate how oxygen content and position on the side chain affect the electrochemical doping and dedoping kinetics, we monitored the change of π-π^* peak absorbance over time when doping bias was applied (Figure 2-5a). Figure 2-5b shows the π-π^* peak absorbance decreases during doping potential applied in KPF_6 solution, and in KCl solution (Figure A19a). Figure A19c, S19d show the increasing of π-π^* peak absorbance when switching from doping potential to dedoping potential. To account for the doping threshold difference between the Cl^- and PF_6^- anion, the doping potential used was +0.5 V (vs Ag/AgCl) for PF_6^- anion and +0.7 V (vs Ag/AgCl) for Cl^- anion. The dedoping potential applied was -0.5 V (vs Ag/AgCl) for both anions. We used biexponential equations for fitting doping and dedoping kinetics results.

Figure 2-5c shows the distribution of doping time constants for eight polymer-ion pairs. Since no significant passive swelling difference was observed in KCl or KPF_6 solutions, we suggest that the initial hole mobility of the undoped polymer film is similar when in contact with KCl or KPF_6 solution. We thus propose that ion motion in the polymer film is the initial rate-determining step in the electrochemical doping process, especially for the reduced-oxygen-content side chain polymers. This result is consistent with both the counterion and side chain dependence of the kinetics. We found faster doping speed (or smaller doping time constants) with more oxygen atoms on the side chain, meaning more hydrophilic side chains facilitate faster ion motion in the polymer film. Comparing the polymers with only one oxygen atom, we find faster doping kinetics when the oxygen atom is farther from the polymer backbone (P3AAPT) compared to closer to the polymer backbone (P3PAAT). This result indicates polar functional groups farther from the polymer backbone are beneficial for ion movement in the polymer film, which is reasonable considering ions need to approach the polymer backbone from farther end of the side chain. In addition, we demonstrated faster doping kinetics with chaotropic PF_6^- anion compared to kosmotropic Cl^- anion for all four polymers, even though higher doping level is achieved with PF_6^- anion. This result is consistent with our previous studies and verifies that the bulky anion moves faster in the polymer film, possibly because the chaotropic anion is surrounded with less water molecules and is more polarizable compared to the kosmotropic anion. We also noticed that the doping speed is less affected by the side chain hydrophilicity when using PF_6^- as counter anion compared to Cl^-, likely because of the more hydrophobic nature of PF_6^- anion.

Figure 2-5d shows the distribution of the dedoping time constants. Though most of the studies to date focus more on doping kinetics, dedoping kinetics are also crucial, and can determine the device turn off speed in neuromorphic computing application and discharging speed in

battery/supercapacitor applications. Interestingly, we find the dedoping speed is less affected by side chain oxygen content and ion species. While one might thus be tempted to attribute the dedoping kinetics to the hole mobility in the polymer, the measured dedoping time constants (≈ 10^{-1} s) are not at the correct order of magnitude if dedoping only depends on hole drifting (≈ 10^{-7} s), assuming a 1 V bias and 100 nm thick film, with a 10^{-3} cm^2/Vs mobility. A more complex process like coupled polaron-counterion movement may be involved during dedoping. Table 2-2 and Table 2-3 summarize the electrochemical properties of polymers in 100 mmol/L $KCl_{(aq)}$ and $KPF_{6(aq)}$.

Recent studies suggested that porous polymer film[67] or polymer film with nanowire architecture[53] enables faster doping kinetics. We thus conducted AFM experiments to investigate the relation between surface topography and doping kinetics. Figure A20 shows the AFM topography images of these four polymers. We found P3APPT film is smoother than P3MEEMT film, while P3AAPT and P3PAAT films are rougher than P3MEEMT. We do not find a direct correlation between film topography and doping or dedoping kinetics for this family of polymers, as such, we concluded that the kinetics trend observed in this study is not due to the film morphology difference. Figure A21 compares the roughness of neat polymer films, doped polymer films (with KPF_6), and further with polymer films doped and dedoped for three cycles with KPF_6. We did not observe significant change of polymer film roughness in these three states.

Lastly, we measured OECT kinetics with P3APPT in both KCl and KPF_6 solutions with a high time resolution capture system. Figure 2-6 shows the OECT transient measurement of P3APPT in KCl and KPF_6 solutions. The time resolution of the data capture is 1 ms. The drain voltage was fixed at -0.6 V and a gate doping bias was applied around 9 s and removed at 59 s. The gate voltage used was -0.5 V (vs Ag/AgCl) for KPF_6 solution and -0.7 V for KCl solution.

We showed that OECT kinetics results agree with spectroelectrochemistry kinetics results: (1) doping speed is ion dependent and faster doping speed for PF_6^- anion (≈ 0.58 s) compared to Cl^- anion (≈ 9.0 s) (2) dedoping speed is less ion dependent (≈ 0.011 s for both ions) and (3) we observe a faster dedoping speed compared to doping speed. We noticed that the difference between doping and dedoping speed is further amplified in the OECT measurement compared to the spectroelectrochemistry measurement. We attribute this result to a combination of the differences in kinetics, and a difference in measurement and device geometry. In spectroelectrochemistry, the direction of polaron injection is perpendicular to the transparent, conducting FTO substrate. In contrast, polarons are injected from source electrode into channel conjugated polymer in OECT, which is parallel to the substrate. In the OECT, as soon as a small region is dedoped, the OECT turns "off", while in spectroelectrochemistry, we probe the entire concentration of polarons through the film stack.

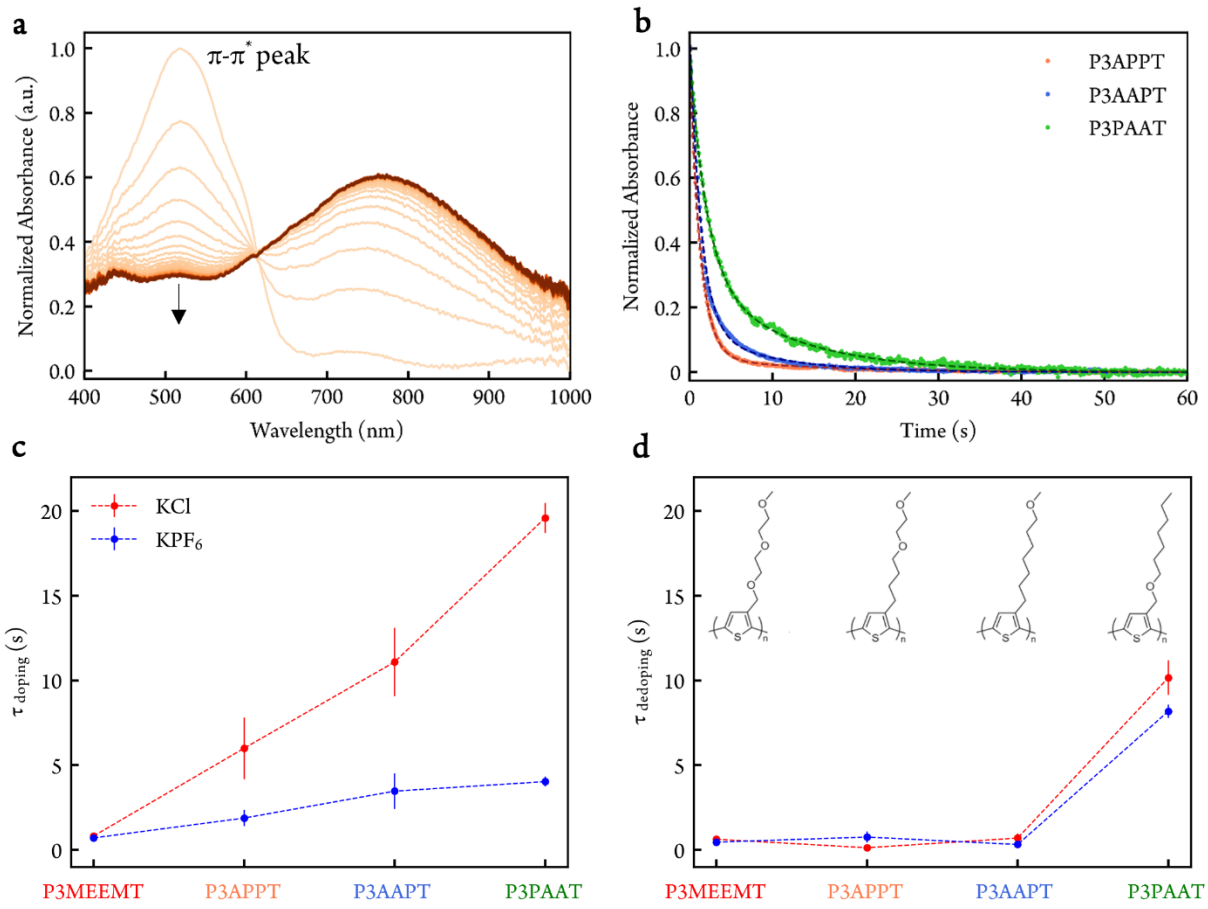

Figure 2-5. Polymer doping and dedoping kinetics via spectroelectrochemistry.

(a) UV-Vis spectra of P3APPT change over time when doping in 100 mmol/L $KPF_{6(aq)}$). Doping potential = 0.5 V vs. Ag/AgCl. We plotted the spectra change every 0.5 s from 0s to 60s. (b) Normalized π-π* change of P3APPT, P3AAPT and P3PAAT in $KPF_{6(aq)}$. Dash lines represent the fitting results. (c) Doping and (d) dedoping time constants of polymers in 100 mmol/L $KCl_{(aq)}$ (red) and $KPF_{6(aq)}$ (blue) via spectroelectrochemistry. Dash lines are guide for the eye. Note that P3PAAT has the lowest doping level but the doping speed is still the slowest.

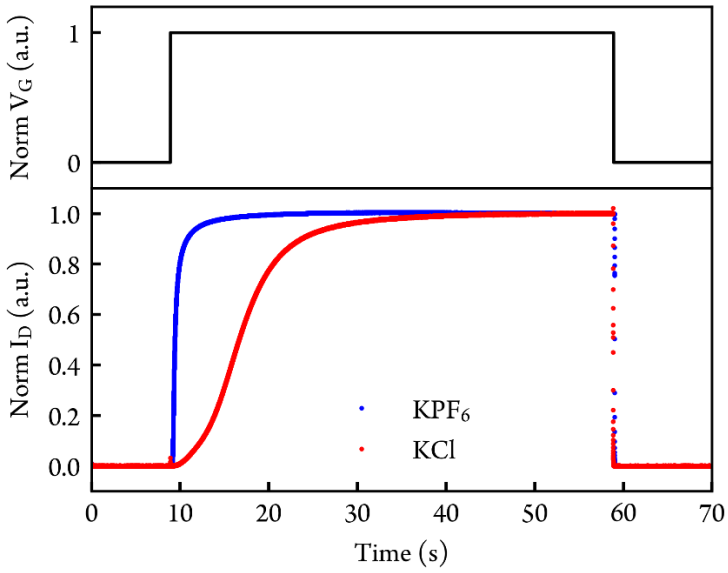

Figure 2-6. OECT transient measurements.

Comparison of OECT transient measurements of P3APPT polymer in 100 mmol/L $KCl_{(aq)}$ and $KPF_{6(aq)}$. V_D is fixed constant at -0.6 V while V_G (-0.5 V for $PF6^-$ and -0.7 V for Cl^-) is turned on at 9 s and turned off (0 V) at 59 s. One data point represents 1 ms. Channel width/length = 1000 µm/10 µm.

Table 2-2. Summary of Electrochemical Properties of Polymers in 0.1 M KCl

	μC^{*} [a]	C^{*} [b]	μ_{OECT} [c]	V_T [d]	τ_{doping} [e]	$\tau_{dedoping}$ [f]
	(F/cm·V·s)	(F/cm^3)	($cm^2/V·s$)	(V)	(s)	(s)
P3MEEMT [g]	49.1 ± 5.0	≈ 215.5	≈ 0.23	-0.56 ± 0.01	0.82 ± 0.03	≈ 0.63
P3APPT	30.5 ± 2.2	81.0 ± 12.8	0.38 ± 0.09	-0.58 ± 0.01	6.00 ± 1.82	0.13 ± 0.05
P3AAPT	9.2 ± 2.8	25.4 ± 1.7	0.36 ± 0.13	-0.56 ± 0.01	11.09 ± 2.02	0.70 ± 0.28
P3PAAT	NA	1.3 ± 0.4	NA	NA	19.59 ± 0.88	10.16 ± 1.02

Table 2-3. Summary of Electrochemical Properties of Polymers in 0.1 M KPF_6

	μC^{*} [a]	C^{*} [b]	μ_{OECT} [c]	V_T [d]	τ_{doping} [e]	$\tau_{dedoping}$ [f]
	(F/cm·V·s)	(F/cm^3)	($cm^2/V·s$)	(V)	(s)	(s)
P3MEEMT [g]	96.7 ± 10.2	≈ 259	≈ 0.37	-0.42 ± 0.01	0.71 ± 0.02	≈ 0.46
P3APPT	41.3 ± 2.8	152.0 ± 21.1	0.27 ± 0.06	-0.27 ± 0.01	1.88 ± 0.48	0.76 ± 0.33
P3AAPT	33.2 ± 3.3	167.2 ± 7.7	0.20 ± 0.03	-0.35 ± 0.01	3.47 ± 1.06	0.32 ± 0.06
P3PAAT	13.3 ± 1.4	84.0 ± 5.9	0.16 ± 0.03	-0.47 ± 0.01	4.03 ± 0.29	8.18 ± 0.40

a. μC^{*} is obtained via Eq. 1 with g_m at $|V_G| - |V_T| = 0.13$ V. $V_D = -0.6$ V. Error bars represent standard error of the mean.
b. C^{*} is measured at $|V_{doping}| - |V_T| = 0.13$ V. Error bars represent standard error of the mean.
c. Obtained via dividing μC^{*} by C^{*}. Error bars represent standard error of the mean.
d. See Figure A4. Error bars represent standard error of the mean.
e. Electrochemical doping time constant via spectroelectrochemistry. $V_{doping} = 0.7$ V (vs Ag/AgCl). Error bars represent standard error of the mean.
f. Electrochemical dedoping time constant via spectroelectrochemistry. $V_{dedoping} = -0.5$ V (vs Ag/AgCl). Error bars represent standard error of the mean.
g. Obtained from Flagg et al.[24]

2.3 CONCLUSIONS

We compared three different side chain polymers and P3MEEMT, highlighting the importance of oxygen content and its position in the side chain on many aspects of electrochemical doping and OECT operation. First, we found increasing OECT figure of merit, μC^*, and doping speed with increasing oxygen (ethylene glycol) content on the side chain, or with the oxygen atom farther from the polythiophene conjugated backbone. Second, we showed that the variations in μC^* between polymers is largely a result of variations in the C^* as a result of the oxygen content and position. Both more oxygen content on the side chain, or having the oxygen atom farther from the backbone, result in more passive swelling and higher C^*. Replacing the oxygen atom close to the polythiophene backbone with an alkyl unit increases the film π-stacking crystallinity (higher electronic mobility in the undoped film) but sacrifices the available doping sites (lower C^* in OECT). We emphasize the importance of balancing μ and C^* while designing molecular structure for OECT materials, and the necessity to develop specific molecular design strategy for different mixed ionic-electronic conducting applications. To design high μC^* material, our results indicate that single EG unit on the side chain may not be sufficient regardless of position, but farther from the backbone helps by allowing the EG units to form extended solvation domain between two adjacent polymer chains. We speculate that future designs could balance EG contents in longer side chains, focusing on small numbers of EG units in the 2-3 range, and with the EG units positioned some distance from the backbone to maintain both moderate swelling and high π-stacking crystallinity. In addition, all three reduced-oxygen-content side chain polymers exhibit higher μC^*, lower doping threshold and faster doping kinetics with chaotropic PF_6^- anion compared to kosmotropic Cl^- anion. This result is consistent with our previous studies and suggests the superiority of chaotropic anion as counterion in p-type accumulation mode OECTs. Using

chaotropic counter anion may improve the OECT performances especially in neuromorphic computing application, in which faster kinetics and lower doping threshold are critical. We note that we chose all polymers to have a 9-atom-length side chain in this study to isolate the effects of the oxygen position, and further OECT studies on polymers with different side chain lengths and varying oxygen positions could thus provide more insights. Finally, we found that, compared to the doping speed, the dedoping speed is generally faster and less dependent on ion species or side chain oxygen content. These results may prove useful for the selection of polymers and polymer-ion pairing to optimize the performance of OECTs, as well as the kinetics of OECTs, organic neuromorphic circuitry, and aqueous polymer-based electrochemical energy storage.

2.4 MATERIALS AND METHODS

Chemicals

Potassium chloride (KCl), potassium hexafluorophosphate (KPF_6), potassium trifluoromethanesulfonimide (KTFSI) and chlorobenzene were purchased from Sigma-Aldrich. All other chemicals, unless otherwise specified, were obtained from Sigma-Aldrich and used as received.

Polymer Synthesis

The detailed monomer and polymer synthesis are described in the previous studies. [24,60]

Sample Preparation

All polymers were dissolved in chlorobenzene and stirred overnight at 50 °C. The concentration of polymer solution is 20 mg/mL. The substrates were cleaned sequentially by sonication in acetone and isopropanol for 15 min each. The surface of the substrate was then treated with oxygen plasma for 3 min before spin coating at 1000 rpm (1 rpm = 2π/60 rad/s) for 60 s. All electrolytes were made with Milli-Q water. All electrolytes were degassed before measurements. We degassed the electrolytes via sparing nitrogen gas into solution (≈ 10 mL) for over 10 min.

Spectroelectrochemistry

The ultraviolet-visible, UV-Vis, absorption spectra at different doping potential and the electrochemical doping and dedoping kinetics were measured using a Metrohm Autolab PGSTAT204 (with NOVA Software version 2.1) coupled with an Agilent 8453 spectrometer. Polymer was spun casted onto fluoride-doped tin oxide-coated glass (FTO, Sigma-Aldrich, 7 Ω/sq)

and was used as a working electrode. A Ag/AgCl electrode and a Pt mesh was used as reference electrode and counter electrode, respectively. All three electrodes were submerged into a cuvette containing either 100 mmol/L $KCl_{(aq)}$ or $KPF_{6(aq)}$. UV-Vis measurements were collected with an integration time of 0.1 s/spectrum. The decay of the π-π* absorption (Abs) peak over time during electrochemical doping is fit to the biexponential function: $Abs(t) = a_1 \cdot e^{-t/\tau_1} + a_2 \cdot e^{-t/\tau_2}$. And the doping time constant is defined as $a_1 \cdot \tau_1 + a_2 \cdot \tau_2$. The recovery of the π-π* absorption peak over time during dedoping is fit to the biexponential function: $Abs(t) = b_1 \cdot (1 - e^{-t/\tau_1}) + b_2 \cdot (1 - e^{-t/\tau_2})$. And the dedoping time constant is defined as $b_1 \cdot \tau_1 + b_2 \cdot \tau_2$.

Organic Electrochemical Transistor (OECT) Device Fabrication and Characterization

OECT devices comprised lithographically patterned gold on glass substrates (see lithography process below) with transistor lengths of 10 μm and widths ranging from 100 μm to 4000 μm. Reduced-oxygen-content side chain polymers were spun casted onto OECT substrates and were carefully removed except at the electrode junction region via cotton tips under microscope. Cotton tips were slightly dampened with acetone solution. An insulating layer containing cellulose acetate and acrylates copolymer (Nail polish: Sally Hansen, Insta-Dry Top Coat) was then applied to avoid the direct contact between electrode and electrolyte during further characterizations. Devices were measured in degassed electrolytes. The electrolyte (≈ 1 mL) was contained in a polydimethylsiloxane (PDMS) reservoir during OECT measurements. The assembly of the OECT substrate, the PDMS reservoir and the electrical connections were achieved via a 3D-printed holder. Transfer curves were measured by varying V_G from 0 V to -0.7 V and then back to 0 V (vs. Ag/AgCl). The V_D was fixed at -0.6 V. For KCl electrolyte, the step size of V_G was either 0.01 V with 5 s between each step or 0.05 V with 20 s between each step. For KPF_6 electrolyte, the step

size of V_G was 0.01 V with 2.5 s between each step or 0.05 V with 10 s between each step to ensure reaching steady-state and minimizing hysteresis between forward and backward scans.

The detailed lithography process: NR9-3000PY negative resist (Futurrex, Inc.) was deposited on cleaned glass wafers with diameter equals to 0.1016 m (University Wafer, Inc.) through spin-coating, followed by UV light exposure (ABM-SemiAuto-Aligner) and resist development. Metal deposition (10 nm chromium or titanium and 100 nm gold) was accomplished through sputtering (Evatec LLS EVO Sputter System) or evaporation (CHA Solution e-beam evaporator). The resist lift-off was achieved by soaking wafers in acetone solution overnight. The wafers were then diced using a Disco Wafer Dicer (Disco, America).

Electrochemical Impedance Spectroscopy (EIS) for C^* Determination

EIS measurements were performed on gold-coated glass substrates with a defined area of (0.01 or 0.04) cm^2. Polymers were spun casted on the gold substrates. A Ag/AgCl electrode and a Pt mesh was used as reference electrode and counter electrode, respectively. The polymer was first electrochemically doped at specific direct current (DC) potential bias (ranging from 0.2 V to 0.7 V vs Ag/AgCl) for 60 s (unless otherwise specified), and the alternating current (AC) perturbation (Sine wave with 10 mV amplitude and frequency from 10^5 Hz to 10^{-1} Hz) was then performed on top of the DC potential bias. The obtained EIS data was fit to either a Randles circuit[61,62] or a Kovac's circuit.[62,63] Fitting was performed with the Metrohm NOVA software or Python impedance.py package.[71] The definition of $\mathcal{X}^2$ in this study:

$$\mathcal{X}^2 = \left(\sum_{i=1}^{n} \frac{\left[\left(Z_{Re,Data} - Z_{Re,Fit}\right)^2 + \left(Z_{Img,Data} - Z_{Img,Fit}\right)^2 \right]}{\left(Z_{Re,Data}{}^2 + Z_{Img,Data}{}^2\right)} \right) \Big/ (n - m) \qquad (2)$$

Where n is the number of data points and m is the number of adjustable parameters in the fit (number of circuit element in the equivalent circuit). $Z_{Re,Data}$ and $Z_{Re,Fit}$ represent the measured and fitted real part of impedance. $Z_{Img,Data}$ and $Z_{Img,Fit}$ represent the measured and fitted imaginary part of impedance, respectively.

Quartz Crystal Microbalance with Dissipation (QCM-D)

QCM-D measurements were conducted using a Q-sense Explorer (Biolin Scientific) on gold/titanium coated sensors. Passive swelling was calculated the following way. First, we recorded the frequency of the bare gold coated sensor in air and subsequently in deionized (DI) water. The crystal was then removed, and polymer solutions were spin coated onto the premeasured sensor. We then measured the polymer coated sensor in both air and DI water. Using the "stitch data" function of the QSoft401 software, we compared the frequency of the bare and coated sensor. The thickness of polymer layer in both air and water were computed using the Sauerbrey equation:[69]

$$\Delta m = \frac{-17.7}{n} \Delta f_n \qquad (3)$$

Where Δm is the areal mass, n is the overtone number and Δf_n is the change is frequency at the n^{th} overtone. We assumed the density of polymers are 1100 kg/m^3.

Cyclic Voltammetry (CV)

Cyclic voltammetry measurements were conducted using Metrohm Autolab PGSTAT204 potentiostat. Polymer was spun casted on the gold substrate and used as a working electrode. A

Ag/AgCl electrode and a Pt mesh was used as reference electrode and counter electrode, respectively. The scan rate used is 50 mV/s.

Atomic Force Microscopy (AFM)

AFM data, including topography and scratch edge images for film thickness measurements, were acquired on an MFP-3D. Polymers were deposited on either FTO or glass substrate.

Contact Angle Measurement

Contact angle measurements were conducted using the custom-built setup with a CCD camera a height adjusTable Atage. The images were analysed using the FTA32 software.

P3MEEMT Data

P3MEEMT data, except for QCM swelling measurements, contact angle measurements and AFM measurements, were obtained from our previous study and used directly for comparison to the reduced-oxygen-content side chain polymers.[24]

2.5 Author Contributions

S.E.C. was responsible for conceptualization, formal analysis, investigation, visualization, writing – original draft, and writing – review & editing. L.Q.F. was responsible for formal analysis and investigation. J.W.O. was responsible for conceptualization and investigation. R.L. was responsible for investigation. J.G. was responsible for formal analysis. C.K.L. was responsible for supervision and writing – review & editing. D.S.G. was responsible for supervision and writing – review & editing.

2.6 Acknowledgements

This paper is based primarily on work funded through the National Science Foundation DMR-2003456. J.W.O. and C.K.L.'s contributions to polymer synthesis are based in part on work supported by the National Science Foundation DMREF-1922259. S.E.C. thanks the support from Clean Energy Institute (CEI) at the University of Washington. L.Q.F. thanks the support of the NIST National Research Council (NRC) associateship. We thank Dr. Rajiv Giridharagopal and Prof. Connor G. Bischak for fruitful discussions. We thank Luke Khoury and Prof. John Berg for helping with contact angle measurements. Part of this work was conducted at the Washington Nanofabrication Facility / Molecular Analysis Facility, a National Nanotechnology Coordinated Infrastructure (NNCI) site at the University of Washington with partial support from the National Science Foundation via awards NNCI-1542101 and NNCI-2025489.

Chapter 3. WHY ACCUMULATION MODE ORGANIC ELECTROCHEMICAL TRANSISTORS TURN OFF MUCH FASTER THAN THEY TURN ON

This work has been submitted to Nature Materials and is also available on arXiv: arXiv:2305.01179.

3.1 INTRODUCTION

Organic electrochemical transistors (OECTs) are currently being explored for applications including bioelectronics,[1–4] logic circuit elements,[5,6] and neuromorphic devices.[7–10] As a class of transistors, OECTs feature high transconductance (≈ mS),[11] low operation voltage (typically < |1 V|),[11] and direct response to biologically relevant ions[72,73] and neurotransmitters.[74,75] The typically soft and flexible nature of organic semiconductors used in OECTs enables the detection of action potentials[2,76] and opens the window for applications in brain-machine interfaces and in vivo sensing.[77–79] To unleash the full potential of OECTs, a deeper understanding of the fundamental transistor operation mechanism is necessary, especially transistor switching behaviors, which are critical to the training phase of neuromorphic computing and simulating behaviors of arrays of transistors and their scaling properties.[12,80]

In OECTs, organic semiconductors — also referred to as organic mixed ionic-electronic conductors (OMIECs) in this context — are used as channel active layers, with the most common materials being conjugated polymers.[13,26,27,81,82] The conductivity of an OECT is modulated by the electrochemical gate potential, which controls the doping level (redox state) of the conjugated polymer channel. Importantly, in contrast to conventional field-effect transistors (FETs), OECTs

exhibit volumetric doping: the gate voltage changes the conductivity of the entire volume of the transistor channel, rather than just the surface layer, and counterions injected from the electrolyte provide charge compensation for injected electronic carriers.[20] At steady-state, the channel current (I_D) is governed by both carrier mobility and carrier density. The steady-state behavior of OECTs has been relatively well studied.[19,26,27,37] To benchmark the device performance, the product of electronic mobility and volumetric capacitance, μC^*, has been recognized as the material figure of merit of OECT in steady-state operation.[29]

Compared to the steady-state performance, our current knowledge of OECT kinetics is limited.[19] For example, the switching speed for materials with identical μC^* can vary by many orders of magnitude.[39] Understanding the switching behaviors of OECTs is crucial for designing logic units as well as emulating and sensing neural activity, which typically operates at the frequency of ≈ 100 Hz.[76] The widely-used Bernards model describes the transient behavior with an equivalent RC circuit as the ionic path and makes the quasistatic approximation for the channel charge distribution.[37] Several improved models based on the original Bernards model have been proposed with more complex equivalent circuits describing the ionic circuit.[83,84] Recently, Paudel *et al.*[85] demonstrated a 2D-finite element model based on drift-diffusion process and shows the existence of the lateral ion current during switching, which is neglected in the traditional model. However, it should be noted that all these kinetics studies are based on poly(3,4-ethylenedioxythiophene):poly(styrene sulfonate) (PEDOT:PSS), which operates as a depletion mode OECT, with the transistor in the on-state when no gate potential is applied. The transient response of PEDOT:PSS-based OECTs may not be directly comparable to accumulation mode OECTs. Accumulation-mode OECTs are generally more favorable for practical applications because of their comparatively lower energy-consumption, particularly for in vivo bioelectronics

and neuromorphic computing. Nevertheless, to our best of knowledge, no studies have yet to systematically discuss the transient response and device turn-on/turn-off kinetics of accumulation mode OECTs.

In this article, we study the asymmetric transient behavior of accumulation mode OECTs. Through operando optical microscopy coupled with OECT characterization, we find that OECT turn-on occurs in two distinguishable stages: (1) doping front propagation and (2) vertical doping. In contrast, device turn-off occurs in one continuous stage. We further identify the factors that contribute to the rapid OECT turn-off behavior including typical faster dedoping kinetics of conjugated polymers compared to their doping kinetics, the channel geometry, and the carrier density-dependent mobility. Combining these observations, we propose an empirical model describing the switching behavior of accumulation mode OECTs and provide physical interpretations to the response time constants. Lastly, we show that ion transport is the limiting factor to device kinetics, and we offer guidance for engineering faster accumulation mode OECTs from both materials and device perspective.

3.2 Results and Discussions

3.2.1 Asymmetric OECT Response Times

Figure 3-1a shows a typical transient response of an accumulation mode OECT: the transistor is turned on (higher $|I_D|$) upon gate potential applied and is turned off upon potential removal. We first tried the Bernards model[37] to describe the transistor switching behavior (Note B1). The Bernards model expresses the variation of I_D over time as a single exponential function upon a square V_G pulse, with one RC time constant related to ion transport into the channel polymer.[37] We found that Bernards model fails to predict the transient response of accumulation mode OECTs from three aspects: (1) the initial transistor turn-on, which manifests as a short delay (Fig. 3-1a, bottom left) rather than instant turn-on, cannot be well-captured; (2) the transistor turn-on cannot be described with a single exponential function; (3) the difference in transistor switching-on and switching-off times cannot be described (Fig. 3-1a). These issues, especially the difference in transistor switching times, cannot be resolved even if the improved models are applied, which focus more on interpreting the pre-exponential factor.[83,84]

Figure 3-1b and Table 3-1 display the turn-on and turn-off times of accumulation mode OECTs from both this paper and our literature survey. We considered published results with typical planar structure and aqueous electrolyte, which is the most common OECT structure to date. Figure 3-1b shows that faster device turn-off compared to turn-on is indeed ubiquitous, though rarely discussed aside from limited reports on PEDOT:PSS.[86]

One hypothesis is that this asymmetry could arise from the switching potentials chosen. Based on the Butler–Volmer model, the electrochemical reaction rate is influenced by the activation potential.[87–89] Since the threshold voltage (V_T) varies with different polymer-electrolyte systems, it is possible that the faster turn-off is the result of smaller voltage difference between V_{on} and V_T

compared to V_{off} and V_T, namely, $|V_{on} - V_T| < |V_{off} - V_T|$. To rule out the influence of the mismatch between switching on and off gate potentials, we selected three p-type polymers as examples and carefully tested their OECT kinetics with fixed voltage difference between V_T and switching potentials. The three conjugated polymers studied here are: poly[2,5-bis-(thiophenyl)-1,4-bis(2-(2-(2-methoxyethoxy)ethoxy)ethoxy)-benzene] (PB2T-TEG), poly(3-{[2-(2-methoxyethoxy)ethoxy]methyl}-thiophene-2,5-diyl) (P3MEEMT), and poly(3-hexylthiophene-2,5-diyl) (P3HT); and the two aqueous electrolytes are: potassium chloride (KCl) and potassium trifluoromethanesulfonimide (KTFSI). The chemical structure of the polymers and the device performance are shown in Fig. B1. After considering threshold voltage, we still observed faster turn-off behavior (Fig. 3-1b, stars). Clearly, the faster turn-off is not caused by the mismatch between switching potentials, and the asymmetry in OECT switching times may be related to other factors such as polymer doping and dedoping kinetics or device geometry.

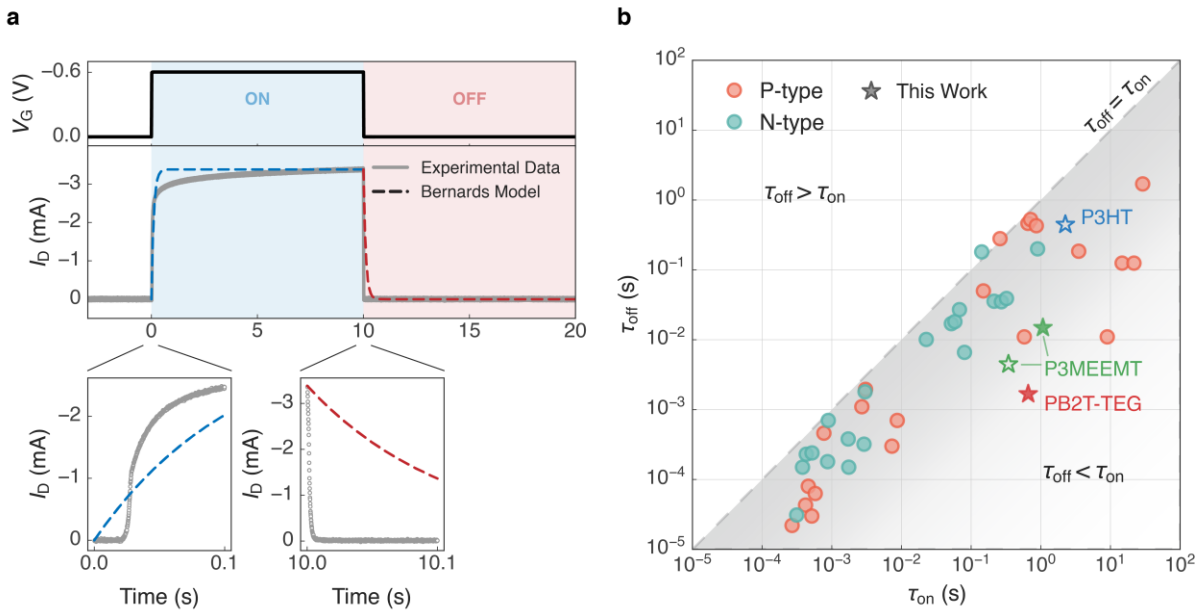

Figure 3-1. OECT response times.

a, Transient response of a typical accumulation mode OECT (solid) and the fit with Bernards model (dashed). The initial stage of transistor turn-on and turn-off are magnified for clarification. b, Accumulation mode OECT response times in literatures. Each point represents one polymer-electrolyte pair. Detailed response times and references are listed in Table 3-1. The device response times measured in this work with carefully chosen gate voltage considering threshold voltage are represented as star symbols, which are PB2T-TEG (0.1 M KCl), P3MEEMT (0.1 M KCl), P3MEEMT (0.1 M KTFSI) and P3HT (0.1 M KTFSI). Solid and unfilled stars represent devices operated in 0.1 M KCl electrolyte and 0.1M KTFSI electrolyte, respectively.

Table 3-1. Accumulation Mode OECT Response Times in Literatures

Polymer	Type	Ion Concentration (mM)	Ion Type	τ_{on} (ms)	τ_{off} (ms)	Reference	Note
gDPP-g2T	p	PBS buffer	PBS buffer	0.269	0.022	[5]	cOECT
p(g2T-TT)	p	100	NaCl	0.42	0.043	[90]	
P(gTDPPT)	p	100	NaCl	0.46	0.08	[34]	
P(bgDPP-MeOT2)	p	100	NaCl	0.516	0.03	[91]	
P(lgDPP-MeOT2)	p	100	NaCl	0.578	0.063	[91]	
p(gPyDPP-MeOT2)	p	100	NaCl	0.77	0.46	[92]	
PBBTL	p	100	NaCl	2.7	1.1	[93]	
PBBTL/BBL blend	p	100	NaCl	3.05	1.95	[93]	
TDPP-gTVT	p	100	NaCl	7.3	0.3	[57]	
TDPP-gTBTT	p	100	NaCl	8.7	0.7	[57]	
PProDOT-DPP	p	100	LiCl	150	50	[94]	
PProDOT-DPP	p	100	$LiPF_6$	260	280	[94]	
P3APPT	p	100	KPF_6	580	11	[25]	estimation
PIBET-AO	p	50	KCl + $CaCl_2$	654	463	[95]	
PIBET-O	p	50	KCl + $CaCl_2$	714	526	[95]	
PIBET-BO	p	50	KCl + $CaCl_2$	862	429	[95]	
PIBT-BO	p	50	KCl + $CaCl_2$	3500	185	[95]	
P3APPT	p	100	KCl	9000	11	[25]	estimation
DPP-DTT (8:2)	p	100	KPF_6	14705	125	[53]	400 μm, estimation
DPP-DTT (1:0)	p	100	KPF_6	21739	125	[53]	400 μm, estimation
PIBET-A	p	50	KCl + $CaCl_2$	29000	1700	[95]	
Polymer	Type	Ion Concentration (mM)	Ion Type	τ_{on} (ms)	τ_{off} (ms)	Reference	Note
Homo-gDPP	n	PBS buffer	PBS buffer	0.313	0.031	[5]	cOECT
BBL_{152}	n	100	NaCl	0.38	0.15	[48]	
BBL_{98}	n	100	NaCl	0.43	0.23	[48]	
BBL_{60}	n	100	NaCl	0.52	0.24	[48]	
gNDI-T	n	100	KCl	0.87	0.18	[96]	normalized to area
BBL_{15}	n	100	NaCl	0.89	0.7	[48]	
PBBTL/BBL blend	n	100	NaCl	1.72	0.38	[93]	
P(gTDPP2FT)	n	100	NaCl	1.75	0.15	[34]	
gNDI-V	n	100	KCl	2.9	0.32	[96]	normalized to area
P(gPzDPP-CT2)	n	100	NaCl	3	1.8	[97]	
P(gPzDPP-2T)	n	100	NaCl	22.7	10.1	[97]	
f-BTI2g-TVTCN	n	100	NaCl	52	17	[98]	
gAIID-2FT	n	100	NaCl	58.5	18.2	[99]	
f-BTI2g-TVT	n	100	NaCl	68	27	[98]	
BBL_H	n	100	KCl	80.3	6.6	[100]	
BBL_L	n	100	KCl	142	181	[100]	
gAIID-T	n	100	NaCl	213.3	35.6	[99]	
f-BTI2TEG-FT	n	100	NaCl	272	35	[101]	
f-BTI2TEG-T	n	100	NaCl	322	39	[101]	
BBL	n	100	NaCl	900	200	[102]	estimation

3.2.2 Comparison between OECT and Spectroelectrochemistry

Because the magnitude of I_D is closely related to the electrochemical doping level of the channel conjugated polymer, it is possible that faster OECT turn-off is the consequence of rapid electrochemical dedoping nature of the polymer. To verify this hypothesis, we compared the doping and dedoping kinetics of spectroelectrochemistry (two-terminal diodes) to the turn-on and turn-off speed of OECTs (three-terminal transistors). Figure 3-2a,b display the geometries of the spectroelectrochemistry and OECT measurements. Figure 3-2c shows the steady-state UV-Vis spectra, which provides information on the electronic states of the conjugated polymers. When electrochemically doped, the polymer is oxidized along with the formation of a polaron, resulting in the bleaching of the π-π^* transition peak ($\approx$ 525 nm) and the increase of the polaron peak ($\approx$ 680 nm). Figure 3-2d shows the transistor output curves associated with the on-state (doped) and the off-state (neutral). In addition to the steady-state study, the time-resolved UV-Vis spectra provide the rate of polaron formation and removal, which we expressed as the time constants: τ_{doping} and $\tau_{dedoping}$. We obtained the time constants from exponential fittings of polaron absorption peak over time (Fig. 3-2e and Figs. B2 and B3). Below, we referred to similar time constants from the transient response of OECT switching as τ_{on} and τ_{off} in order to distinguish them from the spectroelectrochemistry time constants (Fig. 3-2f and Figs. B2 and B3). Given the effect of the activation potential discussed in the previous section, we carefully measured the operando UV-Vis spectra under the same potential difference with respect to the equilibrium potential, or open circuit potential (OCP). The V_T and OCP values are listed in Table B1.

Figure 3-2g,h summarize the ratios of $\tau_{doping}/\tau_{dedoping}$ (spectroelectrochemistry) and τ_{on}/τ_{off} (OECT) of four polymer-electrolyte pairs, respectively. We showed that, in both spectroelectrochemistry and OECT, the processes involving polymer doping are slower than the

ones associated with polymer dedoping. However, across all polymers and electrolytes, the switching difference between these two processes is much larger in OECTs compared to spectroelectrochemistry. Table B2 reports the collected response times. Interestingly, we found that the timescale of OECT turn-on is comparable to the timescale for spectroelectrochemical doping, while OECT turn-off is much faster than spectroelectrochemical dedoping (approximately 10-100x faster). These results suggest that faster OECT turn-off is not simply due to faster polymer dedoping. We next turn to explore the possible causes.

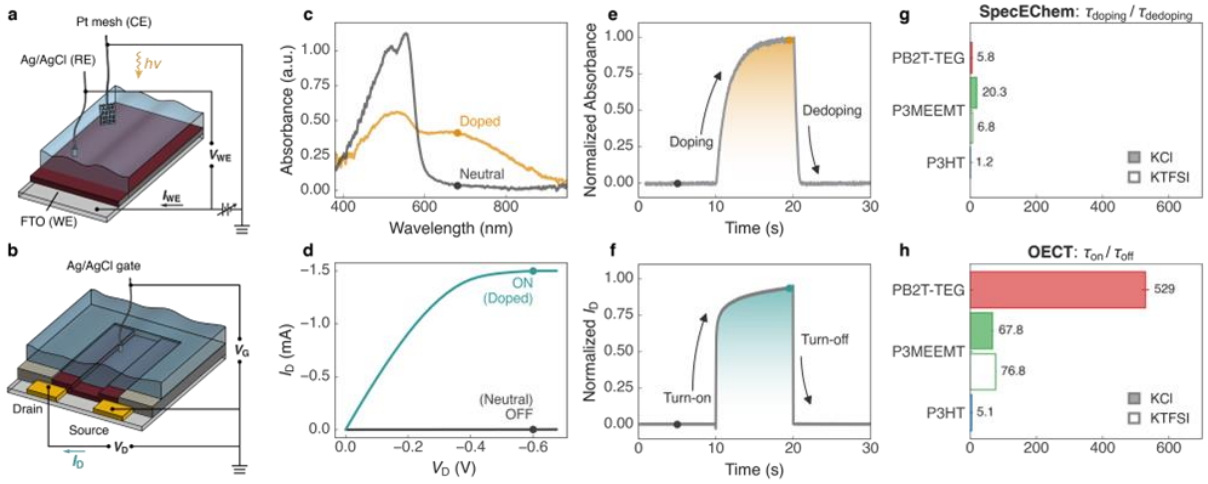

Figure 3-2. Comparison between OECT and UV-Vis spectroelectrochemistry.

a,b, Schematic diagram of spectroelectrochemistry (SpecEChem) (a) and OECT (b) experimental setups. c,d, Typical UV-Vis spectra (c) and OECT output curves (d) of two steady-states (neutral/doped). e,f, An example transient response of spectroelectrochemistry (e) at polaron peak absorption wavelength (680 nm) and OECT (f) at saturation region (V_D = −0.6 V). g,h, The $\tau_{doping}/\tau_{dedoping}$ measured in spectroelectrochemistry (g) and the τ_{on}/τ_{off} measured in OECT (h) for: PB2T-TEG and P3MEEMT with 0.1 M KCl (solid); P3MEEMT and P3HT with 0.1 M KTFSI (unfilled) The doping-voltage for spectroelectrochemistry, V_{doping} = OCP + 0.2 V, and the dedoping-voltage, $V_{dedoping}$ = OCP − 0.2 V. The on-voltage for OECT, $V_{on} = V_T$ − 0.2 V, and the off-voltage, $V_{off} = V_T$ + 0.2 V. Time resolution of spectroelectrochemistry is ≈ 10 ms and OECT is ≈ 10 s. Error bars represent standard error of the mean from multiple cycles.

3.2.3 Operando Microscopy Characterization

To further understand the origin of faster device turn-off in accumulation mode OECTs, we probed the electrochemical doping level of channel conjugated polymer via operando optical microscopy coupled with a 650 nm long pass filter to selectively monitor polaron formation (Fig. 3-3a). Figure 3-3b shows the transient response of I_D and I_G during transistor turn-on. We observed an immediate I_G response to the V_{on}, which shows a typical spiking and decay behavior, suggesting ion injection from the electrolyte into the channel polymer. In contrast, I_D remains relatively low initially after V_{on} applied, which to our knowledge, has not been discussed previously. Figure 3-3c shows the microscope movie screenshots during turn-on. Darker pixels represent more polaron absorption and thus a higher electrochemical doping level. We found that OECT device turn-on occurs in two stages: (1) a *doping front propagation* stage and (2) a *vertical doping* stage. We provide detailed discussions of each stage in the following paragraphs.

During the *doping front propagation* stage, we found that even though substantial doping of the channel polymer is already occurring, the growth of the I_D starts only after the doping front position (x_{front}) reaches the drain electrode (Fig. 3-3d,e). We thus introduce the doping front propagation time, t_p, as the time required for the doping front to propagate across the entire channel from the source to the drain electrode, with the value of ≈ 270 ms for this particular device (L = 600 μm). We defined x_{front} as the position of the peak of the first derivative of the absorbance. Figure 3-3e shows the relatively linear relation between x_{front} and time, suggesting the front is moving at a constant speed, which is ≈ 2.2 μm/ms in this case. The fact that we observed the doping front propagating from the source to drain electrode suggests that the injection of electronic carriers is occurring primarily from the source electrode during device turn-on. This result makes sense considering p-type OECTs are typically operated at negative V_G and V_D, and electron removal (or

hole injection) from channel conjugated polymer (polymer oxidation) will naturally favor the grounded source electrode instead of negatively biased drain electrode. In addition, we note that this doping front propagation stage (I_D remains relatively low after V_{on} applied) may be overlooked if transient response is characterized without enough sampling rate.

In the *vertical doping* stage, we observed a similar speed of doping of the polymer in the center of the channel and near both electrodes (Fig. 3-3f,g). We found the speed of I_D increase ($\tau_{OECT} \approx 290$ ms) and polymer doping ($\tau_{SpecE} \approx 200$ ms) is at the same order of magnitude, suggesting the I_D increment is largely dominated by the increase of doping level (or carrier density) along the channel with the underlying polymer acting as an increasingly conductive, planar electrode. Figure 3-3 shows data from PB2T-TEG, a polymer that undergoes a distinct structural phase transition upon doping.[103] While the ion-induced phase transition in PB2T-TEG provides an easily resolvable doping front for kinetic analysis, we found the two-stage behavior of a doping front propagation followed by a vertical doping, is a general across accumulation mode OECT behavior regardless of cycle numbers, active layer material, or channel length (Fig B4).

For the OECT device turn-off, or the *vertical dedoping* stage, we observed an immediate response of both I_D and I_G to the V_{off} (Fig. 3-3h). We did not observe any front propagation event compared to turn-on. Figure 3-3i,j display the polymer dedoping process along the channel. While we did not see a clear dedoping front, quantitative analysis of the microscope images shows that polymer does dedope faster near the source electrode than other positions in the channel (Fig. 3-3k). This finding partly explains the faster OECT turn-off. The conductive channel is broken by the dedoping of a thin slice near the electrode: if we consider the transistor channel as a series of resistors, as long as the resistance of one of the resistors increases (the polymer near source electrode), the total resistance will increase and thus result in the decrease in I_D. Nevertheless, this

explanation must be incomplete, as the turn-off speed of I_D is *still* much faster than the dedoping speed of polymer near source electrode. As a corollary of this behavior, we found that even though the transistor is in the off-state already, dedoping of the channel polymer is not fully completed as noted by the absorbance in the polaron band (Fig. 3-3k). This phenomenon suggests that, through shortening the off-interval (or increased duty), faster OECT turn-on in the subsequent cycle can be readily achievable, as the channel polymer is already in slightly doped state (Note B2). We speculate that this behavior may be useful in particular for designing OECT-based spiking neural networks[7,8] and emulating neuron dynamic filtering function.[43,104] We next considered whether carrier-density dependent mobility can account for the remaining acceleration of the turn-off time.

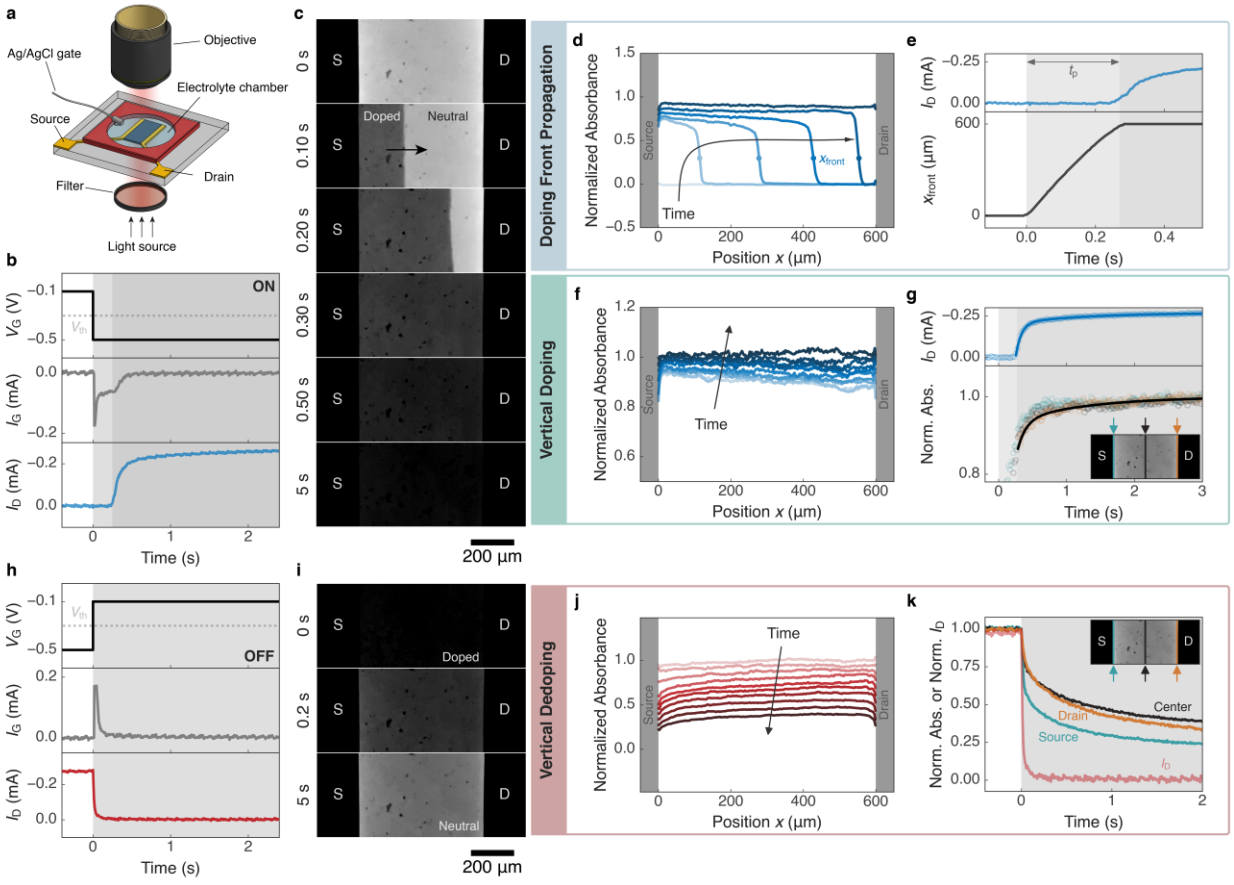

Figure 3-3. Operando optical microscope coupled with OECT switching.

a, Operando optical microscope setup schematics. b, Potential and current response during turn-on. c, Microscope movie screenshots during turn-on with timestamp labels. Darker pixel represents higher polaron concentration. d, Normalized polaron absorption along channel over time during *doping front propagation* stage (stage 1 in turn-on). e, Comparison of I_D and moving front position over time during *doping front propagation* stage. f, Normalized polaron absorption along channel over time during *vertical doping* stage (stage 2 in turn-on). g, Comparison of I_D and normalized polaron absorption over time at selected positions during *vertical doping* stage. The solid lines indicate the fits. The insert image shows the selected positions over the channel. h, Potential and current response during turn-off. i, Microscope movie screenshots during turn-off with timestamp labels. j, Normalized polaron absorption along channel over time during turn-off, or *vertical dedoping*. k, Comparison of normalized I_D and normalized polaron absorption at three selected positions over time. The insert image shows the selected positions over the channel (labeled as source, center and drain). A 650 nm long pass filter was used, and the red channel intensity is used to calculate the polaron absorbance. The polymer used here is PB2T-TEG, and the electrolyte is 0.1 M KCl. The transistor channel length is 600 μm, and the film thickness is ≈ 120 nm. The drain potential is fixed at -0.6 V.

3.2.4 Carrier Density-dependent Mobility

Figure 3-4a shows the transient response of the I_D, carrier density and average carrier mobility during the transistor turn-off. We calculated the carrier density using both the integral of gate current over time and average polaron absorbance along the channel during the vertical dedoping stage and both results are in good agreement (Fig. B5). We then estimated the average hole mobility in the channel during turn-off via:

$$\mu = \left(\frac{L}{W \cdot d \cdot e \cdot V_D}\right) \cdot \frac{I_D}{p} \quad (1)$$

assuming a linear electric field along the channel, where μ is the average carrier mobility, p is the hole density, e is the electron charge and V_D is the drain voltage. L, W, and d represent channel length, width, and thickness, respectively. We found the turn-off rate of I_D is comparable to the rate of the carrier mobility decay, which, due to the non-linear relationship between density and mobility in conjugated polymers, is about one order of magnitude faster than the carrier removal rate. This result agrees with what we have observed previously that the OECT turn-off speed is about an order of magnitude faster than polymer dedoping speed measured by spectroelectrochemistry (Table B2).

Figure 3-4b shows the calculated carrier mobility and extracted carrier density relation required to explain our data. We found that carrier mobility is indeed carrier density-dependent, especially in the high carrier density region. Previously, Friedlein et al. had demonstrated that the steady-state OECT performance could be well characterized if carrier density-dependent mobility is considered, with the relation between mobility and density being:

$$\mu = \mu_0 \cdot \left(\frac{p}{p_0}\right)^{\frac{E_0}{k_B T}-1} \quad (2)$$

where μ_0 is mobility prefactor and p_0 is zero-filed hole concentration. E_0 describes the energetic width of the tail of the density of states, k_B is Boltzmann's constant and T is temperature.[105] This equation captures the filling of the density of states (DOS) due to energetic disorder in conjugated polymer materials.[106] We found this relation also fits our carrier mobility and density data well. Note B3 describes detailed fittings and discussions of Eqn 2. We concluded that the carrier density-dependent mobility explains why the OECT turn-off is even faster than the dedoping of polymer near source electrode: not only carrier density, but also the carrier mobility decreases significantly at the initial stage of device turn-off, and both carrier mobility and carrier density contribute to I_D.

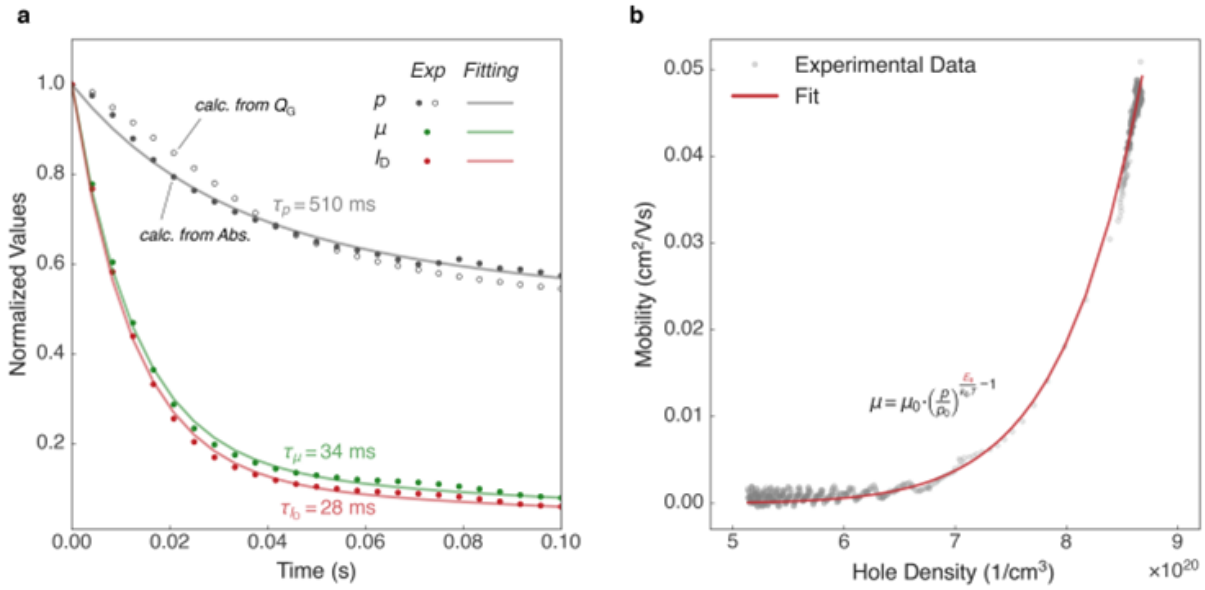

Figure 3-4. OECT mobility and carrier density.

a, Transient response of I_D, carrier density and average carrier mobility during the PB2T-TEG transistor turn-off. Solid line indicates the fit with biexponential equation. b, Calculated carrier mobility as a function of carrier density using eqn (1). Solid line indicates the fit with the eqn (2). The good fit of the classic density-dependent mobility formula to the experimental data based on the measured current and carrier density suggests the importance of carrier density-dependent mobility in explaining the rapid turn-off of OECTs.

3.2.5 Engineering Faster OECTs

With the transient behavior knowledge from operando microscopy, we expressed the two-stage turn-on with an empirical biexponential equation including the initial front propagation time (t_p):

$$\left|I_{\mathrm{D,\,Norm}}(t)\right| = A_1 \cdot \left(1 - e^{-\frac{t-t_p}{\tau_{1,on}}}\right) + A_2 \cdot \left(1 - e^{-\frac{t-t_p}{\tau_{2,on}}}\right);\ A_1 + A_2 = 1 \qquad (3)$$

where $\tau_{1,\,on}$ and $\tau_{2,\,on}$ are time constants associated with the vertical doping stage. A_1 and A_2 are two constants with the value of A_1 typically ≈ 0.7 (Fig. 3-5a). For one-stage transistor turn-off, we described I_D as:

$$\left|I_{\mathrm{D,\,Norm}}(t)\right| = e^{-\frac{t}{\tau_{\mathrm{off}}}} \qquad (4)$$

where τ_{off} is the time constant expressing vertical dedoping (Fig. 3-5a).

To understand how the factors in Eqn. 3 depend on experimental conditions, we next studied how operation variables including potential and device geometry affect OECT switching behavior (Fig. 3-5b–e and Figs. B6–B12). During the *doping front propagation* stage, we found smaller t_p with shorter channel length as expected because the doping front is propagating at a relative constant speed. Surprisingly, we found t_p is relatively independent of the drain potential. This result suggests that ion transport from electrolyte into the polymer channel, instead of electronic transport from the source electrode, is limiting the front propagation speed. Indeed, we found faster front propagation (smaller t_p values) with higher gate potentials, as the increased gate potential speeds up ion movement. We further demonstrated smaller t_p with increased ion concentration, thinner channel active layer and bulky anion,[24,25] all associated with shorter ion transport time from electrolyte into polymer channel.

In the *vertical doping* and *vertical dedoping* stages, we found a similar trend of $\tau_{1,\,on}$ and τ_{off} compared to t_p, namely, smaller $\tau_{1,\,on}$ and τ_{off} if the ion transport time from electrolyte into

polymer layer is reduced (higher gate potential, increased ion concentration, thinner polymer layer and bulky anion[24,25]). We hypothesize that smaller $\tau_{1,\,on}$ and τ_{off} with shorter channel length is akin to charging and discharging a capacitor, where smaller capacitance (shorter channel length) results in faster charging and discharging. In contrast, the slower $\tau_{2,\,on}$, with the magnitude of ≈ 2-3 s, is less dependent on all operation variables. We propose that $\tau_{2,\,on}$ is associated with polymer structural relaxation or ionic/electronic charge reorganization, as recently suggested by Wu et al.[107] In addition, we noticed that when $|V_G - V_T| > |V_D|$, or when the device is operated in the linear region (shadowed area in Fig. 3-5d and Fig. B13), the difference between turn-on and turn-off response time becomes smaller. This result is reasonable as the transistor behaves like a diode-like spectroelectrochemistry device when drain potential is decreased.

Finally, we demonstrated a SPICE circuit model that accurately reflects transient asymmetry of accumulation mode OECTs by incorporating a time-dependent channel resistor into the existing model.[84,108] The detailed SPICE simulation methods and results are in Note B4. To sum up, from the device perspective, shorter channel length, thinner polymer layer and higher gate potential (not drain potential) facilitate more rapid device switching. From the materials perspective, one could increase ion concentration, select a bulky counter anion, or design polymer with high ionic conducting ability or with rigid backbone.[100,109]

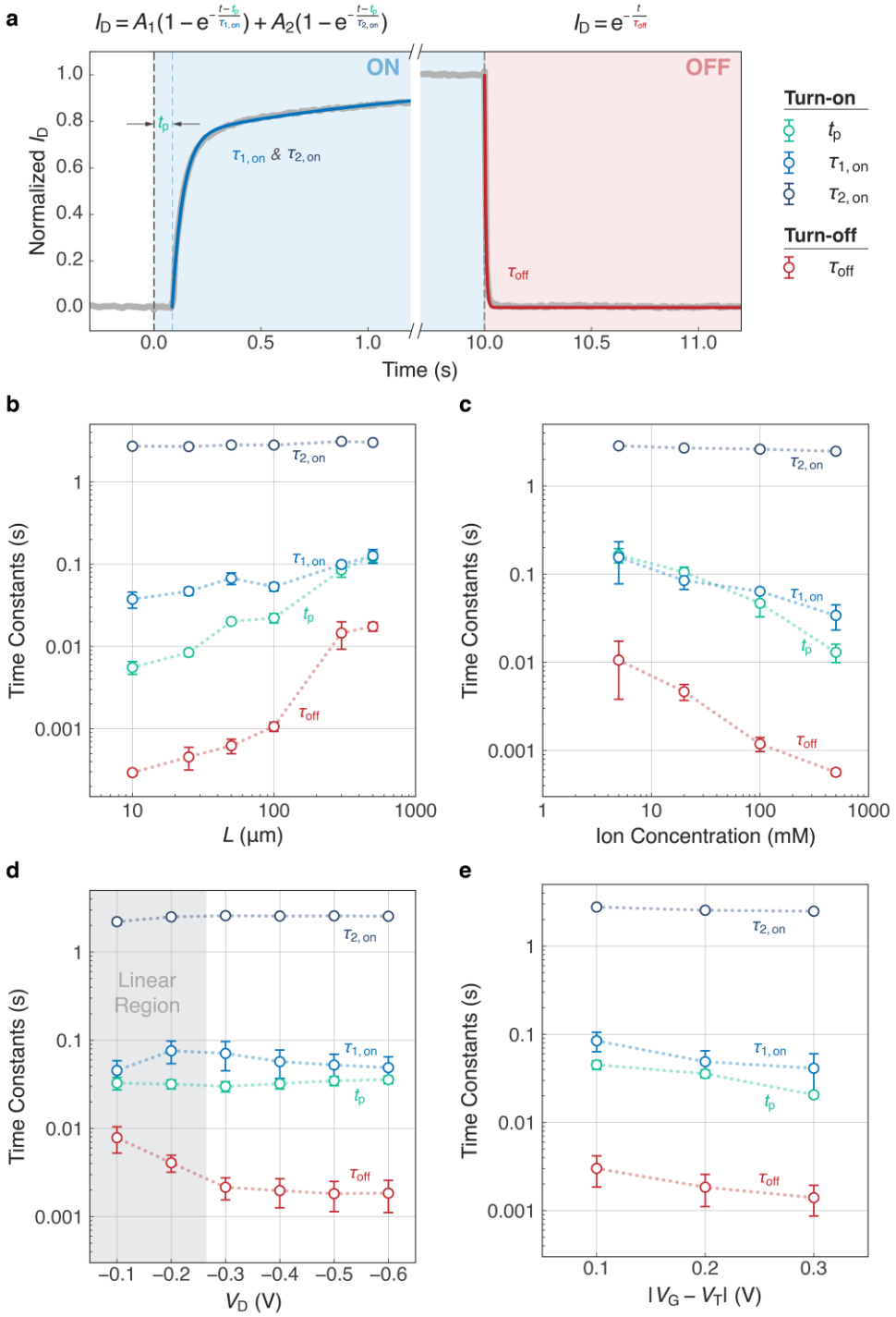

Figure 3-5. Dependency of OECT response times on the operation variables.

a, Transient response of a typical accumulation mode PB2T-TEG OECT and the fitting equations. b, Relation between time constants and channel length. c, Relation between time constants and ion

concentration. d, Relation between time constants and V_D. e, Relation between time constants and $|V_G - V_T|$. Transistor channel width is 2.5 or 5 mm, and the thickness is ≈50 nm for all cases. Electrolyte is 0.1 M KCl and transistor channel length is 100 μm unless otherwise specified. V_D is −0.6 V and $|V_G - V_T|$ is 0.2 V unless otherwise specified. Error bars are standard error of the mean from at least 3 different devices. Dashed lines are guide to the eye.

3.3 CONCLUSIONS

We show that three different conjugated polymers exhibit much faster turn-off compared to turn-on when used to make accumulation mode OECTs. This behavior, while ubiquitous in the literature, is rarely discussed, and is inconsistent with many common OECT models. Using operando optical microscopy, we demonstrate that device turn-on occurs in two temporally and spatially distinct stages: first, a doping front propagates from the source to the drain; second, the partially doped channel continues to dope more homogeneously. In contrast, turn-off occurs in a single step, with the kinetics varying weakly across the channel and the fastest dedoping occurring near the source. We identify several factors contributing to faster device turn-off including channel geometry, differences in doping and dedoping kinetics, and the physical phenomena of carrier density-dependent mobility. In this limit, reducing channel length can be very important to reducing turn-on time due to the initial doping front propagation step. Second, doping processes are generally slower than dedoping, a factor we hypothesize is due to the rearrangement of the polymer that accompanies the doping process. Nevertheless, the doping front propagation and asymmetry of doping and dedoping rates are still insufficient to explain the large differences in turn-on vs. turn-off times for OECTs. The final key piece which we propose to explain the rapid turn-off is density-dependent mobility. Notably, the functional form of the mobility that we extract using this hypothesis is in excellent agreement with previous reports of the function dependence of carrier mobility on charge density in organic semiconductors. Finally, we show that ion transport is limiting the device speed in that it controls both doping and dedoping kinetics. These observations provide guidelines for engineering faster accumulation mode OECTs from both materials and device perspectives. We believe this unique transient asymmetry renders accumulation mode OECT as a tailorable “slow-learning, fast-forgetting” unit which may found

position in either the toolbox of traditional circuit design or neuromorphic computing applications. We anticipate these results will aid in the selection of counterion chemistries and transistor geometries for specific applications and set that stage for full drift-diffusion models that simulate device behavior of both accumulation and depletion mode OECTs and improve the accuracy of simplified equivalent circuit models.

3.4 MATERIALS AND METHODS

Polymer film preparation and characterization

The synthesis of PB2T-TEG[103,110] (see detailed molecular weight information in the previous paper[50]) and P3MEEMT[24] (M_n = 24 kg/mol, $Đ$ = 1.67) polymers were described in our previous works. P3HT was obtained from Ossila (M109, M_w =36.6 kg/mol). PB2T-TEG polymer was dissolved in chloroform with the concentration of 2 to 4.5 mg/mL. P3MEEMT and P3HT polymers were dissolved in chlorobenzene with the concentration of 20 mg/mL. All polymer solutions were stirred overnight at 50 °C prior to spin coating. The substrates were cleaned sequentially by sonication in acetone and isopropanol for 15 min each. The surface of the substrate was then treated with oxygen plasma for 3 min before spin coating. The spin rate used is 600–2500 rpm to control film thickness between 20 nm to 120 nm. PB2T-TEG polymer films were annealed at 150 °C for 10 minutes under N_2 after spin-coating.

OECT device fabrication and characterization

OECT devices comprised lithographically patterned gold on glass substrates (see lithography process below) with transistor widths of 2.5 mm, 5 mm or 6 mm and lengths ranging from 10 μm to 600 μm. Polymers were spun casted onto OECT substrates and were carefully removed except at the electrode junction region via cotton tips (slightly dampened with acetone solution) under microscope or magnifying lens to ensure minimum impact on the transient response. A secure seal hybridization chamber (GRACE BIO LABS) is attached onto the substrate to confine the electrolyte. A Ag/AgCl pellet is used as the gate. The distance between gate and channel is fixed at approximately 4 mm in this study. The transfer curves were measured using two Keithley 2400 source-measure units controlled by custom Python code. The transient measurements were

conducted with NI PXIe-5451, NI PXIe-6366 and NI PXIe-8381 controlled by custom LabVIEW code with time resolution ≈ 10 μs.

The detailed lithography process: NR9-3000PY negative resist (Futurrex, Inc.) was deposited on cleaned glass wafers with diameter equals to 100 mm (University Wafer, Inc.) using Rite Track Automated Coater (SVG-90S), followed by UV light exposure (ABM-SemiAuto-Aligner) and resist development (SVG-90S). Metal deposition (10 nm chromium and 100 nm gold) was accomplished through evaporation (CHA Solution e-beam evaporator). The resist lift-off was achieved by soaking wafers in acetone solution overnight. The wafers were then diced using a Disco Wafer Dicer (Disco, America).

Operando microscope coupled with OECT characterization

An iPhone 11 Pro (1080 P, 240 fps) was attached to Leica CME microscope with a 15× eyepiece, a 10× objective (NA = 0.25) and a 650 nm long pass filter (FEL0650, THORLABS) for video recording. Videos were analyzed using custom Python code with OpenCV library. A dark and a reference image were taken for dark and flat field frame corrections, and absorbance calculation. To optimize the video contrast, a thicker PB2T-TEG film was prepared by drop casting from 1 mg/mL chlorobenzene solution to slow down the evaporation rate.

Spectroelectrochemistry characterization

The ultraviolet-visible (UV-Vis) absorption spectra were measured using an AVANTES spectrometer (AvaSpec-2048L) coupled with an AVANTES light source (Avalight-HAL-S). Doping and dedoping UV-Vis spectra were collected using continuous mode (with AvaSoft software) with time resolution ≈10 ms/spectrum. The potential bias is controlled using a Metrohm Autolab PGSTAT204 (with NOVA Software version 2.1). Polymers were cast onto fluoride-doped tin oxide-coated glass (FTO, Sigma-Aldrich, 7 Ω/sq) and used as a working electrode. A Ag/AgCl

electrode and a Pt mesh were used as reference electrode and counter electrode, respectively. All three electrodes were submerged into a cuvette containing ≈ 2.5 mL of either 0.1 M $KCl_{(aq)}$ or 0.1 M $KTFSI_{(aq)}$.

3.5 Author Contributions

J.G. and S.E.C. contributed equally to the work. J.G., S.E.C. and D.S.G. conceived the project, designed the experiments, and discussed the results together. J.G. and S.E.C. performed the experiments and analyzed the data. S.E.C. wrote the first draft and J.G. made the figures. R.G. performed the SPICE circuit modeling. C.G.B designed the preliminary microscope experiment. K.Y., Z.S., and C.-Z.L. provided the PB2T-TEG polymer. J.W.O. and C.K.L. provided the P3MEEMT polymer. J.G., S.E.C., R.G. and D.S.G. revised the manuscript with input from all the authors.

3.6 Acknowledgements

This paper is based on research supported primarily by the National Science Foundation, DMR-2003456. K.Y., Z.S., and C.-Z.L. thank the support from National Natural Science Foundation of China (22125901) for supporting synthesis of the PB2T-TEG polymer. J.W.O. and C.K.L.'s contributions to P3MEEMT polymer synthesis are based in part on work supported by the National Science Foundation DMREF-1922259. Part of this work (transistor fabrication) was conducted at the Washington Nanofabrication Facility/Molecular Analysis Facility, a National Nanotechnology Coordinated Infra- structure (NNCI) site at the University of Washington with partial support from the National Science Foundation via awards NNCI-1542101 and NNCI-2025489.

Chapter 4. SYNTHESIS AND CHARACTERIZATIONS OF NEW POLYTHIOPHENE DERIVATIVES FOR ORGANIC ELECTROCHEMICAL TRANSISTOR APPLICATIONS

4.1 INTRODUCTION

To further explore the effect of polymer side chain and ion species on OECT device performance, we proposed to synthesize polythiophene derivatives with sulfide or nitrile functional groups. Figure 4-1 shows the three targeted polymer structures: P3CEEBT, poly(3-cyanoethoxyethoxybutylthiophene), P3MTEEBT, poly(3-methylthioethoxyethoxybutylthiophene) and P3MEEBT, poly(3-methoxyethoxyethoxybutylthiophene). Most of the OECT studies to date focus on OMIECs with ethylene glycol (EG) functional groups or mixed EG/alkyl side chains. We planned to explore OECT device performance with OMIECs containing sulfide or nitrile functional groups.

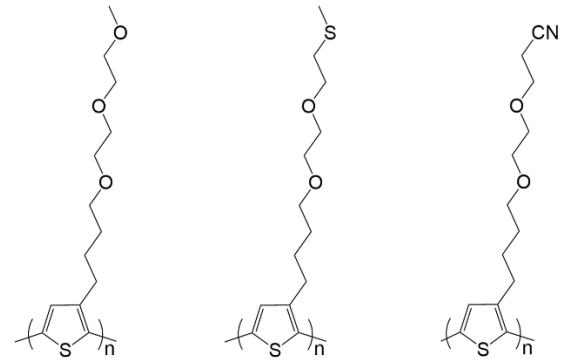

Figure 4-1. Structure of proposed new polythiophene derivatives.

With the proposed polymer structures, our aims are: (1) Compare the OECT device performance between P3MEEBT and P3MEEMT, which both have three EG functional groups on the side chain but with different alkyl spacer length. Previously, Onorato et al had demonstrated that by replacing the ethylene glycol unit close to the backbone with alkyl unit, the crystallinity along with the electronic conductivity of polymer film is improved.[60] Based on our results in Chapter 2, we also show that the OECT volumetric capacitance (C^*) is proportional to the amount of polar functional groups on the side chain (P3MEEMT vs P3APPT vs P3AAPT). It is thus interesting to compare the OECT performance of P3MEEBT and P3MEEMT. In specific, we hypothesize that P3MEEBT may show similar C^* but higher OECT mobility compared to P3MEEMT. (2) Compare the effect of oxygen, sulfur, and nitrile functional groups on mixed conductions. Since the polarity of ether functional group is in between sulfide and nitrile, we could explore the effect of side chain functional group polarity to OECT performance. We substitute the EG unit farther from polymer backbone with sulfide or nitrile functional group because the polar functional group farther from polymer backbone appears to exhibit larger impact on OECT performance based on our results in Chapter 2 (P3AAPT vs. P3PAAT).

We applied Kumada catalyst-transfer polymerization (KCTP) for polymer synthesis. To synthesize polymer with conjugated structure, cross-coupling reactions (carbon-carbon bond formation) are necessary. Among all the commonly used cross-coupling reactions like Suzuki, Stillie or Negishi, KTCP is known for its chain-growth mechanism. Chain-growth polymerization is favorable as the polymerization process is more controllable in terms of molecular weight and dispersity compared to step-growth polymerization. In addition, KCTP is known for its robustness to synthesize regioregular poly(3-hexylthiophne), P3HT with controlled molecular weight and low dispersity. Molecular weight, dispersity and regioregularity are all important factors that determine

electronic charge transport in OFETs. The three major stages of KCTP: in-situ Grignard metathesis (GRIM) (monomer preparation), chain initiation and propagation by adding Ni catalyst, and finally chain termination with the addition of concentrated HCl or methanol. More KCTP details could be found in the review.[111] Notably, because of the necessity of Grignard exchange during monomer preparation stage, additional attention is required when designing the monomer structure. For example, hydroxyl group in the monomer may need to be protected prior to KCTP and deprotected after polymerization.[68]

Here, we successfully synthesized new polythiophene derivatives, P3MEEBT and P3MTEEBT via KCTP. We then characterized their OMIECs performance through XRD, EIS and spectroelectrochemistry. Compared to P3MEEMT, we attributed the slightly lower volumetric capacitance of P3MEEBT to the increased alkyl fraction on the side chain. We did not find significant improvement in terms of μC^* when the end oxygen atom on the side chain is replaced with sulfur (P3MEEBT vs P3MTEEBT). Notably, we verified that higher polymer crystallinity indeed reduces the OECT electronic carrier mobility, agrees with our previous study.[24]

4.2 RESULTS AND DISCUSSIONS

4.2.1 *Material Synthesis*

The synthesis routes of P3MEEBT, P3MTEEBT and P3CEEBT are shown in Figure 4-2, Figure 4-3, and Figure 4-4, respectively. To use KCTP polymerization, synthesis of 2, 5-dibromo-thiophenes with desired side chains is necessary. P3MEEBT and P3MTEEBT share similar synthetic routes, while the synthetic route of P3CEEBT is more complex due to the reactivity of the end nitrile group. All reactions were performed under air-free conditions using standard Schlenk techniques. More synthetic details are described in the following paragraphs.

To synthesize P3MEEBT and P3MTEEBT, the first step is to synthesize 3-(4-bromobutyl)thiophene. This reaction could be achieved by: (1) conduct Lithium-Bromine exchange at ~ -45 °C for ~ 10 min (2) precipitation of 3-lithiothiophene with the addition of dry THF for ~ 1 hour at ~ -45 °C (3) the addition of excess 1,4-dibromobutane at room temperature for 2 to 5 hours.[112–114] The yield for this reaction is typically 40 % to 50 %. Figure 4-5 shows the ^{1}H NMR of 3-(4-bromobutyl)thiophene. The synthesis of 2-((2‘-Methylthio)ethoxy)ethanol (sulfide side chain precursor) is a relatively straightforward substitution reaction with the yield ~ 80 % to 90 %.[115,116] Figure 4-6 shows the ^{1}H NMR of 2-((2‘-Methylthio)ethoxy)ethanol.

To tether polar functional groups onto thiophene unit, substitution reaction is completed by first mixing sodium hydride (NaH) and either 2-(2-Methoxyethoxy)ethanol or 2-((2‘-Methylthio)ethoxy)ethanol, followed by the addition of 3-(4-bromobutyl)thiophene, with conditions similar to reported by Onorato et al.[60] The yield for this reaction is typically 30 % to 40 %. Two portions of the N-bromosuccimide (NBS) is then added slowly under dark for the bromination of thiophene unit at 2 and 5 positions, with the yield ~ 70 %.[24,60] Figure 4-7 and Figure 4-8 show the ^{1}H NMR result of 3MEEBT and 3MTEEBT monomer, respectively. We noted that

the sequence of bromination step and the polar side chain tethering step are interchangeable. The synthesized monomers are typically stored in freezer.

For KCTP polymerization, given that the polymerization process is very sensitive to water (Grignard reagent) and oxygen (Ni catalyst), monomers were first degassed under high vacuum for at least 45 minutes and the water scavenging Grignard reagent, TIPMgBr was also used.[117] i-PrMgCl was used for in-situ GRIM, and Ni(dppp)Cl_2 or Ni(dppe)Cl_2 was used as Ni catalyst. Extra care needs to be given for the addition of catalyst, which is in the form of fine powder (may stick onto glass neck or weigh paper). The ratio between monomer and Ni catalyst determines the degree of polymerization (DP), which is typically aimed between 120 and 150. The addition of Ni catalyst also needs to be fast to minimize the contact between reaction solution and air. Figure 4-9 and Figure 4-10 show the ^{1}H NMR of P3MEEBT and P3MTEEBT, respectively. Table 4-1 shows the obtained polymer molecular wight information. The synthesis of P3MEEMT was accomplished by Dr. Jonathan W. Onorato. [24,60] The molecular wight is characterized by gel permeation chromatography (GPC) compared to polystyrene (PS) standard. Detailed protocol of KCTP polymerization used in this work could be found in the previous published studies.[24,25,60]

The synthesis of P3CEEBT is incomplete due to the low yield of intermediate products and the separation difficulty. 3-(4-hydroxybutyl)thiophene was synthesized with surprisingly much lower yield (~ 20 %) using either the proposed NaOH/DMSO approach or the literature approach (claimed 90% yield).[118] Figure 4-11 shows the ^{1}H NMR of 3-(4-hydroxybutyl)thiophene. The synthesis of 3-(4-tosylethoxyethoxybutyl)thiophene was accomplished by first mixing 3-(4-hydroxybutyl)thiophene with NaH followed by the addition of excess diethylene glycol ditosylate. This yield of this reaction is ~ 40 % and the ^{1}H NMR of 3-(4-tosylethoxyethoxybutyl)thiophene is shown in Figure 4-12. Surprisingly, the addition of sodium cyanide (NaCN) into 3-(4-

tosylethoxyethoxybutyl)thiophene solution gives both 3-cyanoethoxyethoxybutylthiophene (less) and its hydrolysis side product (more) even in the dry condition. In addition, the polarity of 3-(4-cyanoethoxyethoxybutyl)thiophene and 3-(4-hydroxybutyl)thiophene are very close (the two TLC spots overlap in the hexane/ethyl acetate system), suggesting the purity of 3-(4-tosylethoxyethoxybutyl)thiophene needs to be high to avoid residual 3-(4-hydroxybutyl)thiophene in the later product. The synthesis of P3CEEBT was thus deferred with all the adverse conditions described above.

Table 4-1. Polymer Molecular Weight Information

	M_n (GPC)	D (GPC)	M_n (H NMR)	Estimated DP
P3MEEMT	24.0 k	1.67	NA	112
P3MTEEBT	12.2 k	1.69	NA	45
P3MEEBT	23.5 k	1.29	23.5 k	90

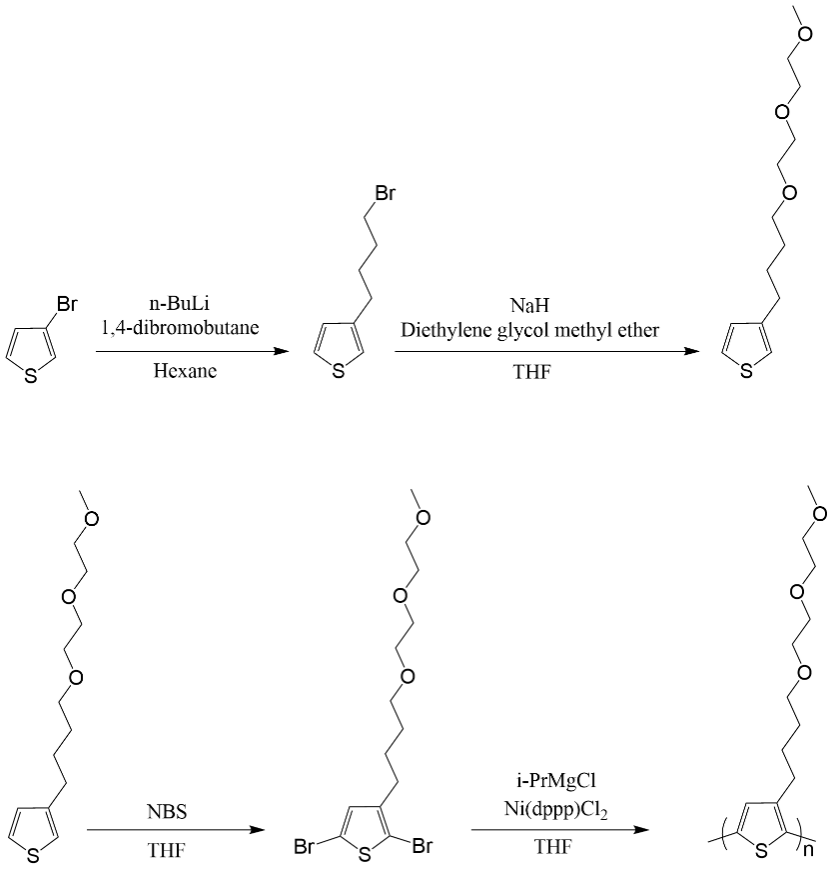

Figure 4-2. Scheme of synthetic route of P3MEEBT.

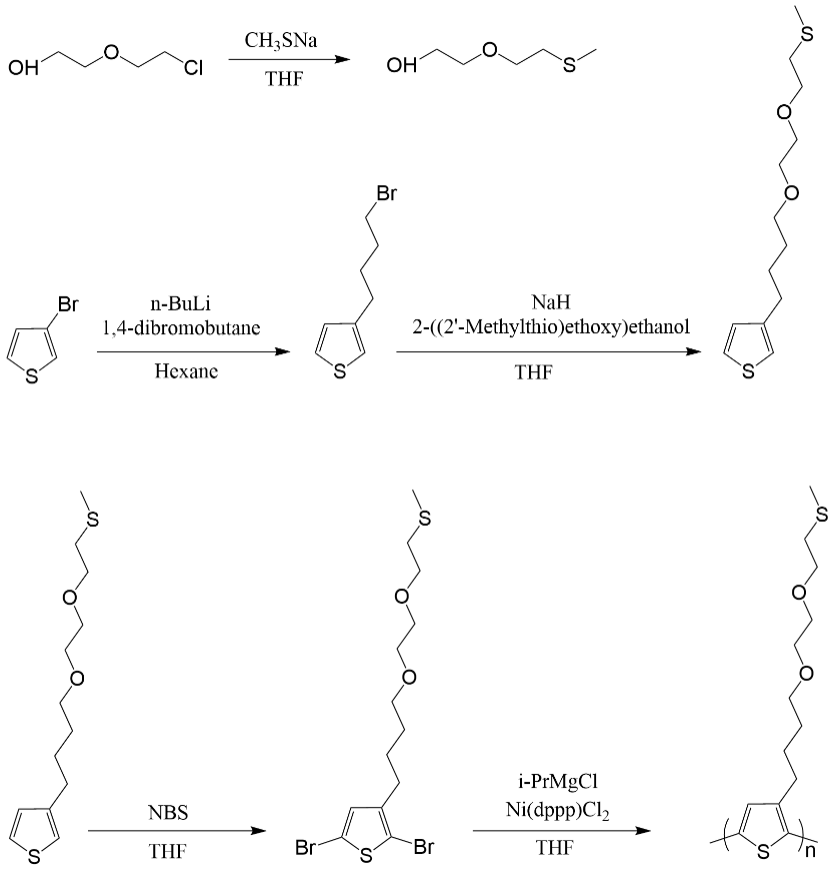

Figure 4-3. Scheme of synthetic route of P3MTEEBT.

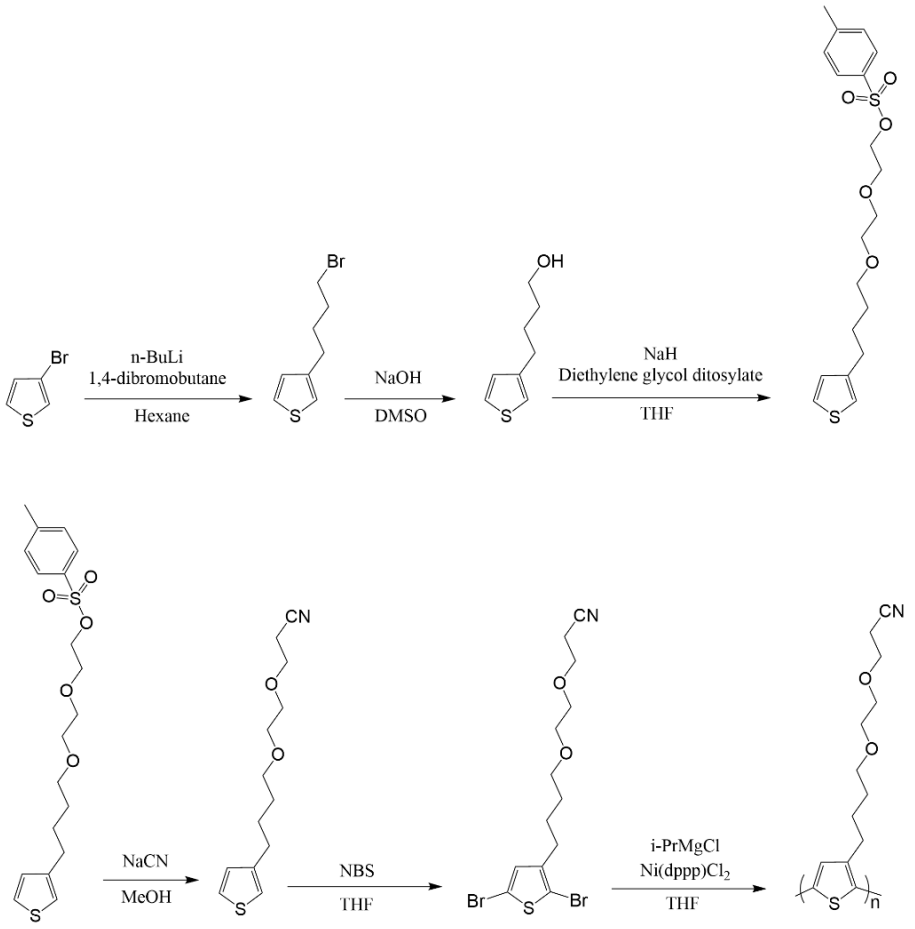

Figure 4-4. Scheme of synthetic route of P3CEEBT.

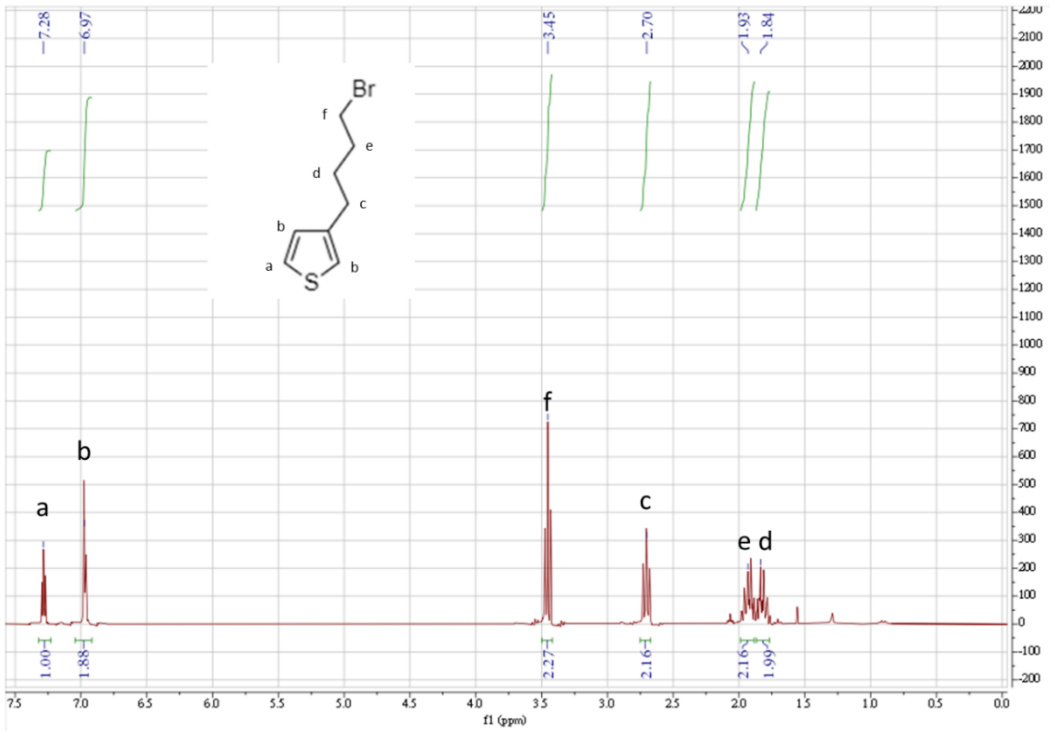

Figure 4-5. [1]H NMR of 3-(4-bromobutyl)thiophene.

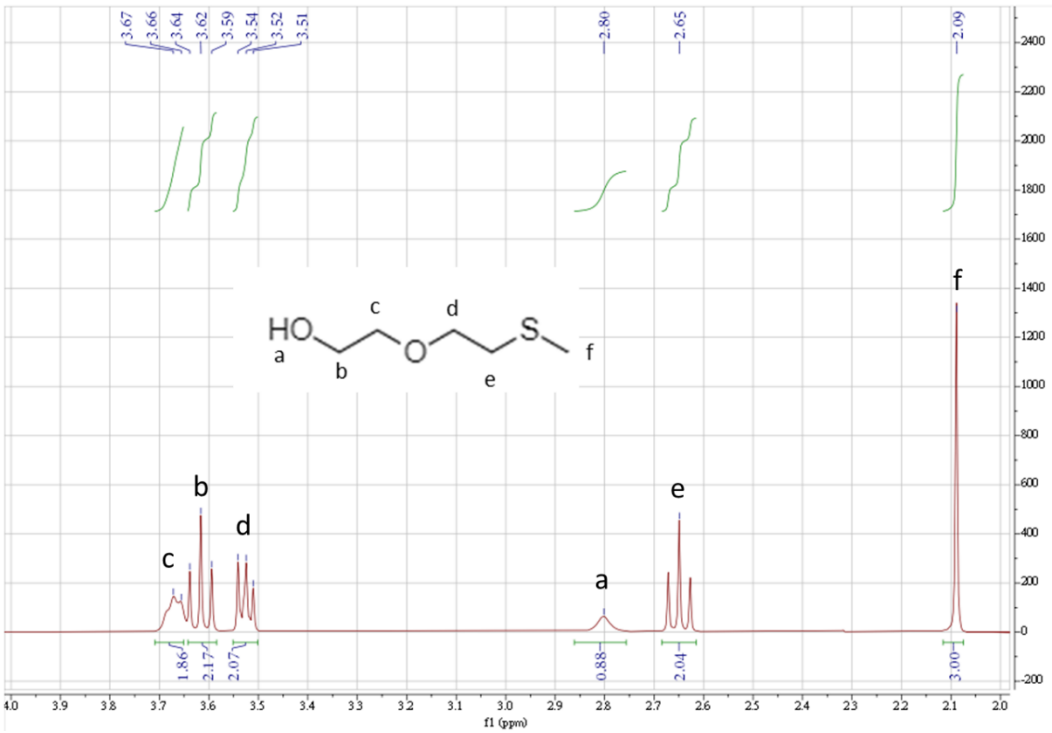

Figure 4-6. [1]H NMR of 2-((2‘-Methylthio)ethoxy)ethanol.

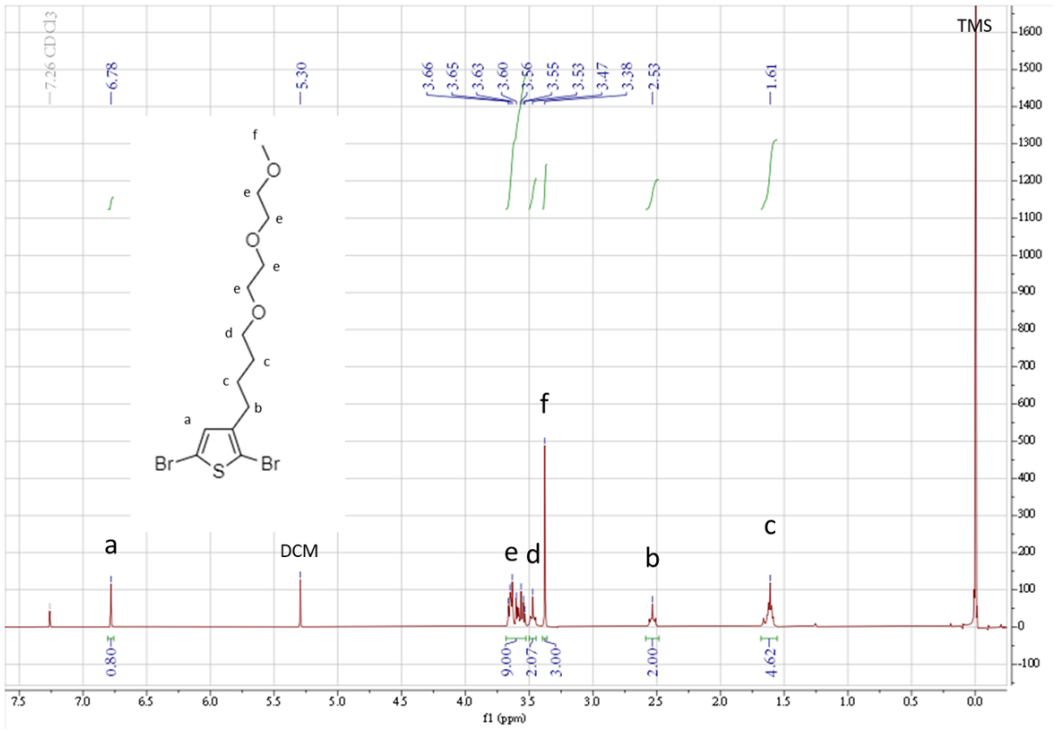

Figure 4-7. ^{1}H NMR of 2,5-dibromo-3-(4-methoxyethoxyethoxybutyl)thiophene.

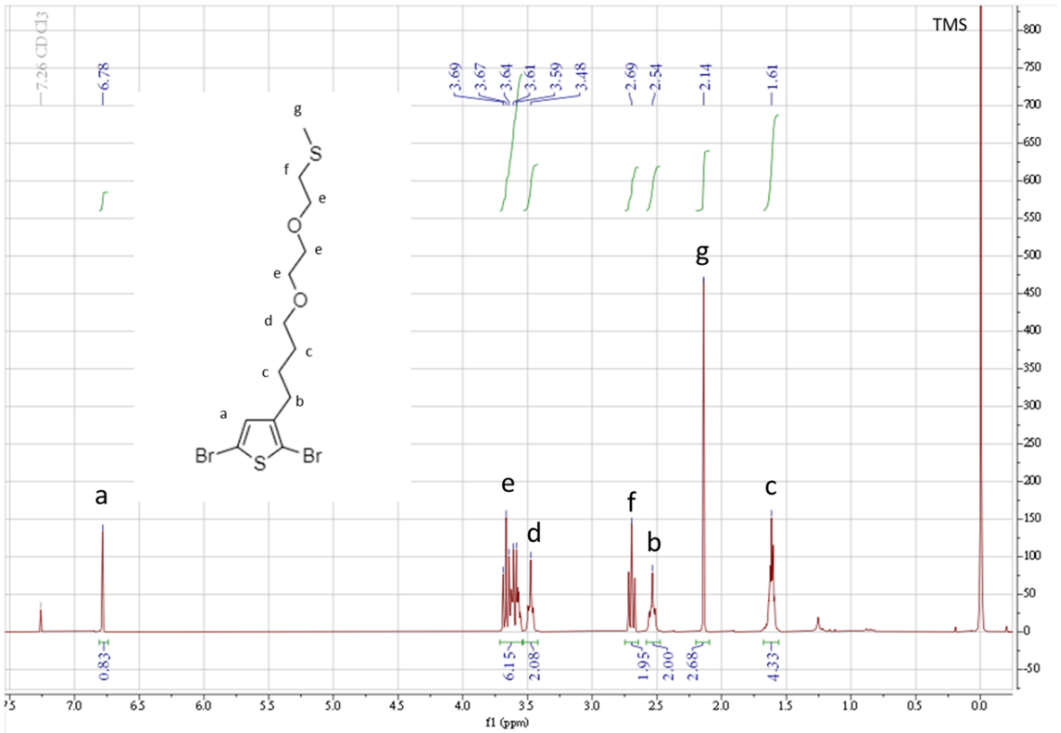

Figure 4-8. ^{1}H NMR of 2,5-dibromo-3-(4-methylthioethoxyethoxybutyl)thiophene.

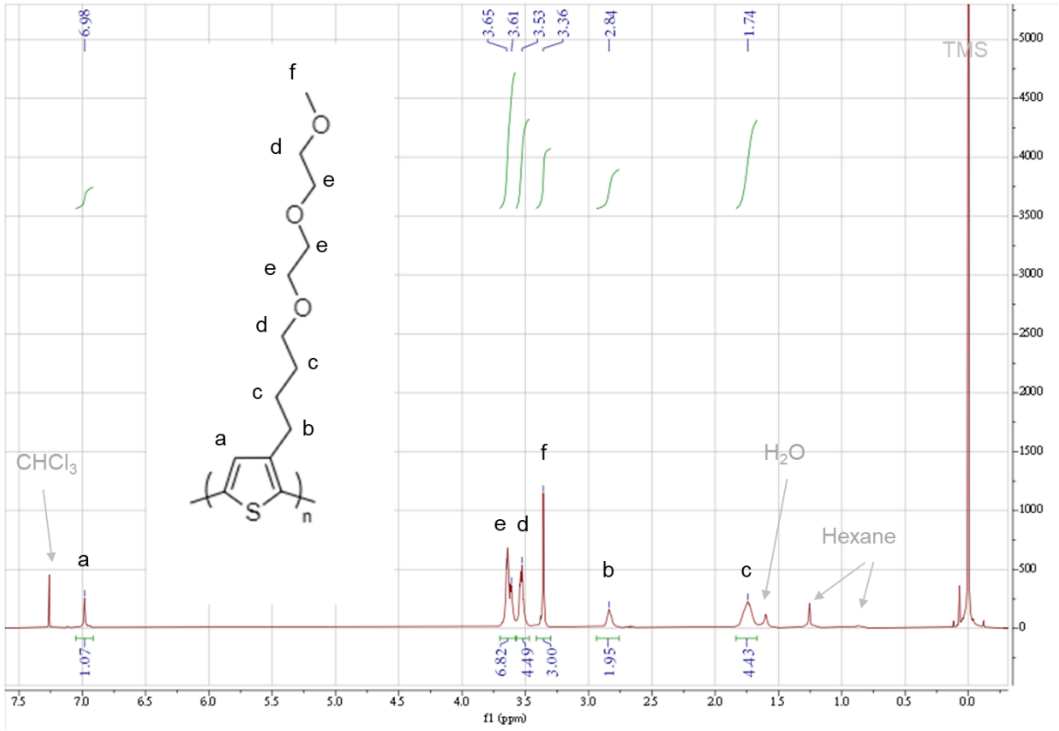

Figure 4-9. ^{1}H NMR of P3MEEBT.

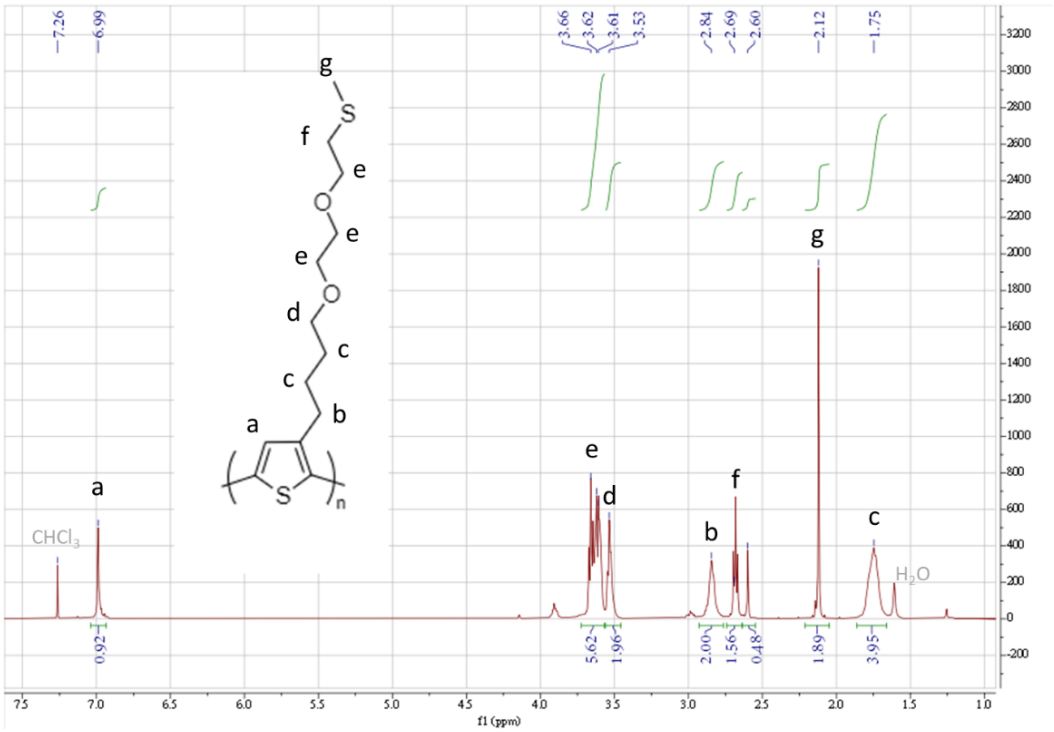

Figure 4-10. ^{1}H NMR of P3MTEEBT.

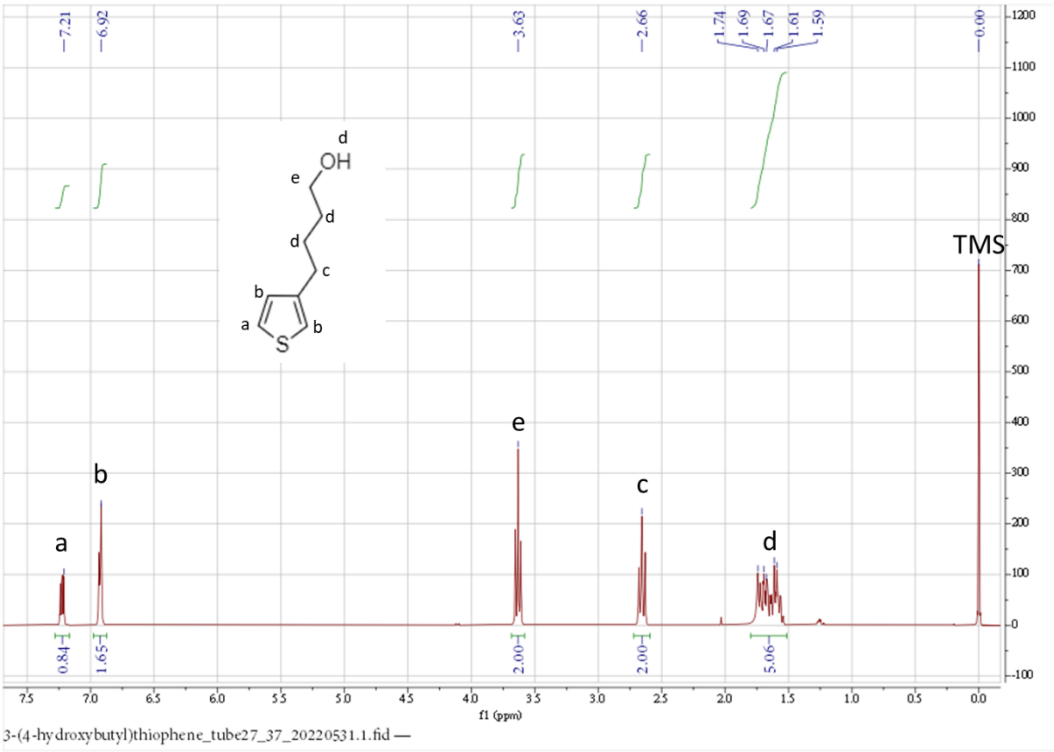

Figure 4-11. ^{1}H NMR of 3-(4-hydroxybutyl)thiophene.

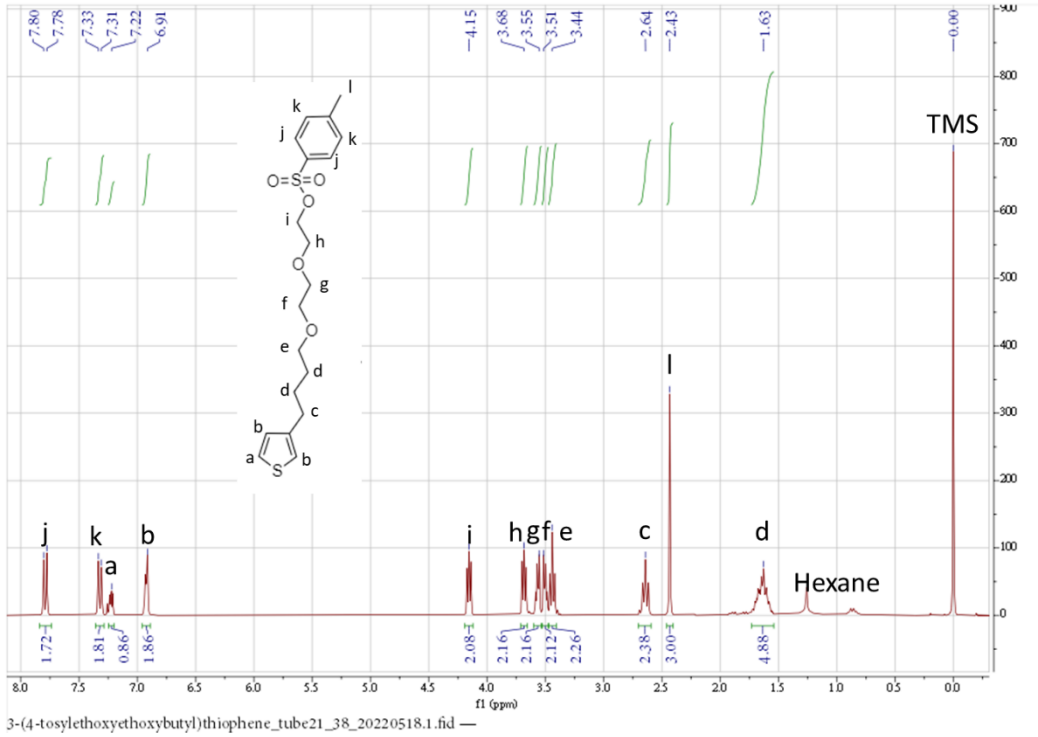

Figure 4-12. ^{1}H NMR of 3-(4-tosylethoxyethoxybutyl)thiophene.

4.2.2 *OMIECs Characterizations*

We first conducted X-ray diffraction (XRD) to characterize the OMIECs crystal structure. Figure 4-13 shows the XRD results of P3MEEMT, P3MTEEBT and P3MEEBT. We found higher film crystallinity for polythiophene derivatives with butyl spacer (3MTEEBT and P3MEEBT) compared to methyl spacer (P3MEEMT), which agrees with our previous studies.[25,60] Table 4-2 shows the lamellar spacing of the three polymers. With three more carbon atoms on the side chain, P3MEEBT and P3MTEEBT show ~ 5 Angstrom larger lamellar spacing compared to P3MEEMT. In addition, P3MTEEBT exhibits slightly larger lamellar spacing compared to P3MEEBT as sulfur atom is slightly larger than oxygen atom.

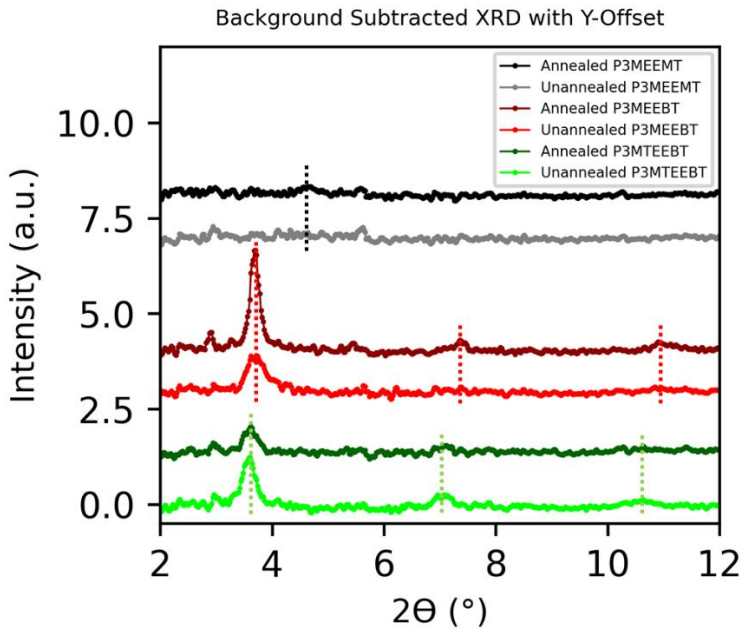

Figure 4-13. Polymer XRD results.

Table 4-2. Polymer Lamellar Spacing Information

	P3MEEMT	P3MTEEBT	P3MEEBT
2Θ of <100> peak	4.70	3.62	3.72
Lamellar spacing	18.8 Å	23.8 Å	24.4 Å

We further conducted spectroelectrochemistry and EIS to study the electronic band structure and doping behaviors of newly synthesized polythiophene derivatives. Since the M_n of as synthesized P3MTEEBT is about half of the P3MEEMT and P3MEEBT, and it is known that both μ and C* could be highly dependent on molecular weight,[48,100,119] we focused more on the comparison between P3MEEBT and P3MEEMT in the following sections.

Figure 4-14 shows UV-Vis-NIR spectra of P3MEEMT and P3MEEBT when various oxidation potentials applied. Similar to reference polymer P3MEEMT, P3MEEBT could be doped (oxidized) in 0.1 M KCl, with π-π^* peak (N) absorbance decreasing and polaron (P) and bipolaron (BP) peak increasing. We further compared the C^* of the two polymers via EIS as shown in Figure 4-15. P3MEEBT shows slightly higher C^* at lower doping level (0.3 V), implying lower doping onset and lower OECT threshold voltage. At higher doping level (0.7 V), P3MEEMT exhibits higher C^*, which may be attributed to the polar unit ratio on the side chain. Specifically, P3MEEMT has 3 ethylene glycol (EG) on the side chain (~100 %) while P3MEEBT has 1 alkyl and 3 EGs on the side chain (~75 %). Additionally, we found annealing has minimum impact to the C^*.

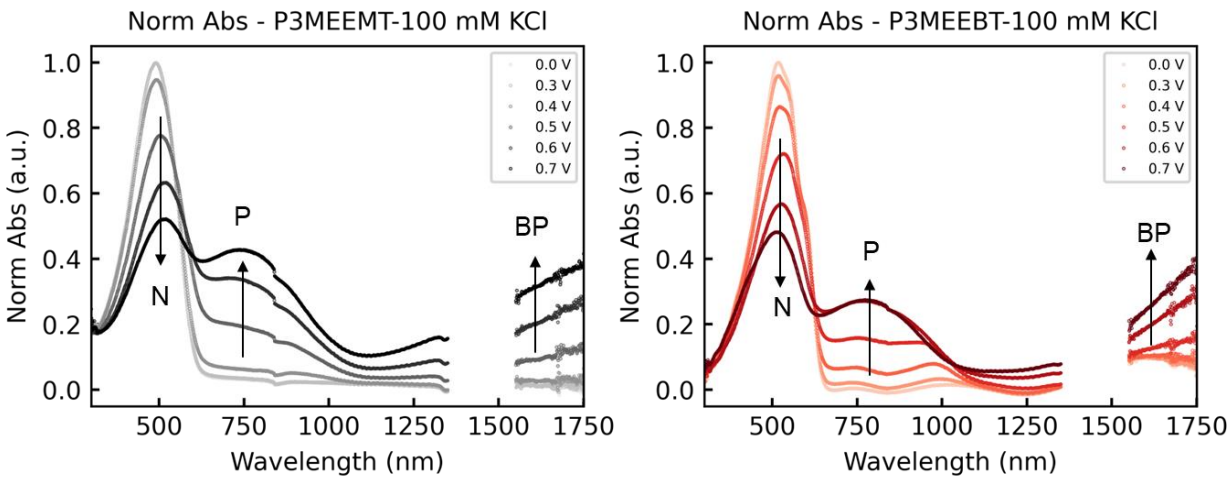

Figure 4-14. Polymer UV-Vis-NIR spectra at various doping potentials.

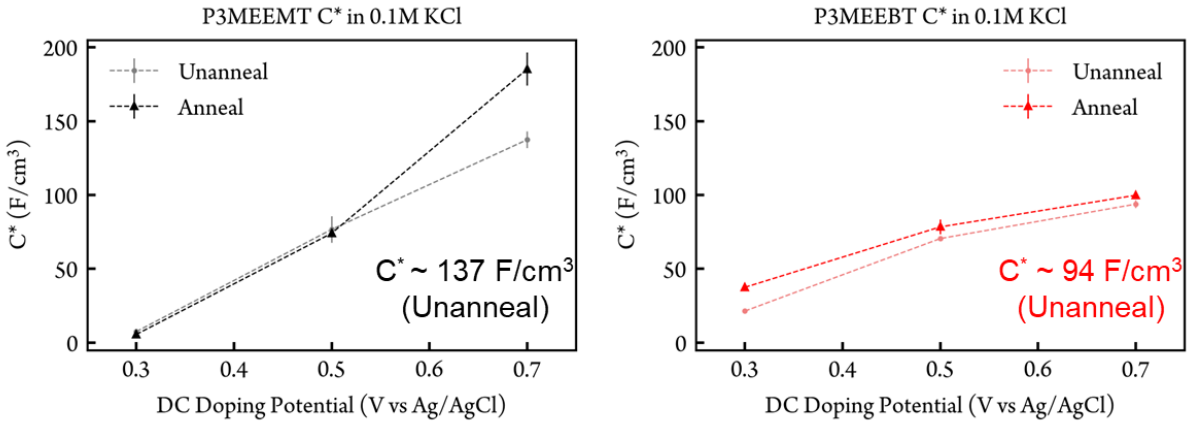

Figure 4-15. Polymer volumetric capacitance at various doping potentials.

4.2.3 *OECT Characterization*

We then compared the OECT performance of the polymers in 0.1 M KCl. Figure 4-16 shows the OECT transfer curves and transconductances. We found P3MEEMT based OECT shows higher I_{ON} and higher g_m compared to P3MEEBT based OECT. Notably, preliminary P3MTEEBT based OECT shows lower I_{ON} and lower g_m compared to P3MEEBT based OECT, implying the difference between 3 oxygen atoms and 2 oxygen atoms plus one sulfur atom on the side chain may be subtle, especially considering the device is operated in the hydrated condition. Figure 4-17 shows the threshold voltage of the polymers in 0.1 M KCl. We found the $|V_T|$ of P3MEEBT is ~ 0.1 V lower than P3MEEMT, which agrees with the EIS onset voltage result. We found that the effect of film annealing to the OECT V_T is unclear from this set of comparison.

Figure 4-18 shows the μC^* comparison of two polymers for both annealed and unannealed devices. Compared to P3MEEBT, P3MEEMT exhibits higher μC^* for both unannealed and annealed devices. And for both polymers, annealing lowers the μC^*. Using the C^* values obtained from EIS, we calculated the OECT mobility as shown in Figure 4-19. It is clear that higher crystallinity (P3MEEBT V.S. P3MEEMT; Anneal V.S. Unanneal) lowers the OECT mobility. This result agrees well with our group's previous work studied by Flagg et al.[24] Flagg et al hypothesized that the heterogeneous swelling in the polymer film lowers the OECT mobility for higher crystalline film. Specifically, in higher crystalline film, amorphous regions between crystalline domains swell more[24,100,120] and weaken the connection between crystalline regions in the film.

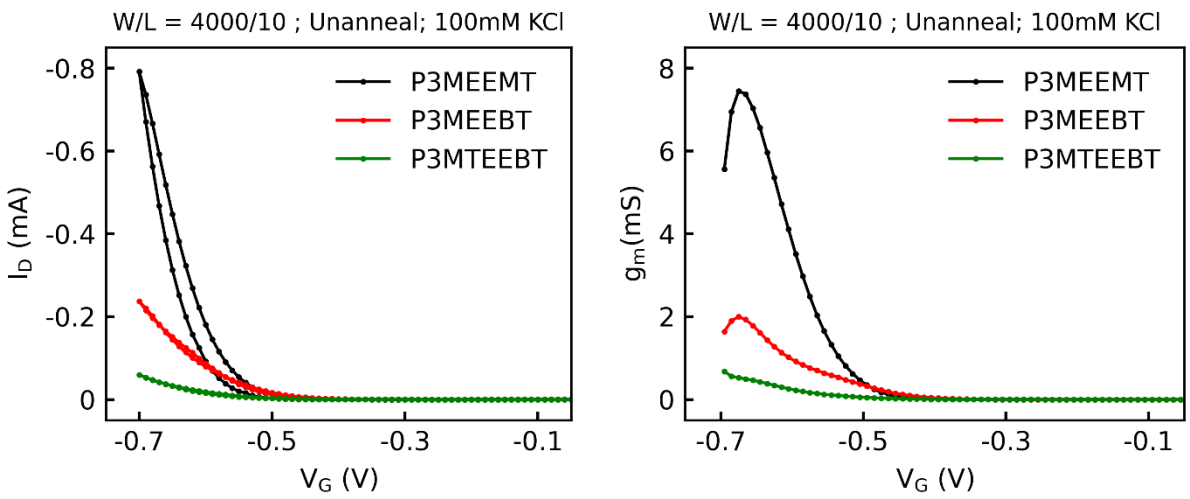

Figure 4-16. OECT transfer curves and transconductances in 0.1 M KCl.

Film thickness is ~ 60 nm, 80 nm, and 120 nm for P3MEEMT, P3MEEBT and P3MTEEBT.

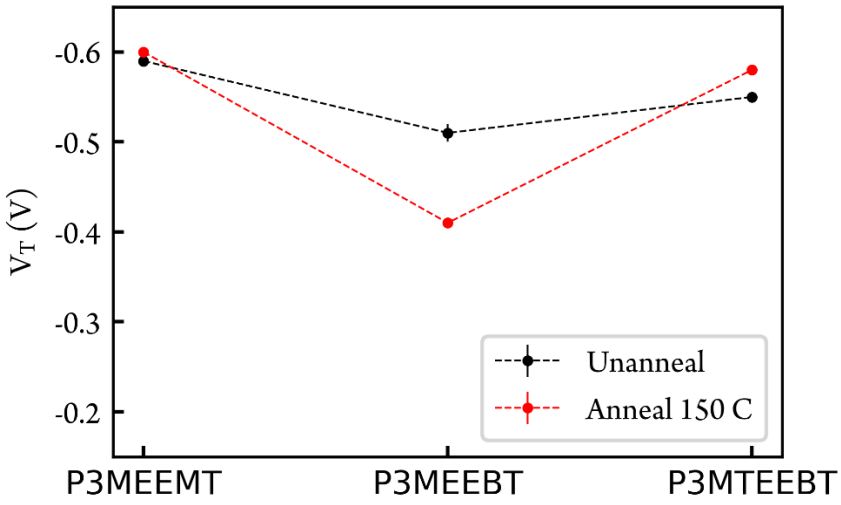

Figure 4-17. OECT threshold voltages in 0.1M KCl.

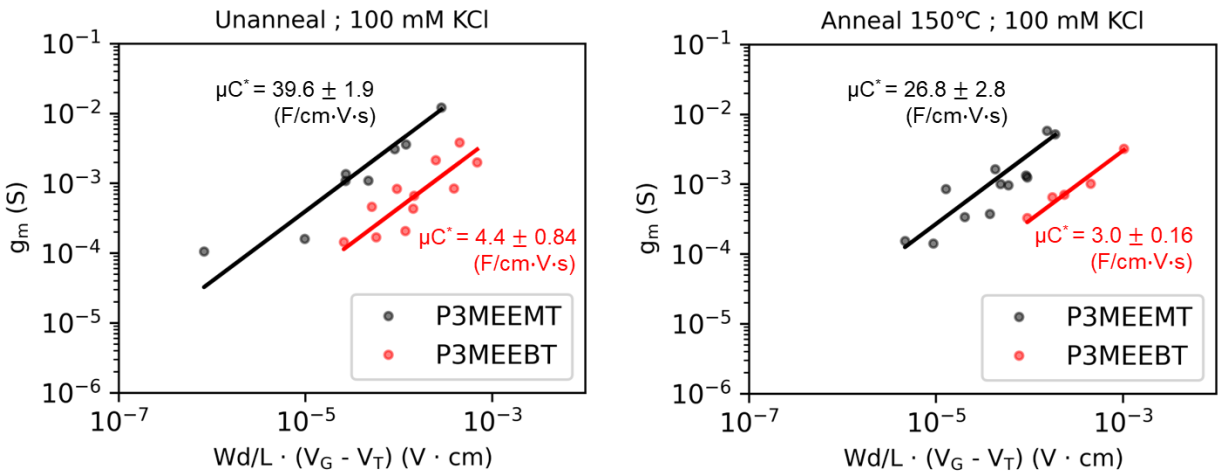

Figure 4-18. Comparison of μC* in 0.1 M KCl.

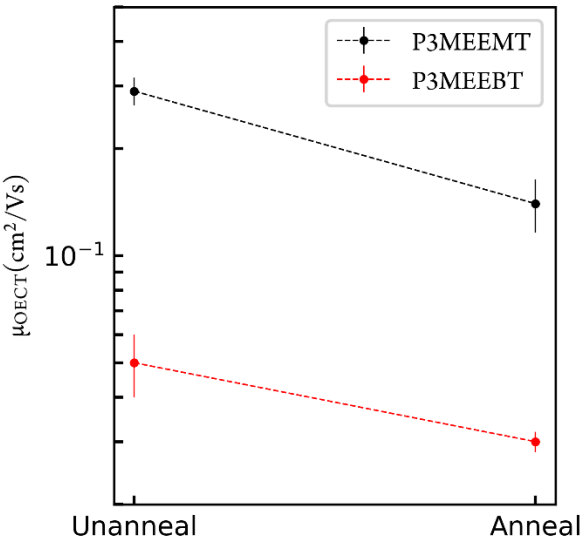

Figure 4-19. OECT mobility comparison.

4.3 CONCLUSIONS

We proposed the synthetic scheme of three new OMIECs containing polar functional groups including ethylene oxide, sulfide, and nitrile. Two of them (P3MEEBT and P3MTEEBT) were successfully synthesized and characterized. Compared to the reference P3MEEMT polymer, P3MEEBT and P3MTEEBT show higher film crystallinity due to increased spacing between polar functional groups and polythiophene backbone. We then compared the OECT performance of P3MEEMT and P3MEEBT with similar molecular weight. Notably, we verified that as opposed to OFET, higher film crystallinity indeed lowers the OECT mobility. We hypothesize that for the higher crystalline film, the intercrystallite connections are disconnected during OECT operation when more swelling occurs in amorphous region. In addition, we show lower I_{ON} and g_m for P3MTEEBT based OECTs compared to P3MEEBT, implying the difference between 3 oxygen atoms and 2 oxygen atoms plus one sulfur atom on the side chain may be subtle, especially considering the device is operated in the hydrated condition.

4.4 MATERIALS AND METHODS

Materials

N-bromosuccinimide (NBS) was purchased from Sigma-Aldrich and recrystallized from water before use. Anhydrous solvents were used for all reactions unless otherwise specified. THF was dried using a PureSolv solvent purification system. All other reagents were purchased from Sigma-Aldrich and used as received.

Methods

Monomer Synthesis and Characterizations

All reactions were performed under air-free conditions using standard Schlenk techniques. All reaction glassware was dried overnight in an oven at 120 °C prior to use. ^{1}H NMR was performed using a 300 MHz Bruker AV-300 instrument at 25 °C.

3-(4'-Bromobutyl)thiophene Synthesis

The synthesis of 3-(4'-Bromobutyl)thiophene synthesis could be found in the existing procedures.[113,121] Briefly, to a 3-neck 500 mL RFB, 3-Bromothiophene (14.05 mL, 0.15 mol) was degassed under vacuum for 5 minutes prior to adding the anhydrous hexanes solvent (150 mL). The solution was then cooled down to -40 °C to -50 °C using acetonitrile/dry ice bath. n-BuLi (2.5 M in hexane, 60 mL) was then added dropwise, and the solution was stirred for 10 min. Anhydrous THF was added dropwise via a syringe (18 - 20 mL) until the white 3-Lithiothiophene salt precipitated. The solution was then stirred for 1 h, after which the solution was allowed to warm to room temperature. Excess 1,4-Dibromobutane (150 mL, 0.6 mol) was added when the solution temperature was ~ -10 °C. The solution was then stirred for 3 h at room temperature and then

quenched with the addition of ~ 90 mL DI water. The reaction solution was then extracted with ether three times and the organic layer was dried over anhydrous $MgSO_4$, filtered, and concentrated. Excess 1,4-Dibromobuane was removed under vacuum. The crude product was purified using silica plug and then silica column chromatography both using hexanes as the eluent, resulting in 16.66 g (76 mmol) of a pale yellow oil as a product in a 50.6 % yield.

2,5-Dibromo-3-(4'-bromobutyl)thiophene Synthesis

To a 3-neck flask, 3-(4'-Bromobutyl)thiophene (8.76 g, 40 mmol) and 40 mL THF was added. The solution was degassed with nitrogen bubbling for 15 minutes. Following bubbling, recrystallized NBS (total: 14.17 g, 79.6 mmol) was added into the flask in 3 equal portions (5 minutes in between each addition). The reaction was then stirred overnight at room temperature with aluminum foil covered. The reaction solution was then filtered with fine frit, and THF was removed using rotary evaporation. The crude product (15.67 g) was purified using column chromatography using hexanes as the eluent, resulting in pale yellow oil in 35% yield (5.57 g, 14 mmol). We note that the yield of this reaction should typically be ~ 70 % or higher. We suspect the lower yield of this batch of reaction is due to the crude product being left in ambient for too long before column chromatography.

2,5-Dibromo-3-(4'-(methoxyethoxyethoxy)butyl)thiophene (3MEEBT) Synthesis

Diethylene glycol monomethyl ether (0.70 mL, 6 mmol) was added into 100 mL RFB and degassed under vacuum for 5 minutes. THF (15 mL) was then added into RFB to dissolve Diethylene glycol monomethyl ether. Sodium hydride (NaH, 6.5 mmol, 60% dispersion in mineral oil, 0.26 g) was quickly added in one portion, and the NaH was allowed to react for 1 h. 2,5-Dibromo-3-(4'-

bromobutyl)thiophene (1.88 g, 5 mmol) was dissolved in THF (5 mL). The 2,5-Dibromo-3-(4'-bromobutyl)thiophene solution was then added dropwise into Diethylene glycol monomethyl ether/NaH solution, then stirred at room temperature overnight. The reaction mixture was filtered over a thin pad of Celite, then the product was washed through with THF. The solvent was removed using rotary evaporation, and the product was purified through column chromatography with the hexanes/ethyl acetate (60%/40%) eluent. The product was pale yellow oil (0.80 g, 1.9 mmol, 38 % yield), and was stored at -20 °C. The above procedure was repeated multiple times with similar/larger scale to obtain enough monomers for polymerization.

2-((2'-Methylthio)ethoxy)ethanol Synthesis

The synthesis of 2-((2'-Methylthio)ethoxy)ethanol could be found in the existing procedures.[115,116] Briefly, Sodium methanethiolate (NaSMe, 5.1 g, 73 mmol) was added into 500 mL RFB with THF (200 mL). 2-(2'-Chloroethoxy)ethanol (6 mL, 57 mmol) was then slowly added into the RFB. The solution was then heated to reflux for overnight. The mixture was cooled to ambient temperature, and DI water (~ 50 mL) was added to dissolve the salts formed. The solution was then extracted three times using chloroform. The organic fractions were combined and dried with $MgSO_4$. The drying agent was filtered off, and the solvent was removed by rotary evaporation. The product was a pale, yellow oil (6.54 g, 48 mmol) with 84 % yield.

2,5-Dibromo-3-(4'-(methylthioethoxyethoxy)butyl)thiophene (3MTEEBT) Synthesis

2-((2'-Methylthio)ethoxy)ethanol (0.82 g, 6 mmol) was added into 100 mL RFB and degassed under vacuum for 5 minutes. THF (15 mL) was then added into RFB to dissolve 2-((2'-Methylthio)ethoxy)ethanol. Sodium hydride (NaH, 6.5 mmol, 60% dispersion in mineral oil, 0.26

g) was quickly added in one portion, and the NaH was allowed to react for 30 min to 1 h. 2,5-Dibromo-3-(4'-bromobutyl)thiophene (1.88 g, 5 mmol) was dissolved in THF (5 mL). The 2,5-Dibromo-3-(4'-bromobutyl)thiophene solution was then added dropwise into 2-((2'-Methylthio)ethoxy)ethanol /NaH solution, then stirred at room temperature overnight. The reaction mixture was filtered over a thin pad of Celite, then the product was washed through with THF. The solvent was removed using rotary evaporation, and the product was purified through column chromatography with the hexanes/ethyl acetate (85%/15%) eluent. The product was a pale, yellow oil (0.66 g, 1.3 mmol, 26 % yield), and was stored at -20 °C. The above procedure was repeated multiple times with similar or larger scale to obtain enough monomers for polymerization.

Polymer Synthesis and Characterizations

P3MEEBT and P3MTEEBT were synthesized using Kumada Catalyst Transfer Polymerization (KCTP). The produced polymer was characterized via size-exclusion chromatography (SEC), using a Malvern Viscotek TDA 305 GPC equipped with UV and refractive index detectors. THF was used as an eluent at a temperature of 40 °C and a flow rate of 1 mL/min. Molecular weight information was determined relative to polystyrene standards. ^{1}H NMR was performed using a 500 MHz Bruker AV-500 instrument at 25 °C.

Poly(3-(4'-(methoxyethoxyethoxy)butyl)thiophene) (P3MEEBT) Synthesis

To a 3-neck 100 mL RFB, 3MEEBT monomer (1.25 g, 3 mmol) was added, then degassed under high vacuum for 75 min. The flask was placed under nitrogen, and 30 mL of THF was added. The flask was cooled to 0 °C, and the water scavenger TIPMgBr (0.5 M in THF, 3 mL, 1.5 mmol) was added and the solution was stirred for 10 minutes.[117] i-PrMgCl (1.88 M in THF, 1.57 mL, 2.95

mmol, titrated before use) was then added dropwise over 10 min. The flask was allowed to warm to room temperature, and then stirred for 1 h. The flask was then heated to 45 °C, and Ni(dppe)Cl_2 (10.56 mg, 0.02 mmol) was quickly added. The polymerization was stirred at 45 °C for 4 hours, then quenched by the addition of 3 mL of 5 M HCl. The polymer solution was poured into ~ 200 mL of MeOH with precipitation observed after quick stirring and left in 4 °C overnight. The precipitated polymer was collected with a cellulose thimble (Whatman). The polymer was further purified with Soxhlet extraction using MeOH and $CHCl_3$. The $CHCl_3$ fraction was dried via rotary evaporator and left overnight in a vacuum oven. Mass of the collected P3MEEBT polymer is ~ 341 mg (M_n = 23.5 kg/mol, Đ = 1.29).

Poly(3-(4'-(methylthioethoxyethoxy)butyl)thiophene) (P3MTEEBT) Synthesis

To a 3-neck 100 mL RFB, 3MTEEBT monomer (1.16 g, 2.67 mmol) was added, then degassed under high vacuum for 70 min. The flask was placed under nitrogen, and 26.7 mL of THF was added. The flask was cooled to 0 °C, and the water scavenger TIPMgBr (0.5 M in THF, 2.67 mL, 1.34 mmol) was added and the solution was stirred for 10 minutes.[117] i-PrMgCl (1.88 M in THF, 1.39 mL, 2.62 mmol, titrated before use) was then added dropwise over 10 min. The flask was allowed to warm to room temperature, and then stirred for 1 h. The flask was then heated to 45 °C, and Ni(dppe)Cl_2 (9.40 mg, 0.018 mmol) was quickly added. The polymerization was stirred at 45 °C for 5 hours, then quenched by the addition of 3 mL of 5 M HCl. The polymer solution was poured into ~ 200 mL of MeOH with precipitation observed after quick stirring and left in 4 °C overnight. The precipitated polymer was collected with a cellulose thimble (Whatman). The polymer was further purified with Soxhlet extraction using MeOH and $CHCl_3$. The $CHCl_3$ fraction

was dried via rotary evaporator and left overnight in a vacuum oven. Mass of the collected P3MTEEBT polymer is ~ 344 mg (M_n = 12.2 kg/mol, Đ = 1.69).

X-ray diffraction (XRD)

XRD of polymer thin films on glass substrates were measured using a Bruker D8 Discover with a Pilatus 100K large area 2D detector.

Spectroelectrochemistry characterization

The ultraviolet-visible-near IR (UV-Vis-NIR) absorption spectra were measured using an AVANTES spectrometer (AvaSpec-2048L) coupled with an AVANTES light source (Avalight-HAL-S). The potential bias is controlled using a Metrohm Autolab PGSTAT204 (with NOVA Software version 2.1). Polymers were cast onto fluoride-doped tin oxide-coated glass (FTO, Sigma-Aldrich, 7 Ω/sq) and was used as a working electrode. A Ag/AgCl electrode and a Pt mesh was used as reference electrode and counter electrode, respectively. All three electrodes were submerged into a cuvette containing ≈2.5 mL of 0.1M $KCl_{(aq)}$.

Electrochemical Impedance Spectroscopy (EIS) for C^* Determination

EIS measurements were performed on gold-coated glass substrates with a defined area of (0.01 or 0.04) cm^2. Polymers were spun casted on the gold substrates. A Ag/AgCl electrode and a Pt mesh was used as reference electrode and counter electrode, respectively. The polymer was first electrochemically doped at specific direct current (DC) potential bias (ranging from 0.2 V to 0.7 V vs Ag/AgCl) for 60 s, and the alternating current (AC) perturbation (Sine wave with 10 mV

amplitude and frequency from 10^5 Hz to 10^{-1} Hz) was then performed on top of the DC potential bias. The obtained EIS data was fit to Randles circuit[61,62]

OECT device fabrication and characterization

OECT devices comprised lithographically patterned gold on glass substrates (see lithography process below) with transistor lengths of 10 μm and widths ranging from 100 μm to 4000 μm. Polymers were spun casted onto OECT substrates and were carefully removed except at the electrode junction region via cotton tips under microscope. Cotton tips were slightly dampened with acetone solution. An insulating layer containing cellulose acetate and acrylates copolymer (Nail polish: Sally Hansen, Insta-Dry Top Coat) was then applied to avoid the direct contact between electrode and electrolyte during further characterizations. Devices were measured in degassed electrolytes. The electrolyte (≈ 1 mL) was contained in a polydimethylsiloxane (PDMS) reservoir during OECT measurements. The assembly of the OECT substrate, the PDMS reservoir and the electrical connections were achieved via a 3D-printed holder. Transfer curves were measured by varying V_G from 0 V to -0.7 V and then back to 0 V (vs. Ag/AgCl). The V_D was fixed at -0.6 V. For KCl electrolyte, the step size of V_G was 0.02 V with 5 s between each step.

The detailed lithography process: NR9-3000PY negative resist (Futurrex, Inc.) was deposited on cleaned glass wafers with diameter equals to 0.1016 m (University Wafer, Inc.) through spin-coating, followed by UV light exposure (ABM-SemiAuto-Aligner) and resist development. Metal deposition (10 nm chromium or titanium and 100 nm gold) was accomplished through sputtering (Evatec LLS EVO Sputter System) or evaporation (CHA Solution e-beam evaporator). The resist lift-off was achieved by soaking wafers in acetone solution overnight. The wafers were then diced using a Disco Wafer Dicer (Disco, America).

4.5 ACKNOWLEDGEMENTS

The polymer synthesis is based on work supported by the National Science Foundation DMREF-1922259. The OMIECs and OECT characterizations are based on work funded through the National Science Foundation DMR-2003456. Part of this work was conducted at the Washington Nanofabrication Facility / Molecular Analysis Facility, a National Nanotechnology Coordinated Infrastructure (NNCI) site at the University of Washington with partial support from the National Science Foundation via awards NNCI-1542101 and NNCI-2025489.

Chapter 5. CONCLUSIONS AND FUTURE DIRECTIONS

We present three studies investigating the operation of organic electrochemical transistors (OECTs) from both material and device perspective. In each case, both the static and transient behavior of OECTs are highly dependent on the choice of channel materials, or organic mixed ionic-electronic conductors (OMIECs) and electrolytes. The results and methods present here are based on classical planar OECTs using aqueous electrolyte, but we believe them to be universal for OECTs using solid electrolyte or with vertical or more complex structures.

In Chapter 2, we study the electrochemical doping/dedoping kinetics, and the OECT performance of a series of polythiophene homopolymers with ethylene glycol units in their side chains using both kosmotropic and chaotropic anion solutions were studied. We compare their performance to a reference polymer, P3MEEMT. We find larger OECT material figure of merit, μC^*, where μ is the carrier mobility and C^* is the volumetric capacitance, and faster doping kinetics with more oxygen atoms on the side chains, and if the oxygen atom is farther from the polythiophene backbone. Replacing the oxygen atom close to the polythiophene backbone with an alkyl unit increases the film π-stacking crystallinity (higher electronic conductivity in the undoped film) but sacrifices the available doping sites (lower volumetric capacitance C^* in OECT). We show that this variation in C^* is the dominant factor in changing the μC^* product for this family of polymers. With more oxygen atoms on the side chain, or with the oxygen atom farther from the polymer backbone, we observe both more passive swelling and higher C^*. In addition, we show that, compared to the doping speed, the dedoping speed, as measured via spectroelectrochemistry, is both generally faster and less dependent on ion species or side chain oxygen content. Last, through OECT, electrochemical impedance spectroscopy (EIS) and spectroelectrochemistry measurements, we show that the chaotropic anion PF_6^- facilitates higher doping levels, faster

doping kinetics, and lower doping thresholds compared to the kosmotropic anion Cl^-, although the exact differences depend on the polymer side chains. Our results here highlight the importance of balancing μ and C^* when designing molecular structures for OECT active layers.

In Chapter 3, we show existing models of device operation cannot explain the experimental observations that turn-off times are generally much faster than turn-on times in accumulation mode OECTs. Through operando optical microscopy, we image the local doping level of the transistor channel and show that device turn-on occurs in two stages, while turn-off occurs in one stage. We attribute the faster turn-off to a combination of engineering as well as physical and chemical factors including channel geometry, differences in doping and dedoping kinetics, and the physical phenomena of carrier density-dependent mobility. We show that ion transport is limiting the device operation speed in our model devices. Our study here provides insights into the kinetics of OECTs and guidelines for engineering faster OECTs.

In Chapter 4, we synthesize two new polythiophene derivatives, P3MEEBT and P3MTEEBT via KCTP polymerization. We do not find significant improvement in terms of C^* and μC^* when the end oxygen atom on the side chain (P3MEEBT) is replaced with sulfur atom (P3MTEEBT). Compared to the reference polymer P3MEEMT, we attribute the slightly lower volumetric capacitance of P3MEEBT to the increased alkyl fraction on the side chain. In addition, we verify that higher polymer film crystallinity slightly improves the OECT threshold voltage but reduces the OECT electronic carrier mobility, which agrees with our previous study. We hypothesize in the more crystalline film, amorphous regions between crystalline domains swell more and lower the connection between crystalline regions.

OECT represents as an exciting new type of transistor with the ability to couple ionic and electronic carriers. This unique ion-electron coupling behavior enables many promising OECT-

based applications including point-of care biosensors, neuromorphic computing, and artificial neurons. To commercialize these intriguing techniques, more understanding of the OECT operation mechanism, especially the OECT transient behavior and OECT cycling stability are still necessary. For the OECT transient behavior, though we have studied how different factors affect the OECT transient behavior in Chapter 3, the universal equations describing the time constants and operation variables are still lacking. In addition, our current understanding of OECT cycling stability is still limited. OMIECs with similar μC^* and doping kinetics could show dramatically different cycling stability.[33] Factors including oxidative degradation, oxygen reduction reactions, over swelling and active-layer delamination could all contribute to device deterioration. We expect more exciting work in these two sub-fields to come.

APPENDIX A: SUPPORTING INFORMATION FOR CHAPTER 2

Adapted with permission from S. E. Chen, L. Q. Flagg, J. W. Onorato, L. J. Richter, J. Guo, C. K. Luscombe and D. S. Ginger, J. Mater. Chem. A, 2022, 10, 10738[25]. Copyright 2022 Royal Society of Chemistry.

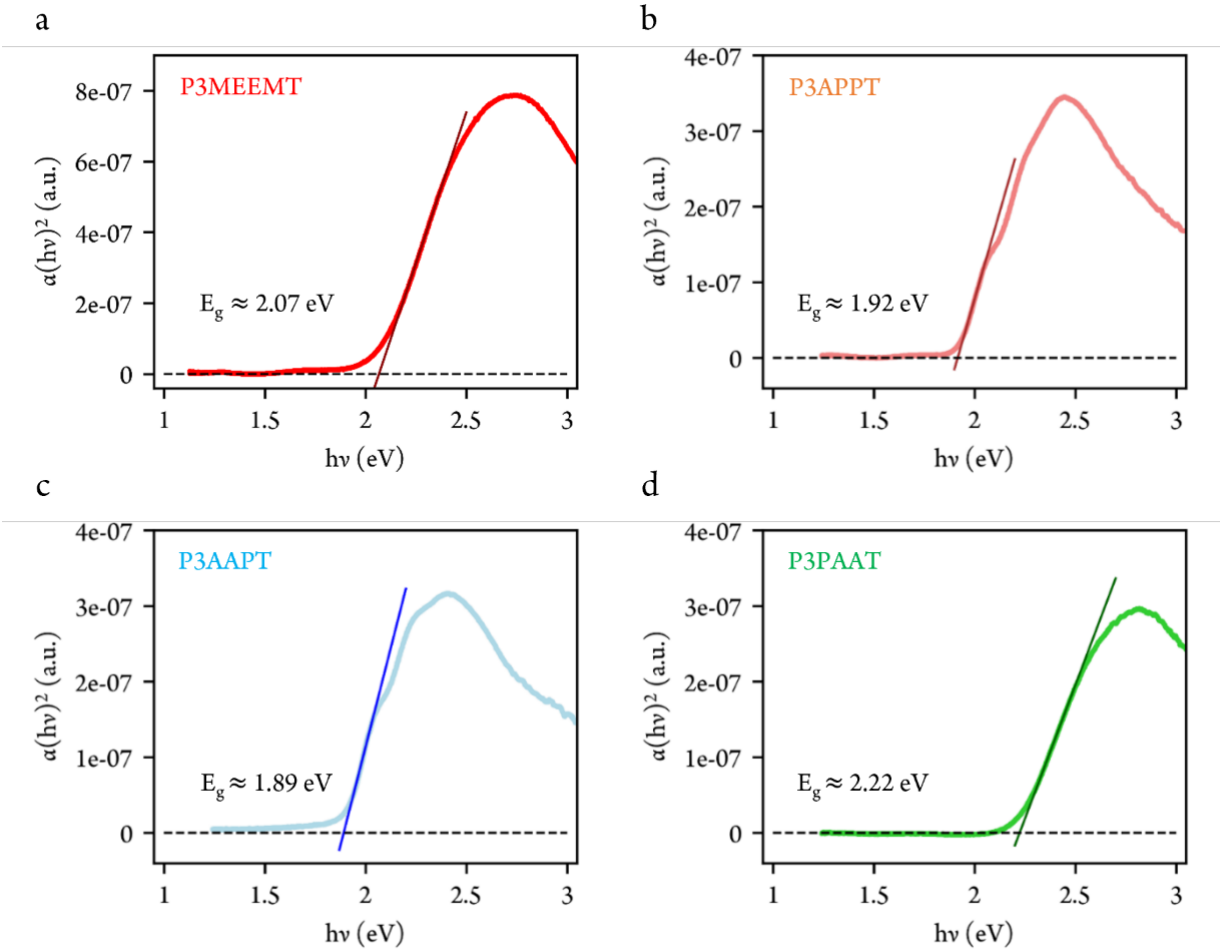

Figure A1. Determination of optical gap of polymers via Tauc plot.(a) P3MEEMT (b) P3APPT (c) P3AAPT (d) P3PAAT. Dash lines are a guide for the eye.

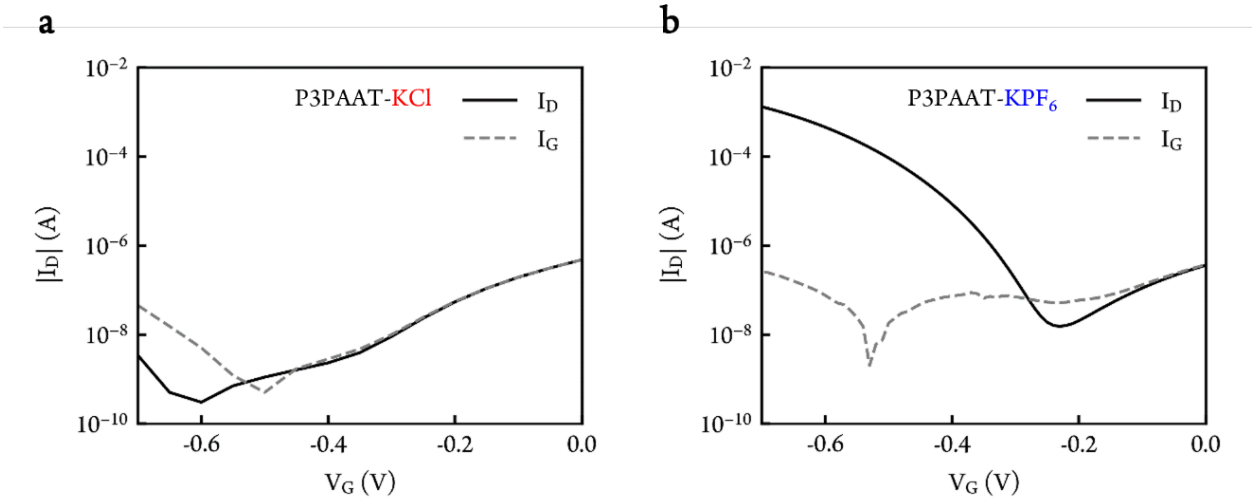

Figure A2. Organic electrochemical transistor, OECT, transfer curve of P3PAAT in (a) 100 mmol/L $KCl_{(aq)}$ and (b) 100 mmol/L $KPF_{6(aq)}$. Channel width/length = 4000 µm/10 µm. See main text for notation of polymer structure. Drain voltage, V_D = -0.6 V. Drain current, I_D. Gate voltage, V_G. Gate current, I_G.

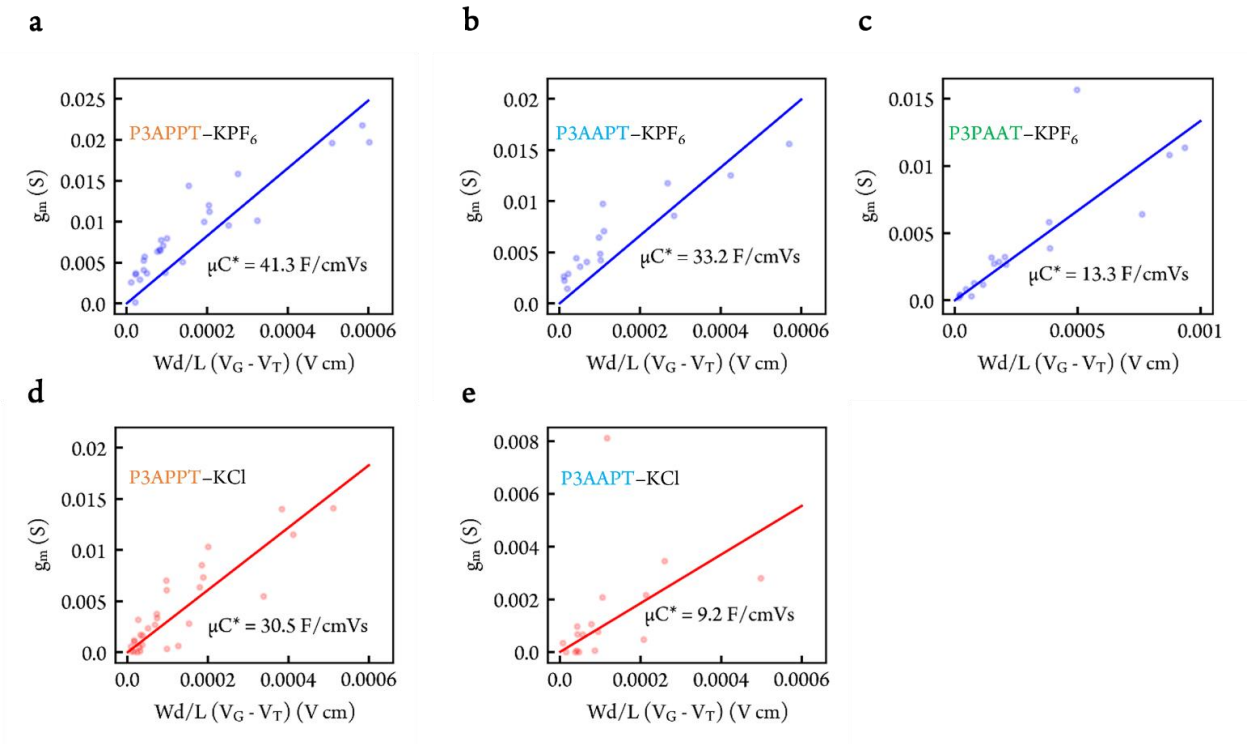

Figure A3. Determination of OECT figure of merit μC^* (μ carrier mobility and C^* volumetric capacitance) of reduced-oxygen-content side chain polymers in 100 mmol/L $KPF_{6(aq)}$ (a) P3APPT (b) P3AAPT (C) P3PAAT and in 100 mmol/L $KCl_{(aq)}$ (d) P3APPT (e) P3AAPT. Each data point represents one transistor device. See main text for notation of polymer structure.

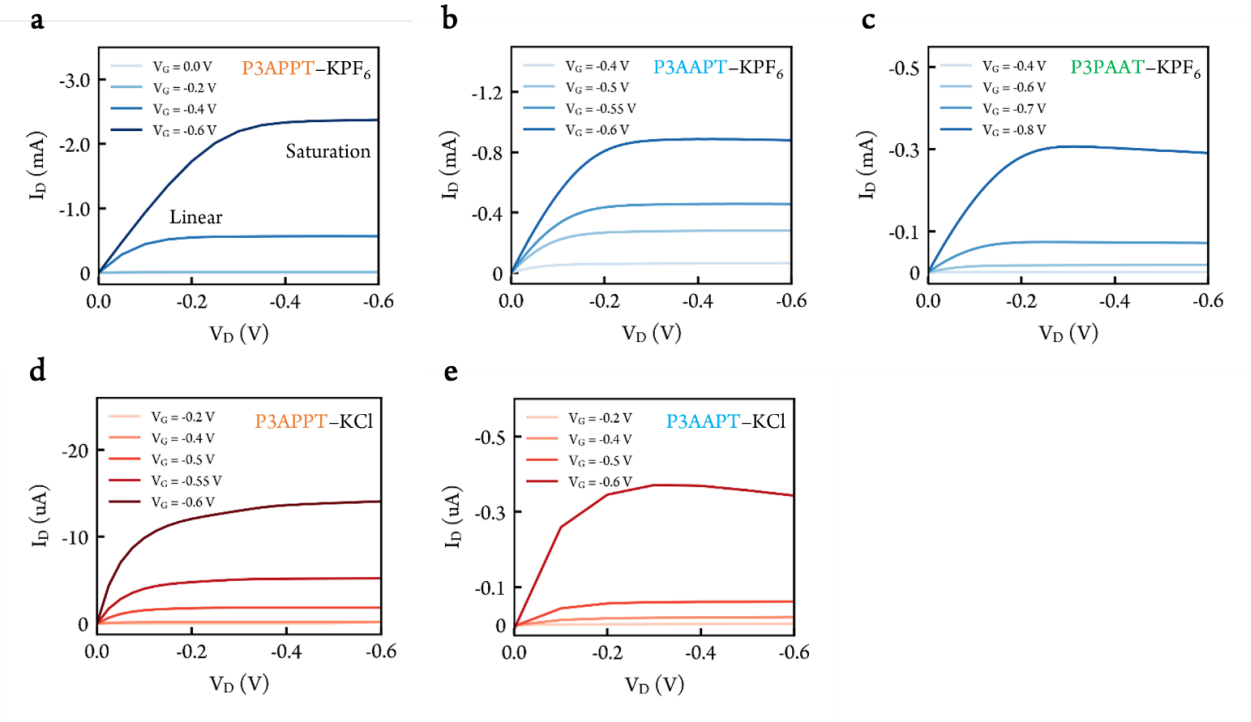

Figure A4. OECT output curves of reduced-oxygen-content side chain polymers in 100 mmol/L $KPF_{6(aq)}$ of (a) P3APPT (b) P3AAPT (C) P3PAAT and in 100 mmol/L $KCl_{(aq)}$ (d) P3APPT (e) P3AAPT. Channel width/length = 800 µm/10 µm.

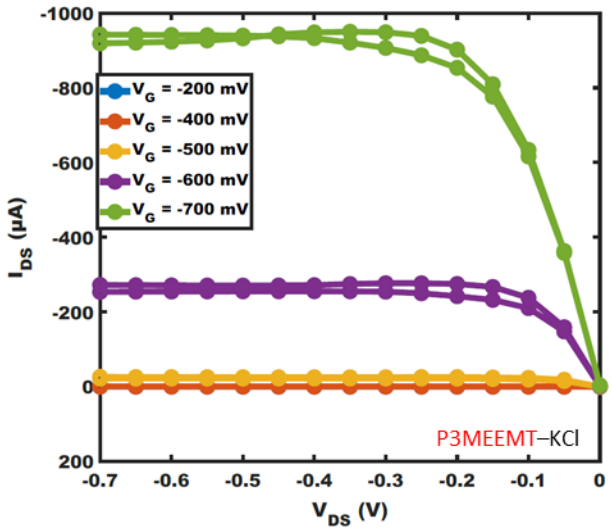

Figure A5. OECT output curve of poly(3-{[2-(2-methoxyethoxy)ethoxy]methyl}thiophene-2,5-diyl) (P3MEEMT) in 100 mmol/L $KCl_{(aq)}$ obtained from Flagg et al.[24]

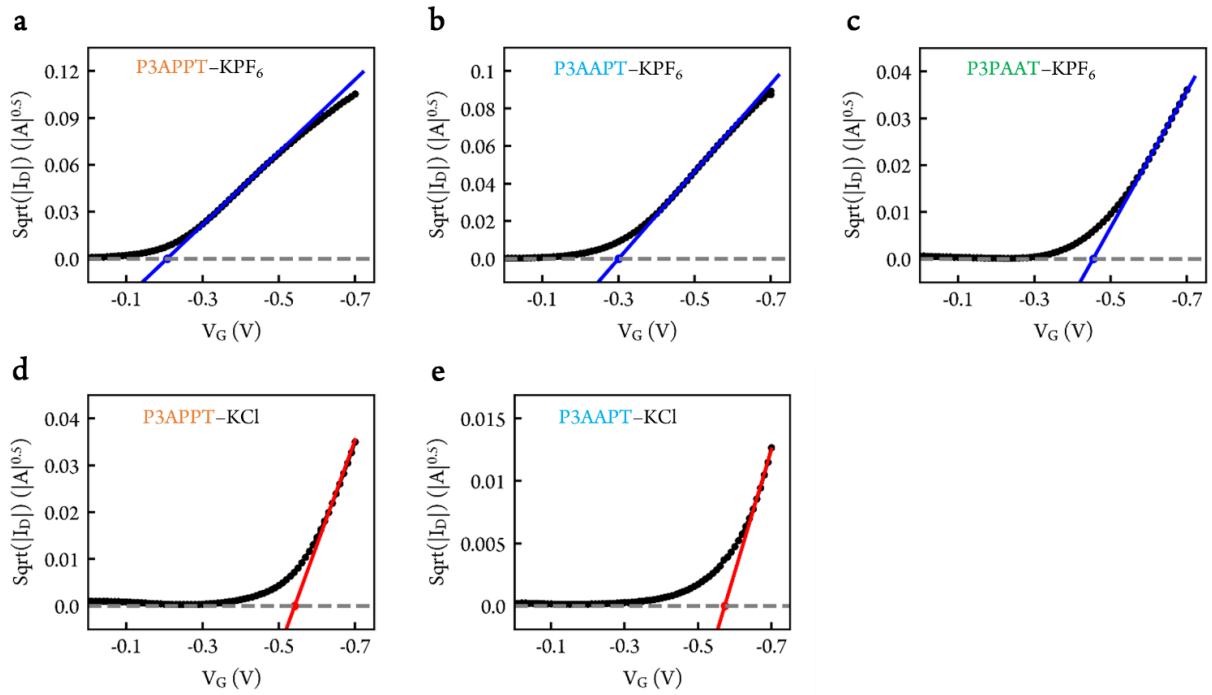

Figure A6. Determination of threshold voltage (V_T) of reduced-oxygen-content side chain polymers in 100 mmol/L $KPF_{6(aq)}$ (a) P3APPT (b) P3AAPT (C) P3PAAT and in 100 mmol/L $KCl_{(aq)}$ (d) P3APPT (e) P3AAPT. Channel width/length = 4000 µm/10 µm. Grey dash lines are a guide for the eye.

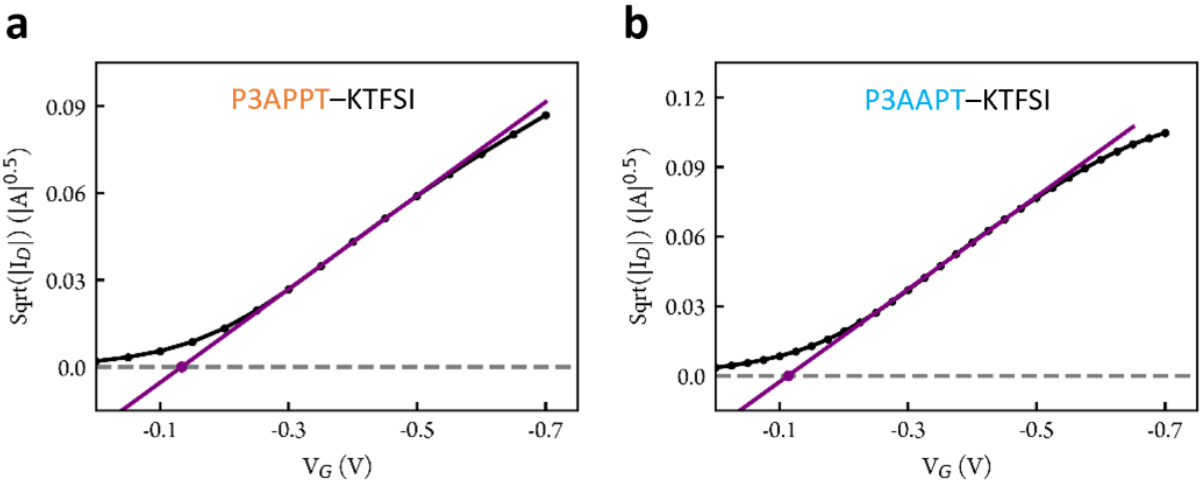

Figure A7. Determination of V_T of reduced-oxygen-content side chain polymers in 100 mmol/L $KTFSI_{(aq)}$ (a) P3APPT (b) P3AAPT. Channel width/length = 2000 µm/10 µm. Grey dash lines are a guide for the eye.

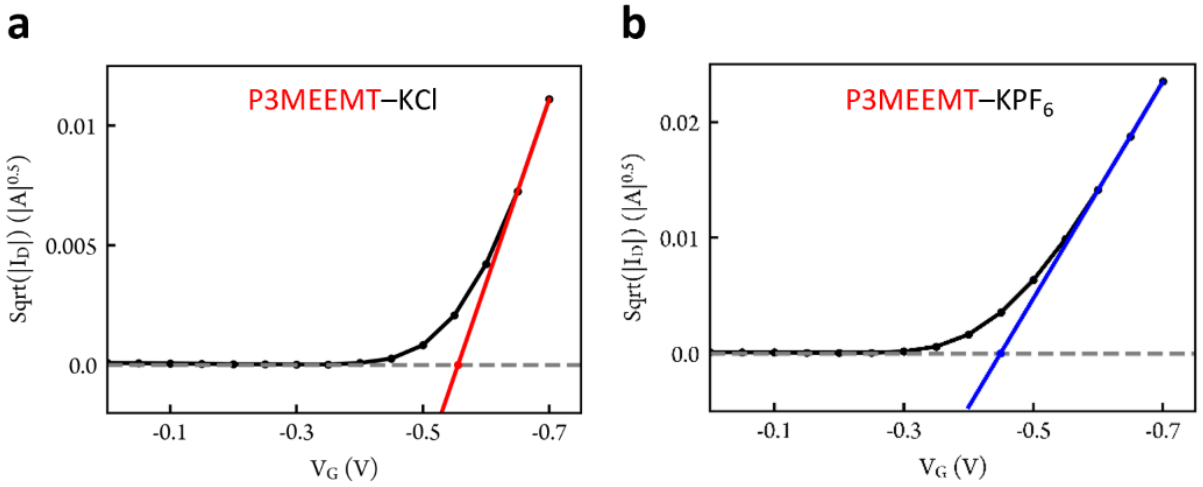

Figure A8. Determination of V_T of P3MEEMT in (a) 100 mmol/L $KCl_{(aq)}$ and (b) 100 mmol/L KPF_6 obtained from Flagg et al.[24] Grey dash lines are guide for the eye.

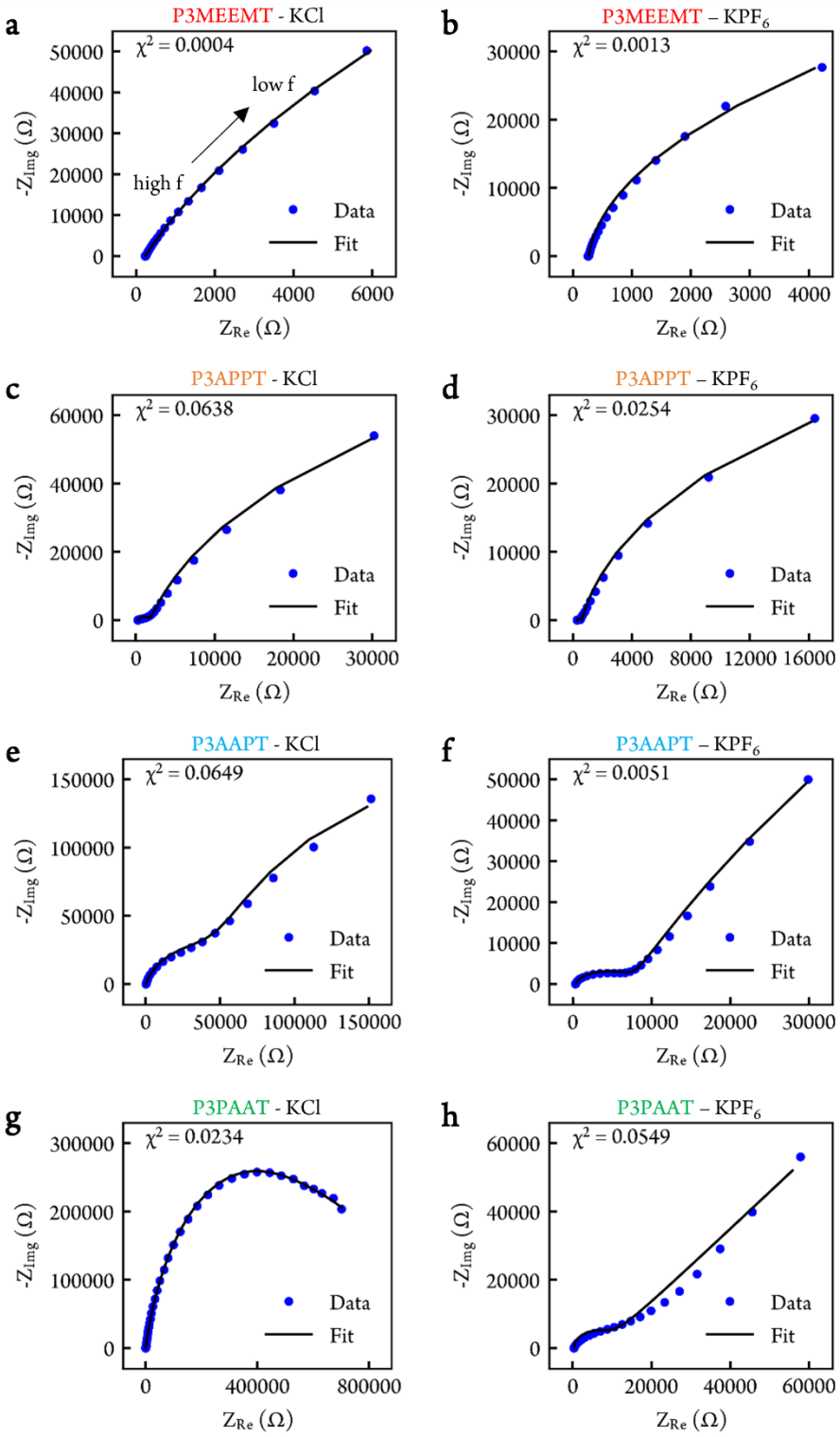

Figure A9. Example Nyquist plots of (a)(b)P3MEEMT (c)(d) P3APPT (e)(f) P3AAPT (g)(h) P3PAAT in 100 mmol/L $KCl_{(aq)}$ (left) and 100 mmol/L $KPF_{6(aq)}$ (right), respectively.

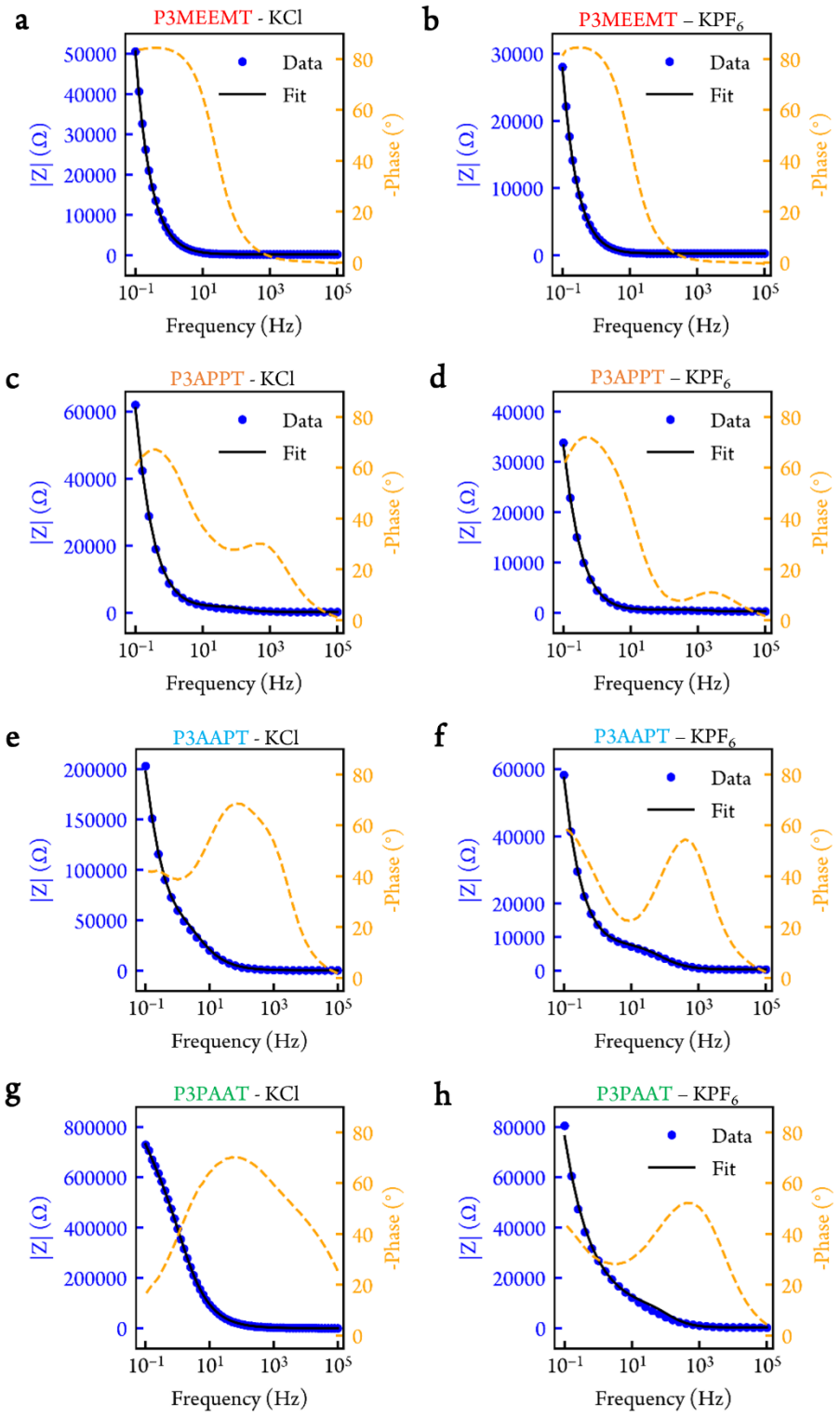

Figure A10. Example Bode plots of (a)(b)P3MEEMT (c)(d) P3APPT (e)(f) P3AAPT (g)(h) P3PAAT in 100 mmol/L $KCl_{(aq)}$ (left) and 100 mmol/L $KPF_{6(aq)}$ (right), respectively.

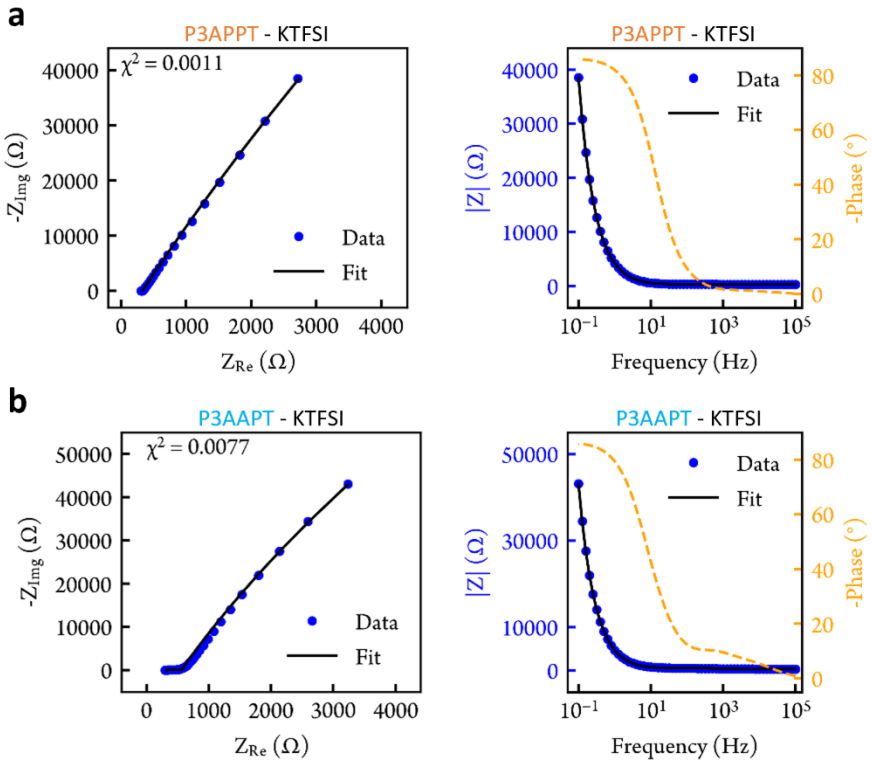

Figure A11. Example Nyquist plot (left) and Bode plot (right) of (a)P3APPT (b) P3AAPT in 100 mmol/L $KTFSI_{(aq)}$.

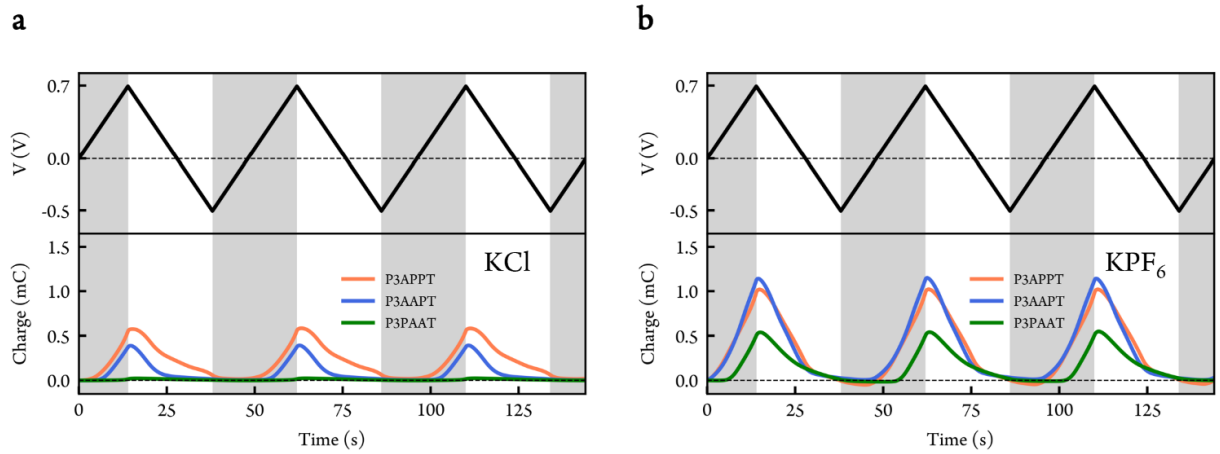

Figure A12. Charge injection in polymer films during cyclic voltammetry (CV) scans in (a) 100 mmol/L $KCl_{(aq)}$ and (b) 100 mmol/L $KPF_{6(aq)}$. Black dash lines are a guide for the eye.

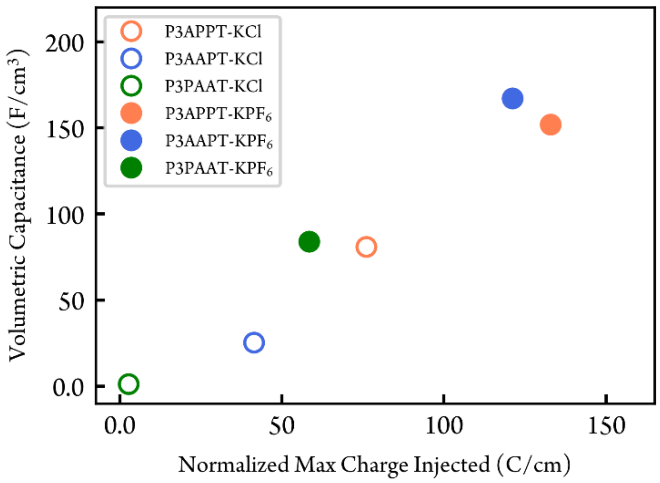

Figure A13. Volumetric capacitance (via EIS) and charge injected in polymer films (via coulometry). Charge injected in the film was normalized by polymer film thickness.

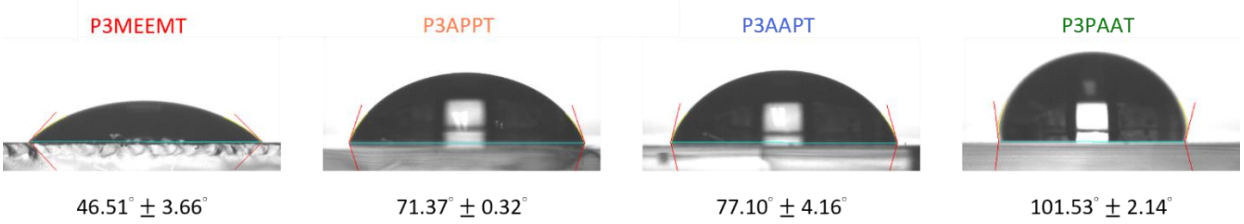

Figure A14. Water contact angle measurement images. Error bars represent standard error of the mean.

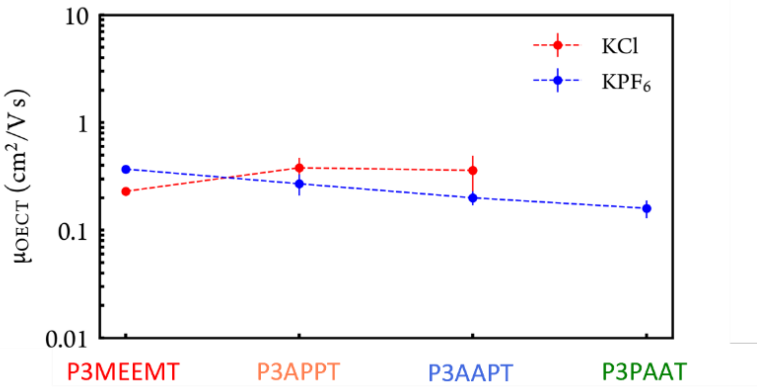

Figure A15. OECT mobility of polymers in 100 mmol/L $KCl_{(aq)}$ and 100 mmol/L $KPF_{6(aq)}$. Dash lines are guide for the eye. OECT mobility was derived from dividing μC^* by C^* with error propagation. Error bar represents standard error of mean.

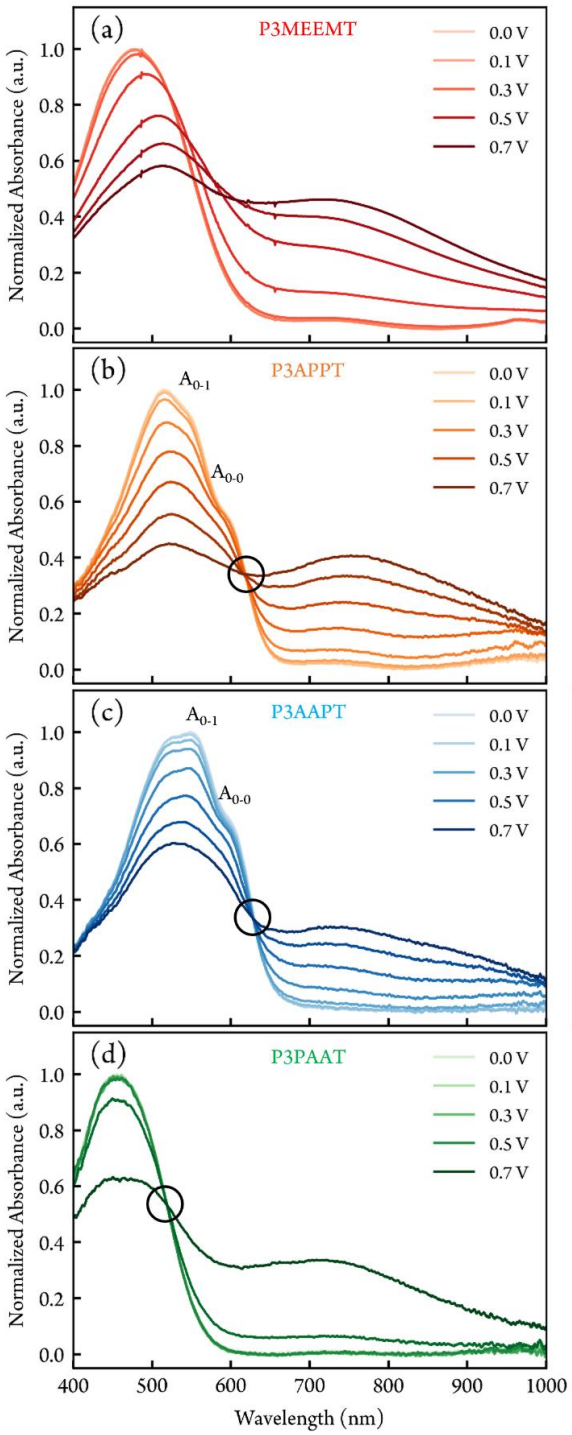

Figure A16. Spectroelectrochemistry of (a) P3MEEMT (b) P3APPT (c) P3AAPT (d) P3PAAT in 100 mmol/L $KCl_{(aq)}$ electrolyte upon doping. Doping potential = 0.0 V, 0.1 V, 0.2 V, 0.3 V, 0.4 V, 0.5 V, 0.6 V, 0.7 V (vs Ag/AgCl). Black circle indicates the isosbestic point. Only P3APPT and P3AAPT show vibronic progression feature.

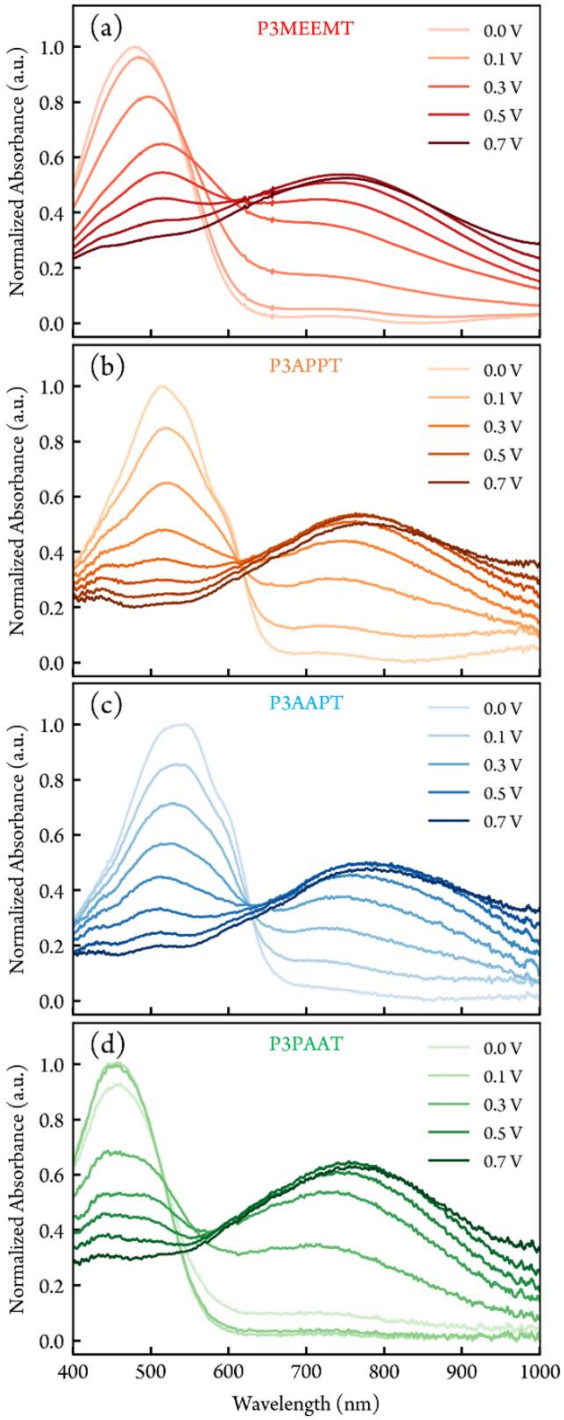

Figure A17. Spectroelectrochemistry of (a) P3MEEMT (b) P3APPT (c) P3AAPT (d) P3PAAT in 100 mmol/L $KPF_{6(aq)}$ electrolyte upon doping. Doping potential = 0.0 V, 0.1 V, 0.2 V, 0.3 V, 0.4 V, 0.5 V, 0.6 V, 0.7 V (vs Ag/AgCl).

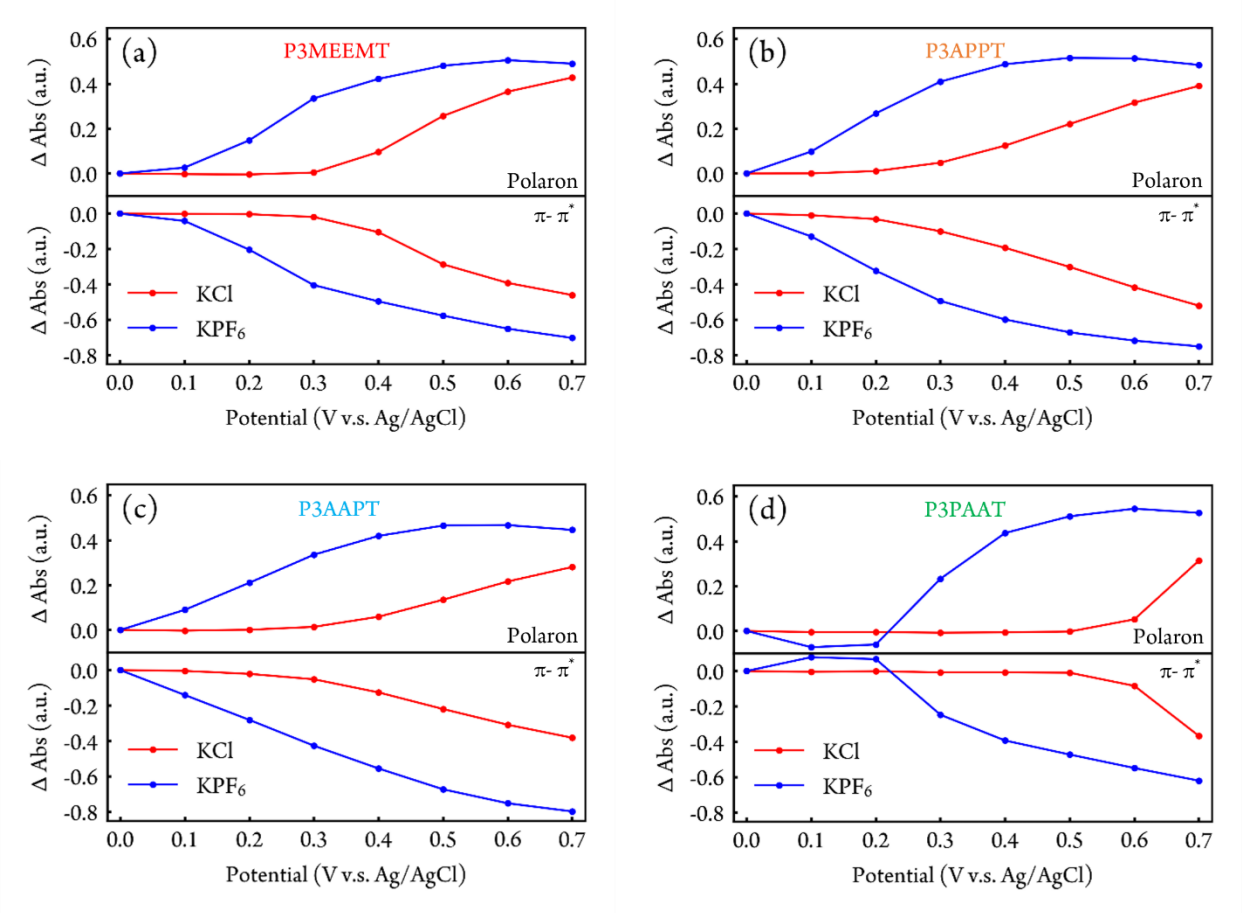

Figure A18. Comparison of polaron and π-π^* peak absorbance change upon doping in 100 mmol/L $KCl_{(aq)}$ and $KPF_{6(aq)}$ (a) P3MEEMT (b) P3APPT (c) P3AAPT and (d) P3PAAT.

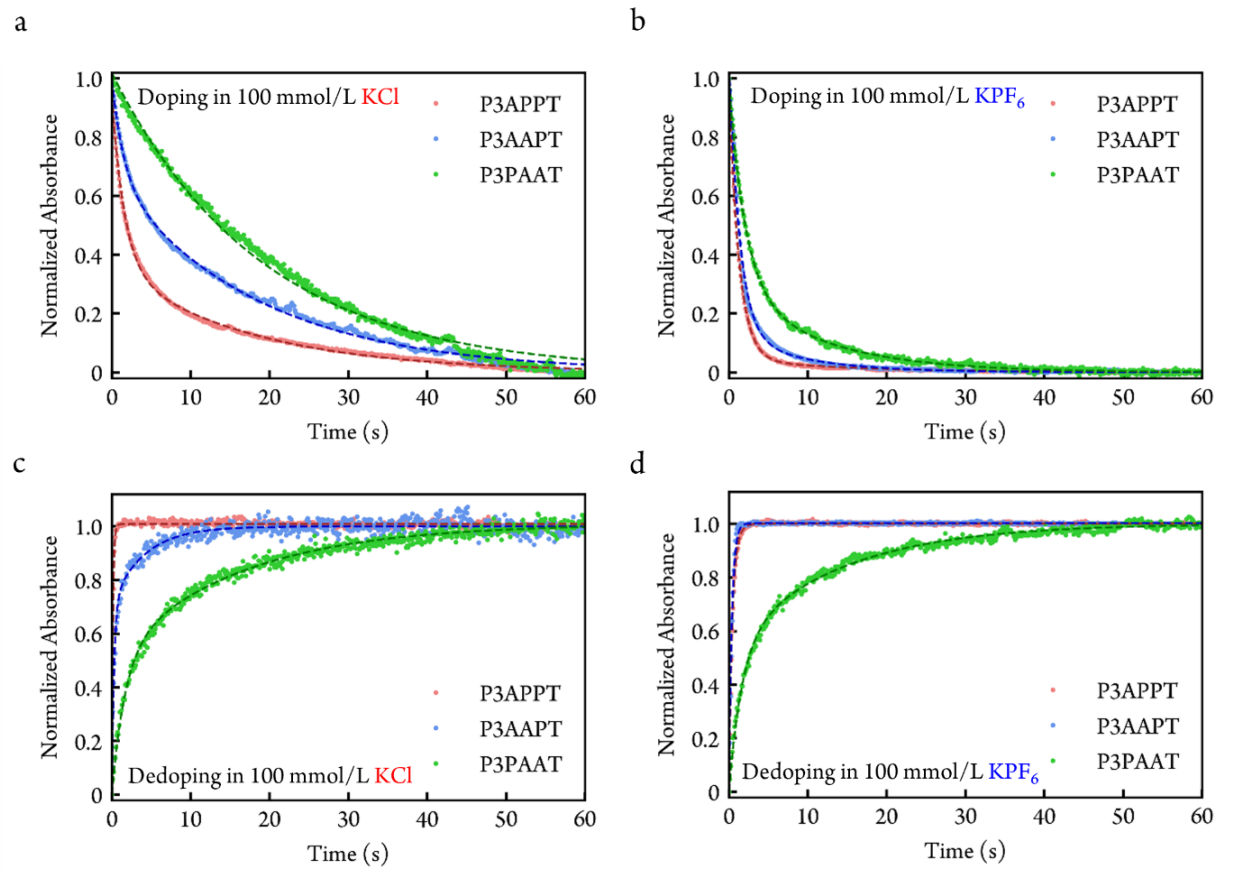

Figure A19. π-π^* peak absorbance change over time during doping in (a) $KCl_{(aq)}$ (b) $KPF_{6(aq)}$ and dedoping in (c) $KCl_{(aq)}$ (d) $KPF_{6(aq)}$. Dash lines represent the fitting results.

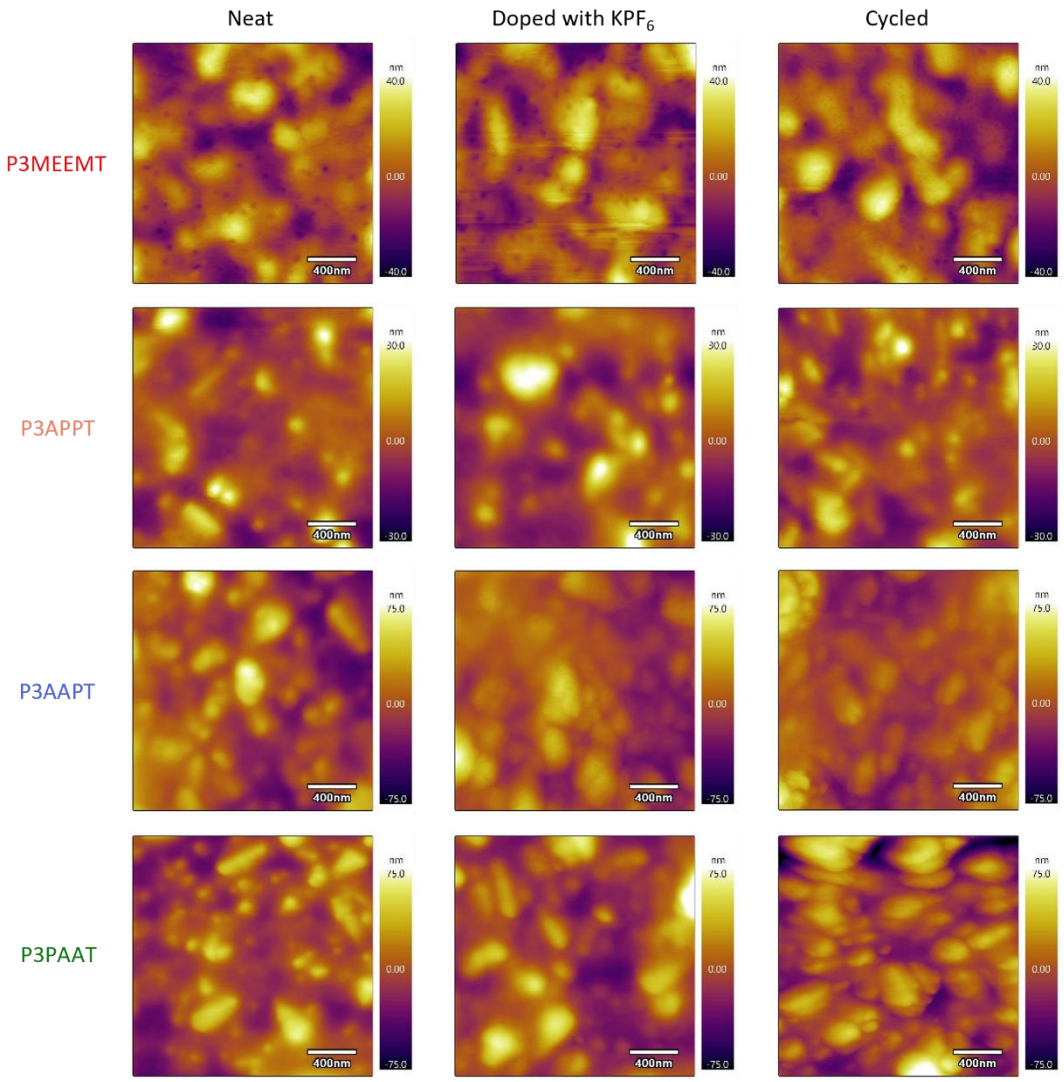

Figure A20. Atomic force microscopy (AFM) topography images of four polymers in three different states: neat, doped and after three cycles of doping and dedoping. Polymer films were deposited on fluorine-doped tin oxide (FTO) glass substrate.

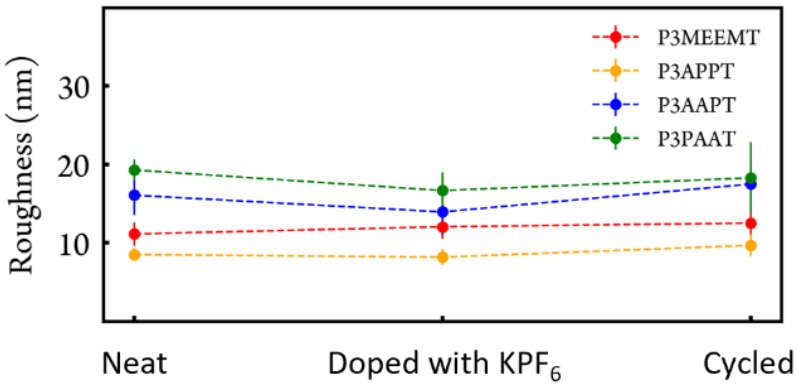

Figure A21. Roughness of neat polymer films, doped polymer films (with KPF_6), and polymer films doped and dedoped for three cycles with KPF_6. At least four different regions of the film were scanned. Error bars represent standard deviation.

Table A1. V_T and C^* Results of P3APPT and P3AAPT in 100 mmol/L $KTFSI_{(aq)}$

	C^*	V_T
	(F/cm^3)	(V)
P3APPT	143.2 ± 9.4	-0.14 ± 0.01
P3AAPT	107.5 ± 6.5	-0.11 ± 0.02

Table A2. Polythiophene Derivatives with Isosbestic Point Observed in Spectroelectrochemistry

Polymer	Electrolyte	References
P3HHT	KCl	[68]
P3MEET	NaCl	[58]
PTHS-TMA+-co-P3HT 70:30 mol	NaCl	[31]
PTHS-TMA+-co-P3HT 51:49 mol	NaCl	[31]
PTHS-TMA+-co-P3HT 23:77 mol	NaCl	[31]
P3HT	Polymetric Ionic Liquid	[64]
P3APPT	KCl	This work
P3AAPT	KCl	This work
P3PAAT	KCl	This work

Conversion of CPE to Capacitor.

Eq A1 shows the impedance form of a constant phase element (CPE). ω is the angular frequency. Y_0 and n are the characteristic parameters of the CPE. A CPE is an imperfect capacitor with n value between 0 and 1. A CPE with n equals to 1 represents an ideal capacitor. Eq A2 shows the impedance form of a capacitor. We applied Eq A3 to convert Y_0 to an equivalent capacitor. ω''_{max} is the frequency where the imaginary part of impedance has its maximum.[122,123]

$$Z_{CPE} = \frac{1}{Y_0 (i\omega)^n} \quad \text{(Eq A1)}$$

$$Z_C = \frac{1}{C (i\omega)^1} \quad \text{(Eq A2)}$$

$$C = Y_0 (\omega''_{max})^{n-1} \quad \text{(Eq A3)}$$

APPENDIX B: SUPPORTING INFORMATION FOR CHAPTER 3

This work has been submitted to Nature Materials and is also available on arXiv: arXiv:2305.01179.

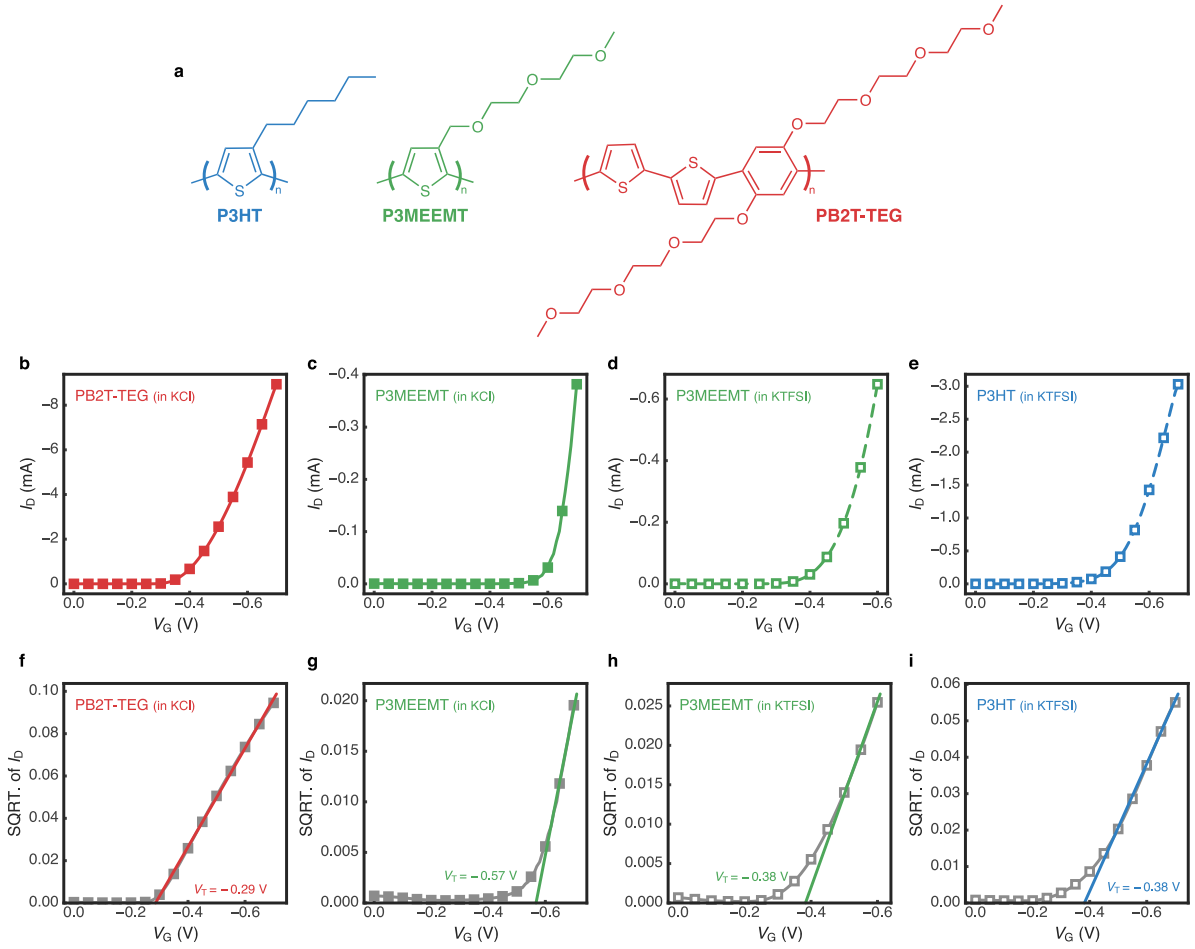

Figure B1. Transfer curves and threshold voltage determination. (a) The polymer structure of P3HT, P3MEEMT, and PB2T-TEG (b-e) transfer curves and (e-i) threshold voltage fits of polymers in 0.1 M KCl and 0.1 M KTFSI.

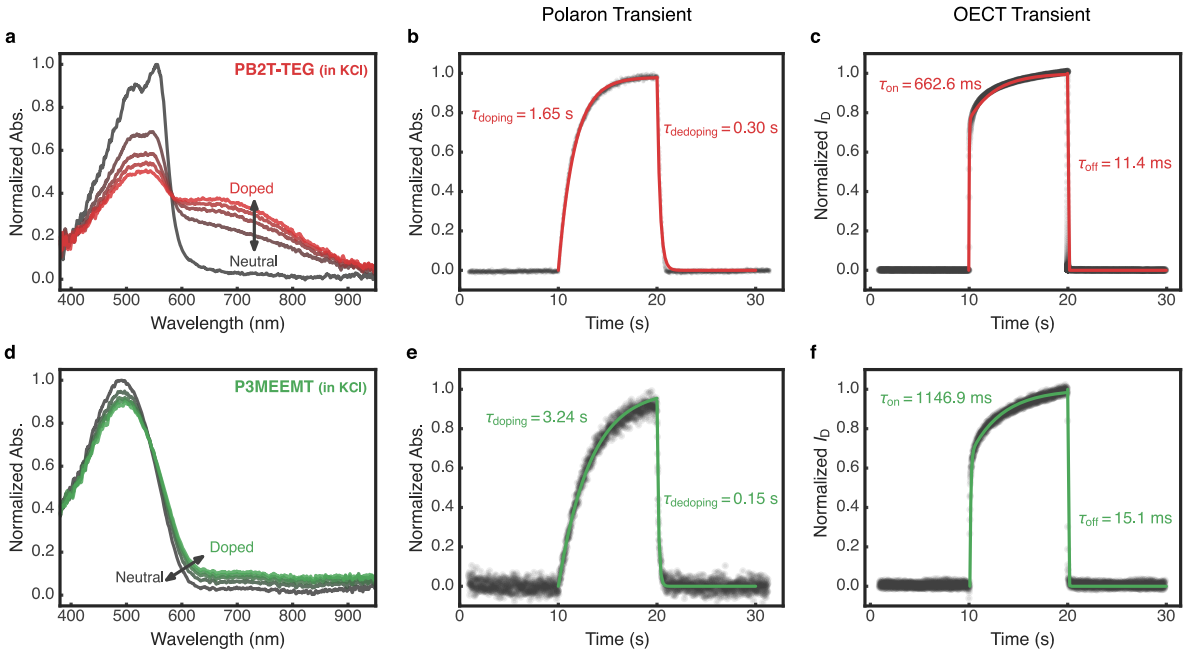

Figure B2. The comparison between spectroelectrochemistry and OECT transient behaviors in 0.1 M KCl. The UV-Vis spectra of (a) PB2T-TEG and (d) P3MEEMT in 0.1 M KCl. The Polaron transient of (b) PB2T-TEG and (e) P3MEEMT in 0.1 M KCl. The OECT transient of (c) PB2T-TEG and (f) P3MEEMT in 0.1 M KCl. Dots represent the data and lines represent the fit in (b), (c), (e), and (f).

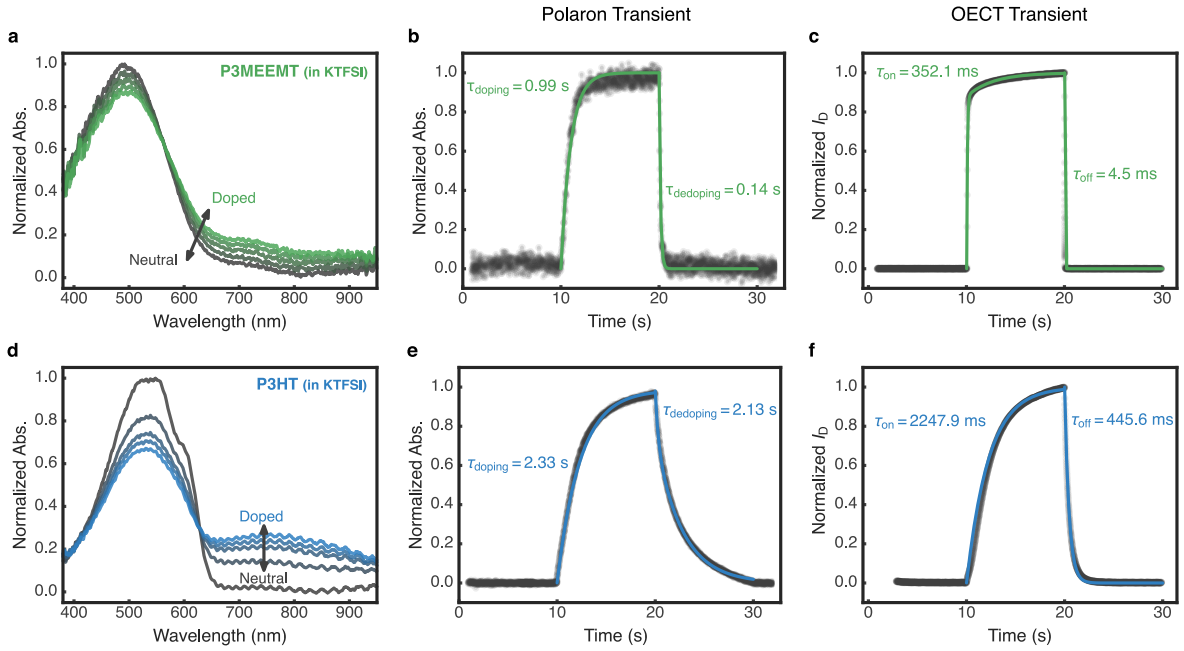

Figure B3. The comparison between spectroelectrochemistry and OECT transient behaviors in 0.1 M KTFSI. The UV-Vis spectra of (a) PB2T-TEG and (d) P3MEEMT in 0.1 M KTFSI. The polaron transient of (b) PB2T-TEG and (e) P3MEEMT in 0.1 M KTFSI. The OECT transient of (c) PB2T-TEG and (f) P3MEEMT in 0.1 M KTFSI. Dots represent the data and lines represent the fit in (b), (c), (e), and (f).

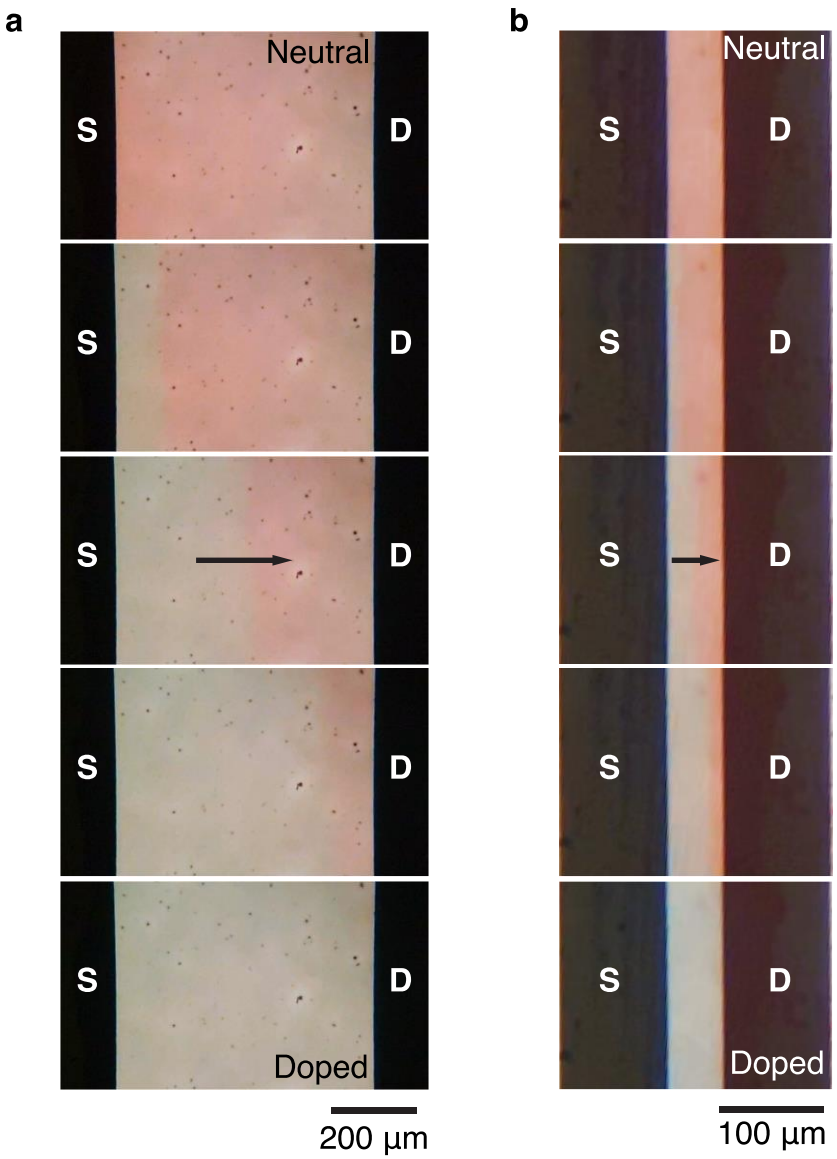

Figure B4. Microscope screenshots of P3MEEMT OECT channels during operation. Turn-on process of P3MEEMT-based OECT with the channel length of (a) 600 µm (b) 50 µm. The electrolyte is 0.1 M KCl. Arrows indicate the doping front propagation direction. The color of the P3MEEMT polymer is red/orange in the neutral state and blue in the doped state.

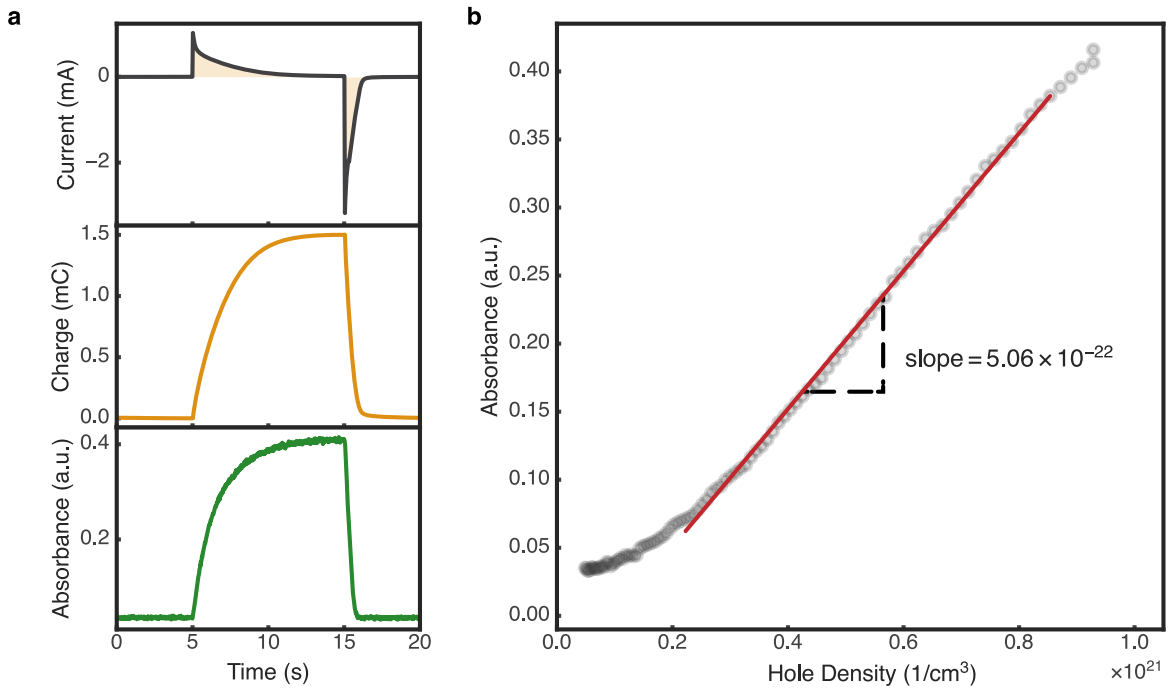

Figure B5. The absorption-hole density calibration based on Beer's law. (a) The transient response of current, charge, and absorbance of PB2T-TEG in spectroelectrochemistry. The electrolyte is 0.1 M KCl. (b) The relation between absorbance and hole density.

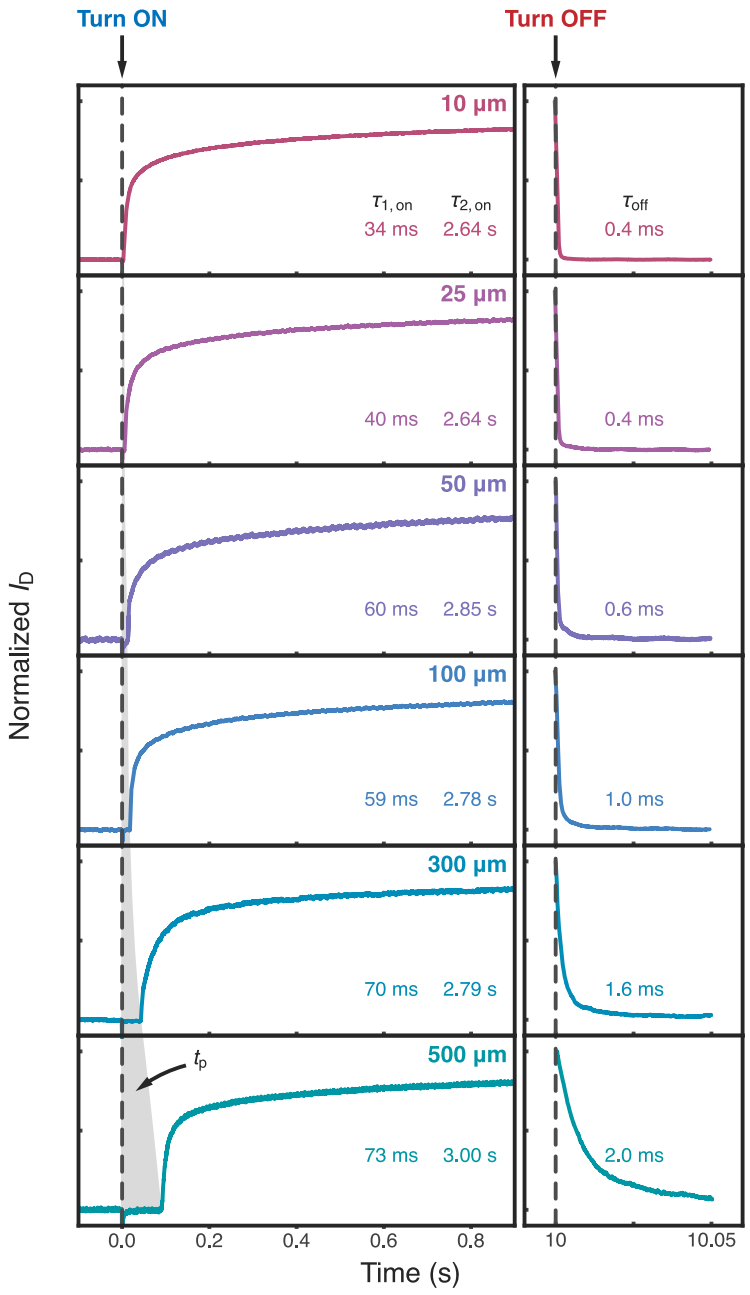

Figure B6. The transient response with various channel lengths. The polymer is PB2T-TEG, and the electrolyte is 0.1 M KCl. The transistor channel width is 5 mm and the film thickness is ≈ 50 nm. The gate potential is fixed at $|V_G - V_T| = 0.2$ V, and the drain potential is – 0.6 V.

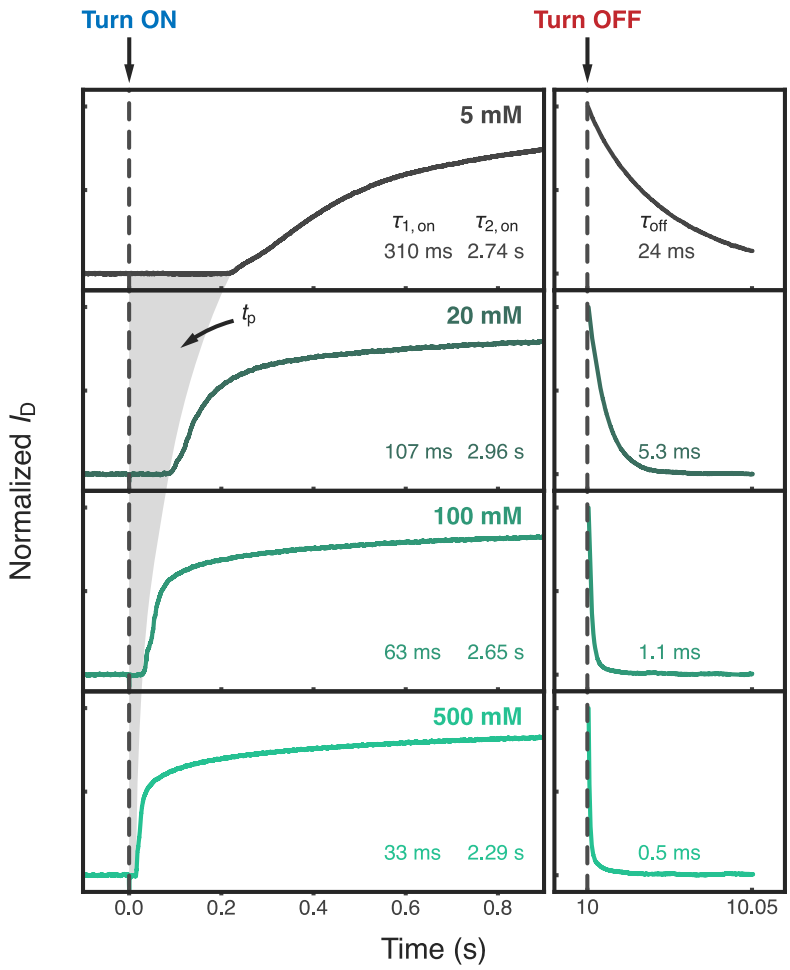

Figure B7. The transient response with various ion concentrations. The polymer is PB2T-TEG. The transistor channel width is 2.5 mm, the channel length is 100 μm and the film thickness is ≈ 50 nm. The gate potential is fixed at $|V_G - V_T| = 0.2$ V, and the drain potential is – 0.6 V.

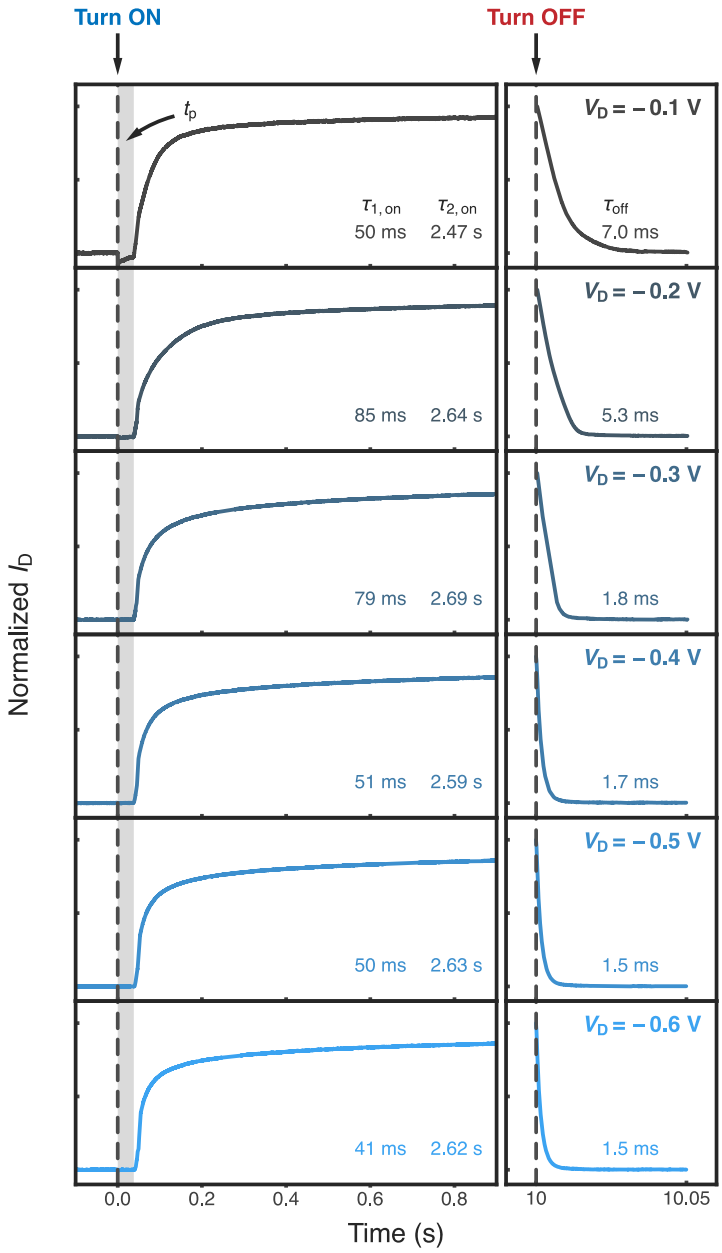

Figure B8. The transient response with various drain potentials. The polymer is PB2T-TEG, and the electrolyte is 0.1 M KCl. The transistor channel width is 5 mm, the channel length is 100 μm, and the film thickness is ≈ 50 nm. The gate potential is fixed at $|V_G - V_T| = 0.2$ V.

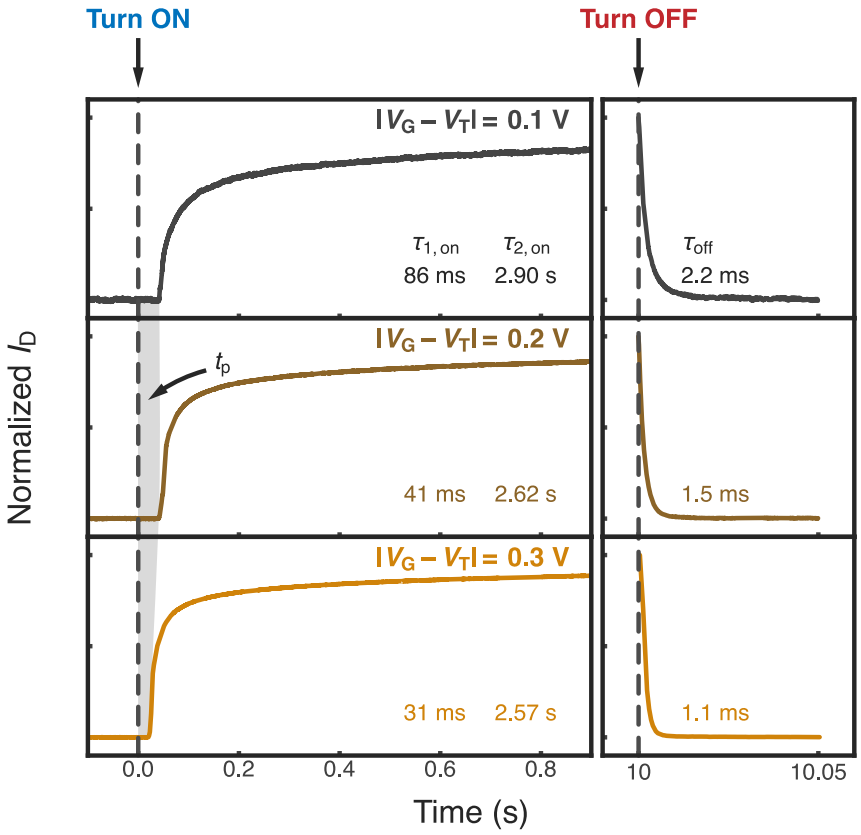

Figure B9. The transient response with various gate potentials. The polymer is PB2T-TEG, and the electrolyte is 0.1 M KCl. The transistor channel width is 5 mm, the channel length is 100 μm, and the film thickness is ≈ 50 nm. The drain potential is – 0.6 V.

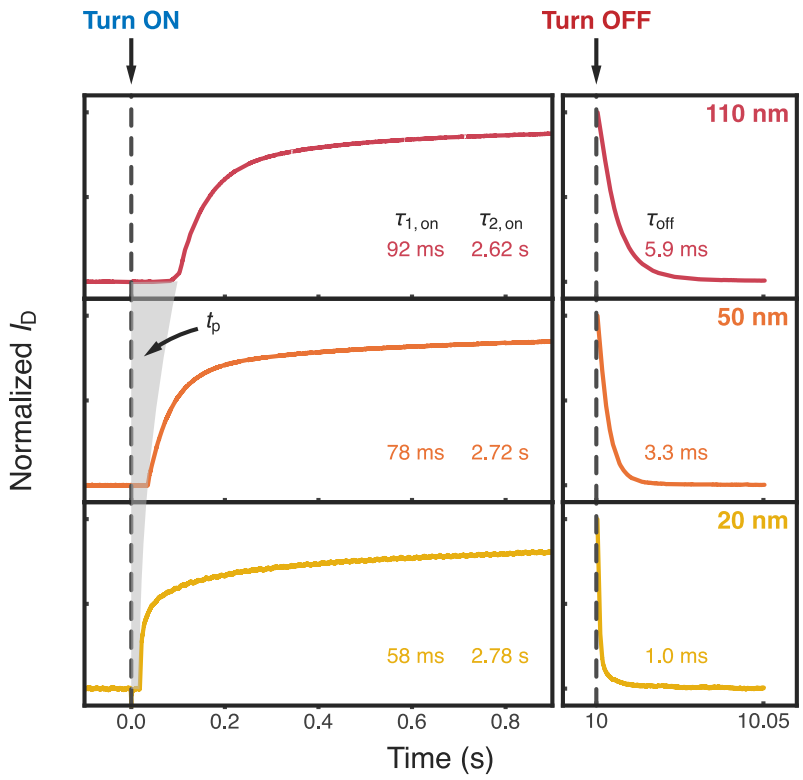

Figure B10. The transient response with various film thickness. The polymer is PB2T-TEG, and the electrolyte is 0.1 M KCl. The transistor channel width is 5 mm, and the channel length is 100 μm. The gate potential is fixed at $|V_G - V_T| = 0.2$ V, and the drain potential is – 0.6 V.

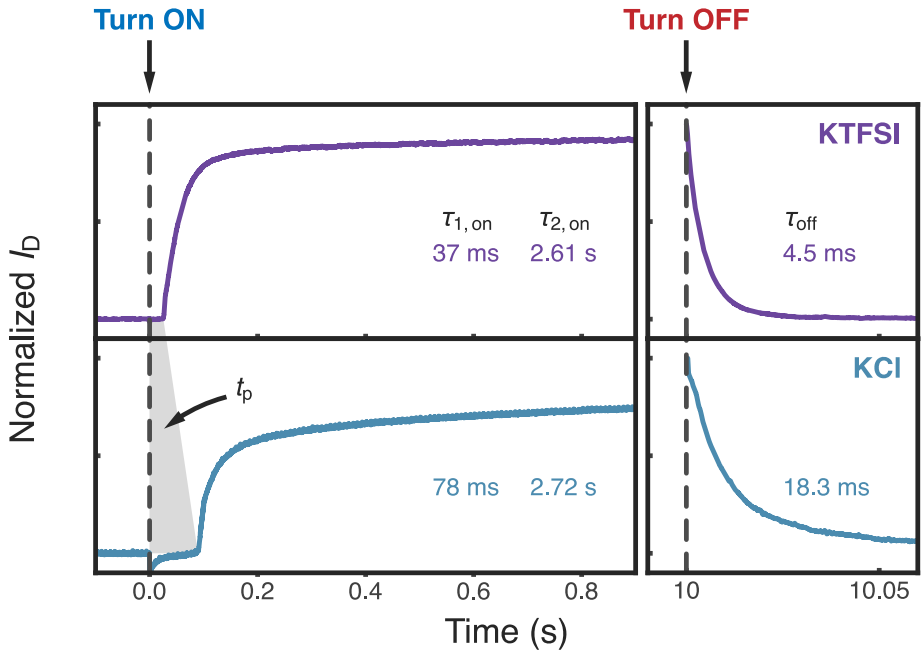

Figure B11. The transient response with various counter anion species. The polymer is P3MEEMT. The transistor channel width is 5 mm, the channel length is 100 μm, and the film thickness is ≈ 120 nm. The gate potential is fixed at $|V_G - V_T| = 0.2$ V, and the drain potential is – 0.6 V.

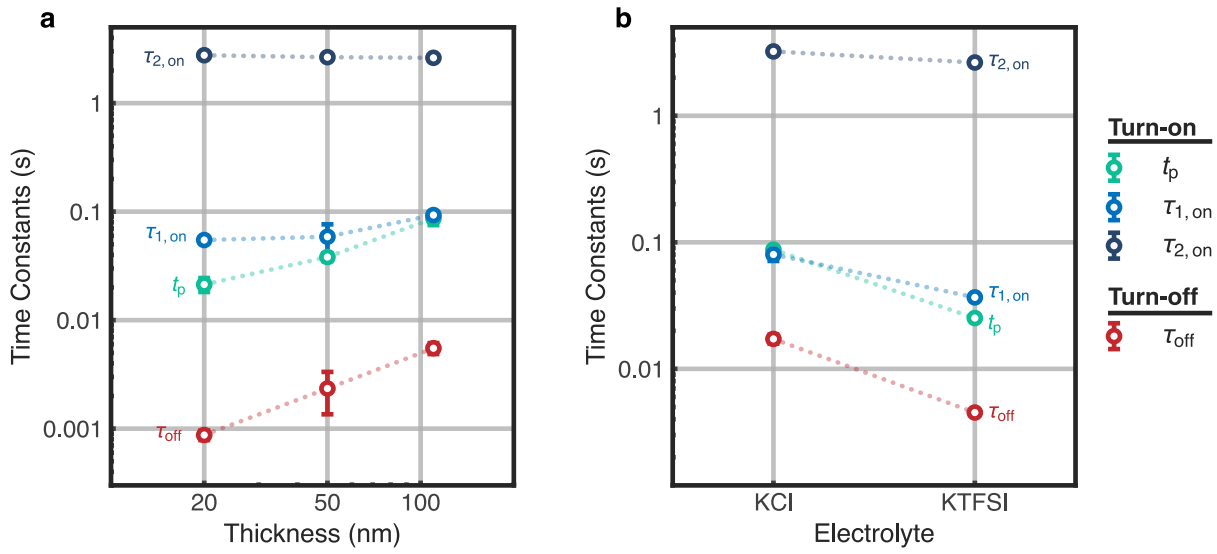

Figure B12. The relation between response time constants and (a) thickness (results from Fig. B10) and (b) counter anions (results from Fig. B11). Error bars represent the standard deviation from multiple cycles.

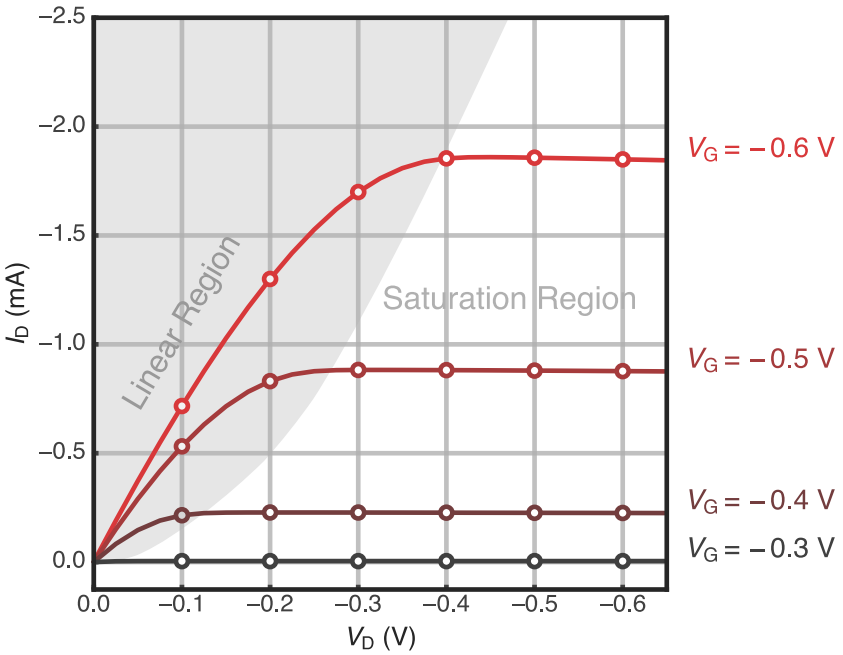

Figure B13. The output curve of PB2T-TEG in 0.1 M KCl.

Table B1. OCP and V_T Values of Different Polymer/Electrolyte Pairs

Polymer	Electrolyte	OCP (V)[a]	V_T (V)[b]
PB2T-TEG	0.1 M KCl	0.11	-0.29
P3MEEMT	0.1 M KCl	0.13	-0.57
P3MEEMT	0.1 M KTFSI	-0.03	-0.38
P3HT	0.1 M KTFSI	-0.12	-0.38

a. Open circuit potential of the system.

b. OECT threshold voltage. See Figure B1.

Table B2. Response Time Constants of Spectroelectrochemistry and OECT

Polymer	Electrolyte	SpecEChem τ_{doping} (s) [a]	OECT τ_{on} (s) [b]	SpecEChem $\tau_{dedoping}$ (s) [c]	OECT τ_{off} (s) [d]
PB2T-TEG	0.1 M KCl	1.69 ± 0.01	0.65828 ± 0.00701	0.29 ± 0.01	0.00124 ± 0.00002
P3MEEMT	0.1 M KCl	3.17 ± 0.07	1.14873 ± 0.03257	0.16 ± 0.01	0.01693 ± 0.00075
P3MEEMT	0.1 M KTFSI	1.05 ± 0.03	0.34316 ± 0.00515	0.15 ± 0.01	0.00447 ± 0.00004
P3HT	0.1 M KTFSI	2.67 ± 0.35	2.25052 ± 0.01539	2.18 ± 0.05	0.44508 ± 0.00134

a. Average tau from biexponential fit or single exponential fit. Error bars represent standard error of the mean from multiple cycles. Time resolution of spectroelectrochemistry is ≈ 10 ms.

b. Average tau from biexponential fit. We did not consider propagation time (t_p) here. Error bars represent standard error of the mean from multiple cycles. Time resolution of OECT is ≈ 10 μs.

c. Average tau from biexponential fit or single exponential fit. Error bars represent standard error of the mean from multiple cycles.

d. Tau from single exponential fit. Error bars represent standard error of the mean from multiple cycles.

Note B1. Transient fits with Bernards model

The Bernards model considers the transient behavior of an OECT as the characteristic of charging or discharging a capacitor.[37] Assuming charging or discharging occurs uniformly along the channel polymer, they proposed that I_D to have a single exponential response when switching between two steady-states:

$$I_D(t, V_G) = I_{ss}(V_G) + \Delta I_{ss}\left(1 - f\frac{\tau_e}{\tau_i}\right) \cdot e^{-t/\tau_i}$$

where I_{SS} is the steady-state channel current, and ΔI_{SS} is the current difference between two different steady-states. f determines the ratio of I_{GS} and I_{GD}. τ_e is the electronic charge transit time and τ_i is the product of $R_S \cdot C_{Ch}$. The R_S is the electrolyte resistance and the C_{Ch} is the channel capacitance.[37] They demonstrated the I_D response to be either a monotonic decay or a spike-and-recovery depending on the ratio between $f\tau_e$ and τ_i, with device switching speed determined by τ_i.[37]

As shown in Figure 3-1a, we found that Bernards model cannot accurately describe the transient response of accumulation mode OECTs. Most importantly, the Bernards model cannot explain the much faster device turn-off speed compared to turn-on phenomenon, which, based on the model, should be both equal to τ_i, as R_S and C_{Ch} are the same. We believe the reasons why Bernards model failed to predict the switching behavior of accumulation mode OECTs are as follows: first, the uniform charging or discharging assumption is inaccurate. Second, the carrier density dependent mobility needs to be considered, especially during device turn-off. Last, Bernards and Malliaras developed the model based on poly(3,4-ethylenedioxythiophene) doped with poly(styrene sulfonate) (PEDOT:PSS), which is a depletion mode OECT material.

Note B2. Off-interval dependent OECT turn-on kinetics

Figure B14 shows faster OECT turn-on kinetics through shortening the off-interval. To ensure the same electrochemical doping level is achieved, we fixed the on-interval to be 30 s for each cycle while varying the off-interval from 30 s to 1 s. Since the τ_{off} is much smaller than τ_{on} (see main text), the device could be turned off even with 1s off-interval in this case. It is clear that transistor turns on faster (smaller τ_{on}) with shorter off-interval. This phenomenon occurs because even though the transistor is at off-state already, dedoping of the channel polymer is not fully completed (see main text).

This behavior also implies that accumulation mode OECT turn-on kinetics is duty cycle dependent if the total period is carefully selected. Duty cycle is defined as the ratio between on-interval over the total period, and the total period is the sum of the on-interval and the off-interval. The duty-dependent kinetics may be beneficial for emulating neuron dynamic filtering function, in which the post synaptic response (i.e. I_D) depends on the duty of the presynaptic stimuli (i.e. V_G). Previously, Gkoupidenis et al.[104] and Yamamoto et al.[43] had demonstrated the dynamic filtering function with depletion mode, PEDOT:PSS-based OECTs.

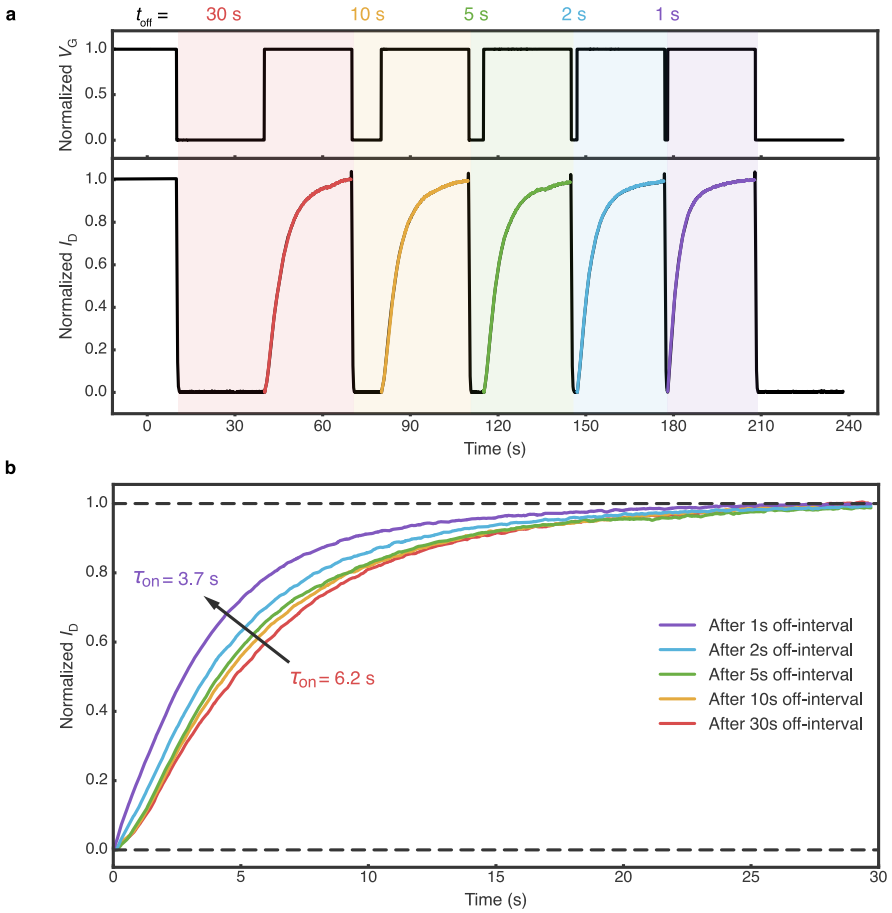

Figure B14. (a) The transient response of a P3HT-based OECT with a fixed on-interval (30 s) and various off-intervals. Pre indicates previous runs for device stabilization. Numbers represent the cycle number. Transistor channel width, length and thickness is 4000 μm, 10 μm and ≈ 100 nm, respectively. (b) Comparison between turn-on kinetics with various off-intervals.

Note B3. Carrier density-dependent mobility

Previously, with the exponentially distributed density of states (DOS) assumption, Friedlein et al. proposed the relation between OECT mobility and carrier concentration to be:

$$\mu = \mu_0 \cdot \left(\frac{p}{p_0}\right)^{\frac{E_0}{k_B T}-1} \quad (1)$$

where μ_0 is mobility prefactor and p_0 is zero-filed hole concentration. E_0 describes the energetic width of the tail of the density of states, k_B is Boltzmann's constant and T is temperature.[105] We found that our mobility and carrier concentration relation could be well characterized with this equation (Figure 3-4b and Figure B15a). The E_0 obtained from mobility and carrier concentration fit is ≈ 300 meV.

To justify our fitting result, we further estimated the E_0 value from the ultraviolet photoelectron spectroscopy (UPS) spectra data from our previous work.[110] Figure B15b shows the estimation of E_0 value of PB2T-TEG via the exponential fit of the edge of HOMO region. We found the E_0 value is ≈ 204 meV, which we believe is close to the value obtained from mobility and carrier concentration fit, considering the difficulty to accurately determine the width of DOS via different techniques,[124,125] and the possible broadening of DOS after doping.[126] The similar E_0 values obtained by two different methods verify that our approach studying mobility and carrier density relation is feasible.

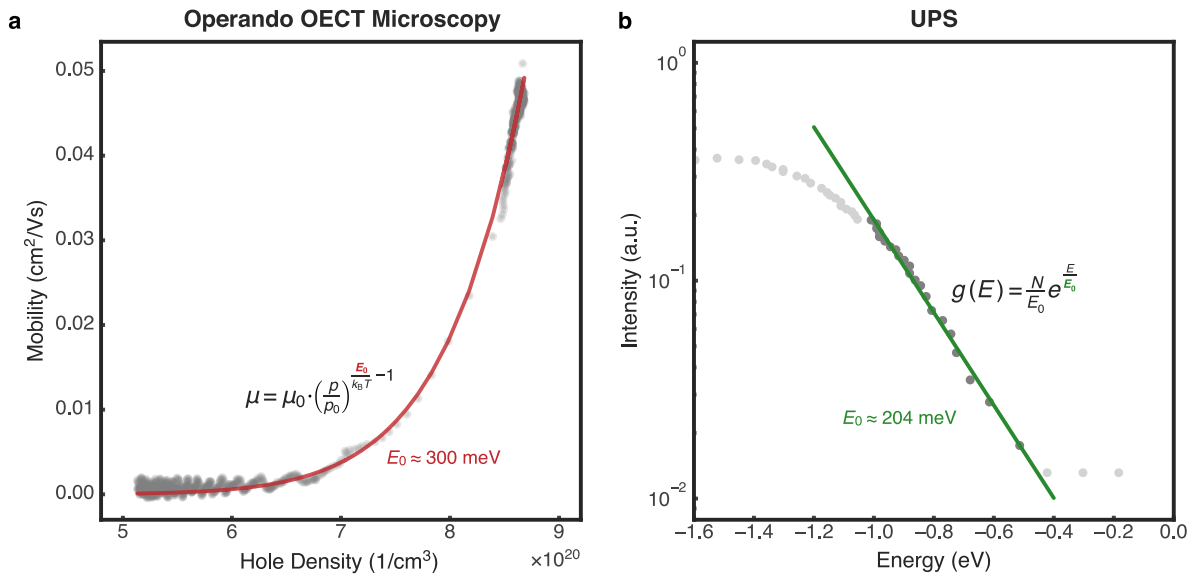

Figure B15. The estimation of the energetic width of the tail of the density of states (E_0) with (a) OECT mobility and concentration fit and (b) via ultraviolet photoelectron spectroscopy (UPS). N represents number of states, E is the energy, and g is the DOS in the equation in (b).

Note B4. SPICE simulation

Here, we attempt to replicate the delayed turn-on (doping front propagation stage) and asymmetric kinetics via circuit modeling. To the best of our knowledge, Ersman et al. are the only ones to report an OECT circuit model including active elements and show asymmetric kinetics with depletion mode OECTs.[17] In their approach, a diode was used to represent the discharging path from the body of a SPICE MOSFET model. Though their model can indeed represent asymmetric kinetics, it does not intuitively capture the physics of an OECT, because unlike a MOSFET, there is no body terminal in an OECT. On the other hand, purely passive element circuit models are very popular, as in those developed by Bernards et al. and Faria et al. that have seen widespread adoption.[37,84] However, such circuit models are linear and thus cannot exhibit different turn-on and turn-off kinetics. For details, the reader is referred to reviews on circuit model kinetics,[108,127,128] and a more systematic modeling is beyond the scope of this manuscript.

To reconcile these two approaches with our experimental data, based on the classical R_s+($R_{ct}||C_p$) model commonly used in literature,[84,129] we include a time-dependent resistance to represent the channel polymer resistivity. The RC component could reflect the initial "spike" in both I_G and I_D, while the time-dependent resistance could replicate the timing. Figure B16a shows the proposed equivalent circuit model. Here, V_G is the gate potential and V_D is the drain potential. R_s is the solution resistance, R_D(t) is the time-dependent resistance and R_{ss} is the source electrode contact used for measuring current in SPICE simulation. C_p and R_{ct} are the polymer volume capacitance and charge transfer resistance commonly applied in Randles circuit. R_s, C_p, R_{ct} have limited effects on the kinetics through the channel in this proposed model, where they represent the electrolyte-drain interface, rather than the entire active layer. We also included a constant

current source to represent the gate leakage current, $f \times I_G$, which does not affect the kinetics here. The detailed explanation of *f* factor could be found in Faria and Bernards models.[37,84]

Figure B16b shows the transient response and SPICE simulation result of an example accumulation mode P3HT OECT operating 0.1 M KTFSI. (*W*/*L*/*d* = 5 mm/100 μm/100 nm) The drain potential is fixed at −0.6 V while the on-potential is −0.2 V and off-potential is −0.6 V. We modeled the time-dependent resistance $R_D(t)$ by an exponential decay from a high resistance (undoped) state to a low resistance state (doped) or vice versa:

$$R_D(t) = \begin{cases} V_D/I_{D,sat} + C\left(1 - e^{-\frac{t}{\tau_{off}}}\right) & \text{(turn-off)} \\ V_D/I_{D,sat} + Ae^{-\frac{t}{\tau_1}} + Be^{-\frac{t}{\tau_2}} & \text{(turn-on)} \end{cases}$$

where *A*, *B*, and *C* are constants. $I_{D,sat}$ is the expected saturation current, or the on-state current. τ_1, τ_2, and τ_{off} are the time constants associated with the transistor turn-on stage (which has two components as discussed in the main text), and the transistor turn-off stage. We demonstrated that the SPICE model could accurately reflect the transient asymmetry, with the time constants τ_1, τ_2, and τ_{off} being 0.7 s, 2 s, and 0.5 s, consistent with observations of faster device turn-off behavior. We also note that the parameters used for fitting here including solution resistance ($R_s \approx 1$ kΩ), polymer volume capacitance ($C_p \approx 2.4$ μF) and charge transfer resistance ($R_{ct} \approx 10$ kΩ) are all close to the actual physical values, verifying the proposed model captures the physics of OECT switching. Constants related to time-dependent resistance, namely, *A*, *B* and *C* all have values around 1000 in this specific example. We expect these values to vary with different polymers and channel geometry. All SPICE simulations were performed with LTSpice (freely available from Analog Devices).

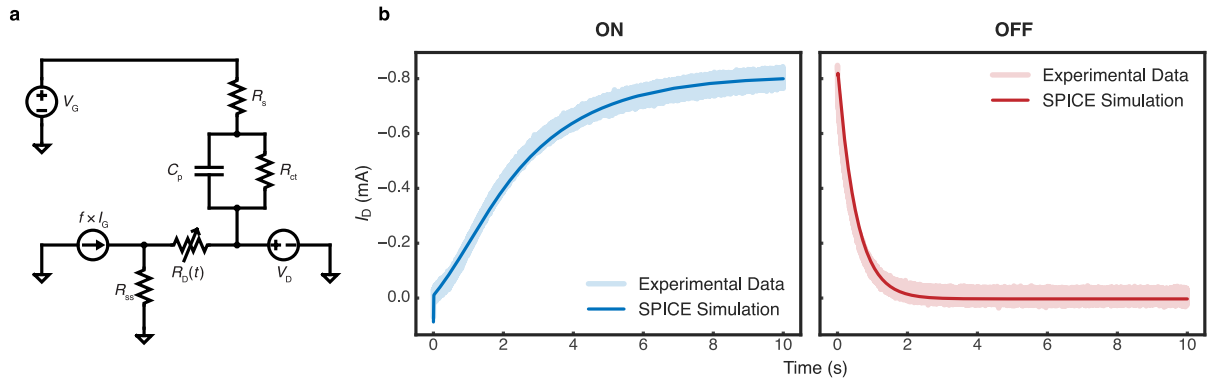

Figure B16. SPICE simulation of an accumulation mode OECT. a, LTSpice circuit model. Here, we used $f = 0.5$, though in this work the nature of f parameter is not under investigation. R_{ss} is used only for simulation purposes to measure the total source current, and it is generally a trivially low resistance (0.01 Ω). The other values are defined in the discussion above. b, Experimental data of an example accumulation mode P3HT OECT operates in 0.1 M KTFSI and the SPICE simulation results. ($W/L/d$ = 5 mm/100 µm/100 nm) The drain potential is fixed at −0.6 V while the on-potential is −0.6 V and off-potential is −0.2 V. We showed that the turn-on and turn-off kinetics are well represented by the circuit.

APPENDIX C: PHOTOLITHOGRAPY PROTOCOL

Appendix C describes the fabrication of OECT devices via photolithography. With Parylene C protecting layer, the fabricated OECT devices could have small and accurately defined channel active area. Photolithography fabricated OECTs could benefit applications like neuromorphic computing, in which a high ratio of number of transistors per area is desired.

Materials

All materials used in the photolithography protocol were kindly supplied by Washington Nano Fabrication (WNF) facility unless otherwise specified.

Methods

Scheme C1 shows the fabrication process of OECT devices with Parylene C protecting layer similar to a previously reported protocol.[130] NR9-3000PY negative resist (Futurrex, Inc.) was spin-coated on 4-inch cleaned glass wafers (University Wafer, Inc), followed by UV light exposure (ABM-SemiAuto-Aligner) and resist development using conditions based on the resist protocol **[Step 1 to Step 3]**. Oxygen plasma (Vision 320 RIE Mark II, Plasma Therm, Inc.) was applied for resist descum before evaporation. Metal deposition (10 nm titanium and 100 nm gold) was accomplished using e-beam evaporator (CHA Industries, Inc.) **[Step 4]**. After resist lift-off in acetone solution overnight, glass wafers were immersed into 0.5 vol% A-174 silane solution (Fisher Scientific) to improve Parylene C adhesion **[Step 5]**. Two layers of Parylene C (2 um/layer) were deposited using SCS Labcoter Parylene Deposition System. A 1% Micro-90 cleaning solution (Sigma-Aldrich) was spray-coated on first Parylene C layer as an anti-adhesive layer before depositing second Parylene C layer **[Step 6]**. The anti-adhesive layer assisted the later peel-

off step. AZ10 XT positive resist (EMD Performance Materials, Merck KGaA, Darmstadt) was then spin-coated on Parylene-protected wafers, followed by UV light exposure and development. Metal contacts and channel were exposed using Oxygen plasma (Vision 320 RIE Mark II, Plasma Therm, Inc.). The dry etching condition used was 100 mTorr (pressure), 300 W (power), 30 minute (time) and 40 sccm (flow rate) **[Step 7 to Step 9]**. The wafers were then diced into 15 mm × 15 mm chips using Disco Wafer Dicer (Disco, America).

Figure C1 shows the two photo masks used to define the gold and Parylene C patterns on the wafer. Photo masks were fabricated based on the WNF mask making procedure. In specific, positive resist and chromium coated glass was exposed using Heidelberg laser writer (20 mm Head), followed by resist developing, chromium etching and resist removing. Figure C2 shows the microscope image after step 3, step 5 and step 9. Figure C3 shows the wafer (left) and diced OECT chips (right). Figure C4 shows the peeled-off OECT chip after spin coating. The polymer layer is perfectly confined in the defined opening region. OECT devices with channel width (W) equal to 10 μm, 100 μm and 1000 μm and channel length (L) equals to 10 μm were successfully fabricated.

Results

The procedure was plausible and OECTs with desired dimension were successfully fabricated. Some optimizations were required in step 2 to 3 and step 8 to 9, as these steps determined the actual device dimension and the pattern alignment. In particular, channel length (10 μm) and Parylene C opening length (30 μm) would be affected most significantly if optimizations failed. However, one concern of this protocol is the second Parylene C layer might be peeled-off accidentally by dicing tape during wafer dicing step (account for ~ 77 % of the devices). Ideally,

the second Parylene C layer should not be peeled off until the polymer spin coating step is completed.

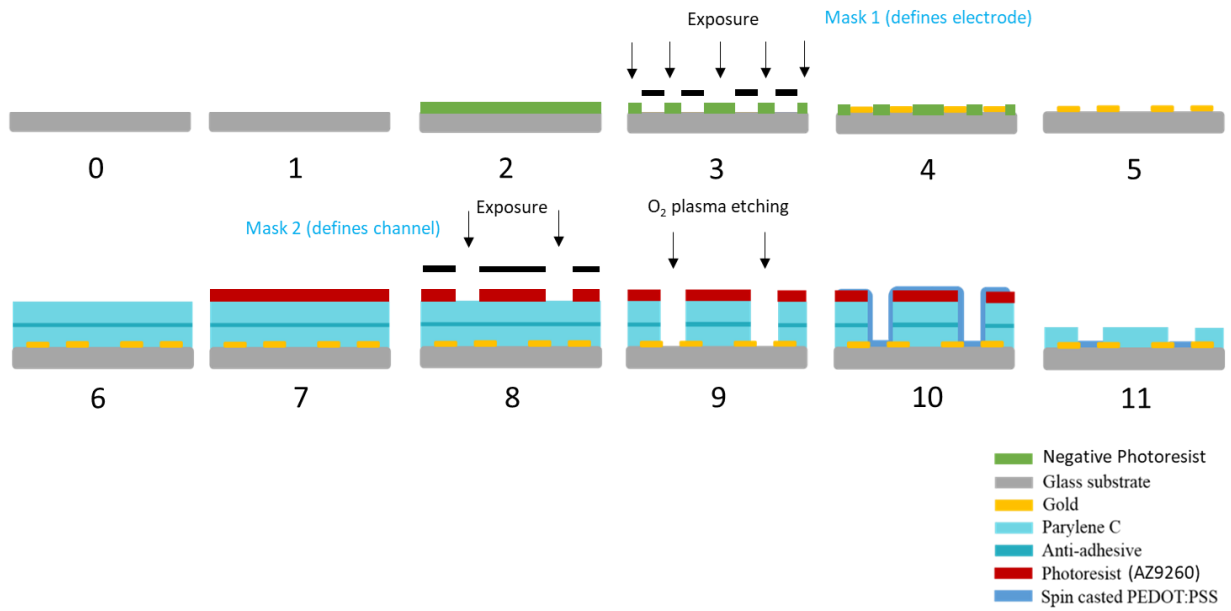

Scheme C1. Fabrication of OECT devices via photolithography based on Wustoni et al's procedure with some modifications.[130]

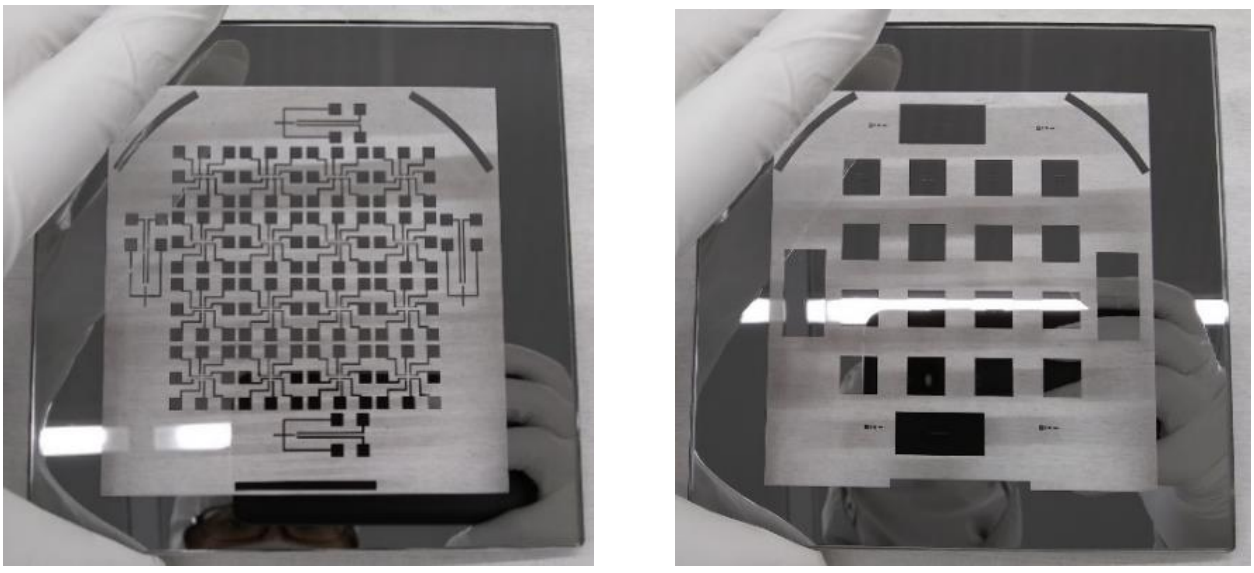

Figure C1. Two photo masks used for defining gold (left) and Parylene C patterns (right).

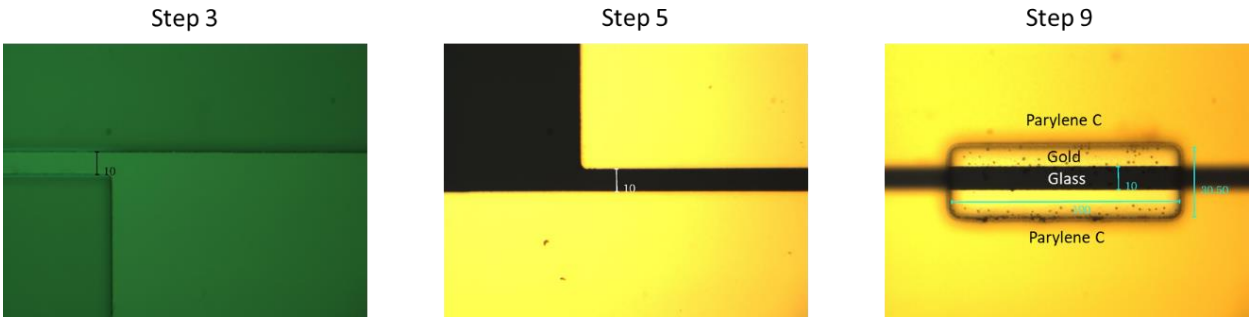

Figure C2. Microscope images after step 3, step 5, and step 9. The unit of the scale is μm.

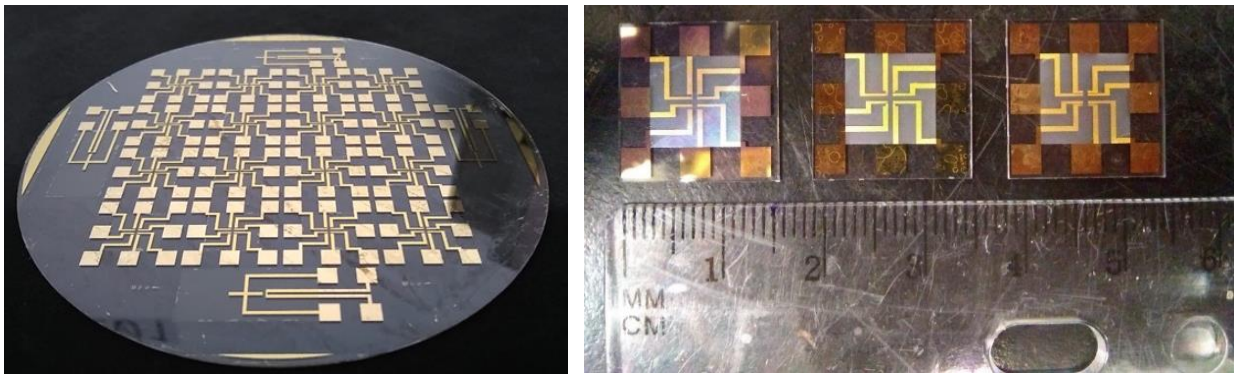

Figure C3. A wafer sample after step 9 (left) and the diced OECT chips (right).

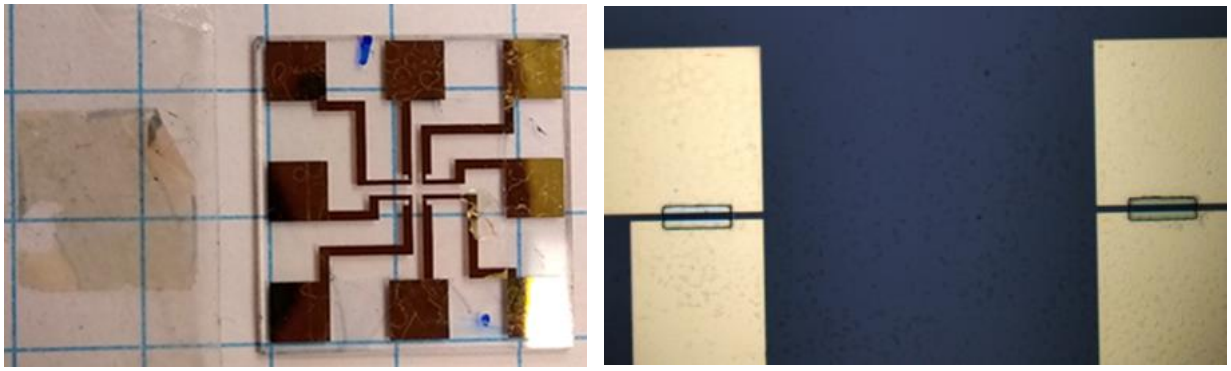

Figure C4. Peeled-off OECT chip after spin coating (left) and images near channel region under microscope after spin coating and peeled off (right). The channel width/length is 100 μm/10 μm. It is clear the PEDOT:PSS polymer is nicely confined in the defined area.

APPENDIX D: PRINTING PROTOCOL

Appendix D describes the fabrication of PEDOT:PSS based OECT devices using both Canon office printer and FUJIFILM Inkjet printer. Printed OECTs could benefit applications like point of care (POC) biosensors, in which low fabrication cost is desired.

Materials

PEDOT:PSS (Clevios P VP AI 4083 or Clevios PH 1000) solutions were purchased from Heraeus. Triton-X 100 was obtained from Sigma. PET substrate (PP2500) was obtained from 3M. PELCO® colloidal silver paste was obtained from Ted Pella Inc. Office printer (PIXMA MG3520) and black ink cartridge (PG-240 XL) were obtained from Canon. Inkjet printer (Dimatix DMP 2831) and cartridges were purchased from Fujifilm. Silver jet ink was acquired from Advanced Nano Products. Sodium chloride, Calcium chloride, Ethylene glycol and Dimethyl sulfoxide and all other solvents were obtained from Fisher Scientific. All chemicals were used as received without further purification.

Methods

Ink Preparation

The inks were prepared by adding different percent of DMSO, EG and Triton-X 100 (TX100) into commercial PEDOT:PSS solutions filtered with 0.45 um cellulose filter. DI water was added to adjust the viscosity of the final ink solution. The addition of DMSO or EG improved the film conductivity after annealing.[131] The addition of Triton-X 100 helped to overcome the surface tension of PET substrate.[16,132]

Cartridge Filling

For the Canon office printer, the sponge inside the black ink cartridge (Figure D.1) was taken out and both sponge and cartridge were thoroughly cleaned by DI water. The PEDOT:PSS ink (~3 mL) was then filled into the cartridge and the cartridge was installed back into the office printer. The printing process is the same as printing documents using Microsoft Office Word software. The resolution of the office printer is 600×600 dpi or 42 μm /pixel (dot) for black ink.

For FUJIFILM Inkjet printer, roughly 1 ml of Ink 15 was injected directly into the cartridge (Figure D1). The printing process was controlled by custom FUJIFILM software. The substrate temperature was maintained at 60 ℃ and the nozzle angle was fixed at 90°. The drop spacing used was 25 μm or 50 μm during fabrication and the resolution of the inkjet printer is 25 μm /pixel (dot). Three or six layers of PEDOT:PSS patterns were printed first. Silver circuits were then printed using the other cartridge. The whole devices were annealed under 100 ℃ on hotplate after printing for 30 minutes. Other detailed printing parameters were either followed the existing protocol in Washington Clean Energy Testbeds (WCET) or based on Wang et al's procedure.[133]

Additionally, we found that both cartridges broke after a period of time, which varied from several days to several weeks. This may be due to either nozzle clogging or print head damaged by the strong acidity of PEDOT:PSS solution. An alternative is to use P JET 700 (also PEDOT:PSS solution) from Heraeus instead, with little compromise of film conductivity (650 S/cm) compared to PH 1000 (850 S/cm with the addition of 5% DMSO).

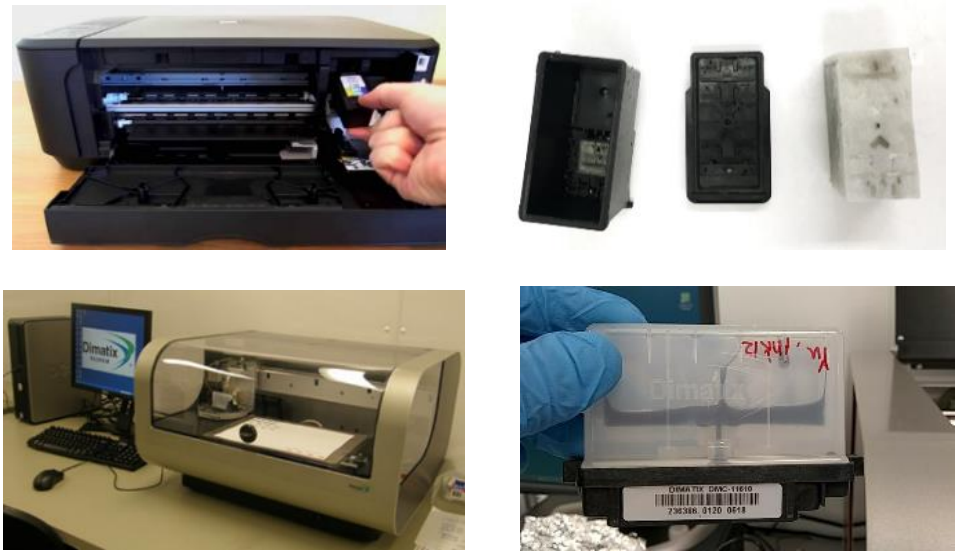

Figure D1. The photo of Canon office printer (upper left) and its cartridge (upper right). The image of FUJIFILM Inkjet printer (bottom left) and its cartridge (bottom right).

Results

Ink Characterization and Surface Treatment

The viscosity of ink solution was critical for successful printing process. Though viscosity between 2 cP and 30 cP was jettable for FUJIFILM inkjet printer, the optimal viscosity was 8 cP – 13 cP as recommended by the company. The ideal ink viscosity for Canon office printer should be around 5 cP – 10 cP based on its original black ink. We found that different PEDOT:PSS solution based inks behaved very differently (Figure D2), which may be due to different PEDTO to PSS ratio. According to Heraeus, the PEDOT to PSS ratio was 1:6 for P VP Al 4083 and 1:2.5 for PH 1000. P VP Al 4083 based ink solutions were close to Newtonian fluid, in which viscosity kept constant as shear rate increasing. The viscosity of Ink 5 and Ink 6 were about 8 cP, which was ideal for both printers. PH 1000 based ink solutions were close to pseudo plastic fluid, in which the viscosity decreased as shear rate increased. This made the choice of ink solution harder as it is unclear which viscosity under which specific shear rate should be compared.

Substrate surface treatment and surfactant in the ink are also crucial to the printing quality. A discrete pattern was obtained without the addition of surfactant, Triton-X 100 (Figure D3). Through contact angle measurements, the optimal surface treatment condition was determined to be adding 0.3% surfactant into ink solution and to treat the PET substrate with UV Ozone for 10 minutes before printing. And we successfully printed our devices with Ink 6 and Ink7 using Canon office printer, and Ink 13 using FUJIFILM inkjet printer. Though the viscosity of Ink 7 was higher than the ideal viscosity, we were still able to print out patterns using Canon office printer.

Planar OECT Designs

Aiming for point of care biosensing applications, several planar OECT devices were designed (Figure D4). The printed devices were shown in Figure D5. Design 1 was quickly eliminated as the redundant circuit merely increased the resistance. In Design 2, the silver paste was applied for lowering the contact resistance (R_C) between conducting polymer (CP) film and the metal electrode. Toward the goal of biosensor application in the future, in Design 3, flow channel-OECT was also accomplished by mounting the PET with acrylic gadget similar to the custom-built SPR flow channel system in the lab.

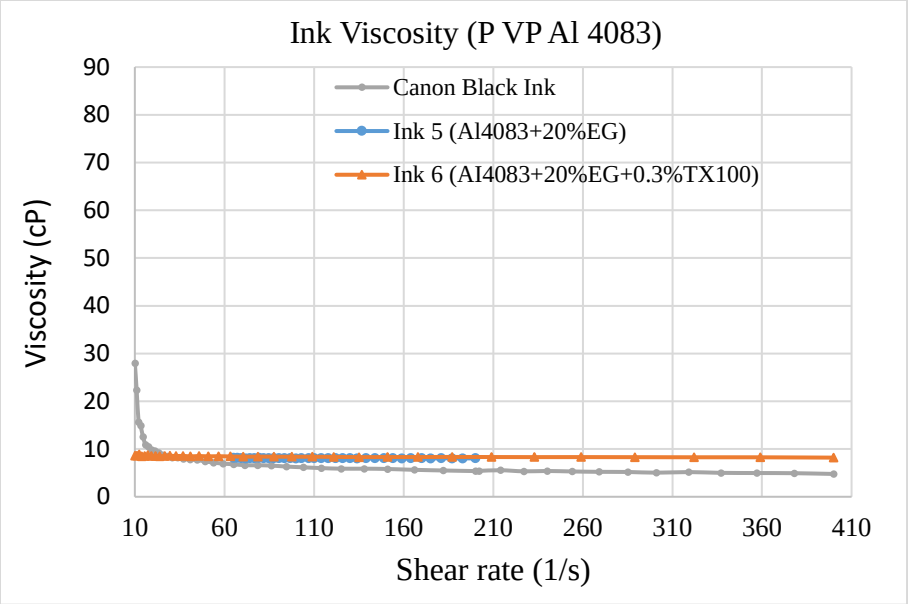

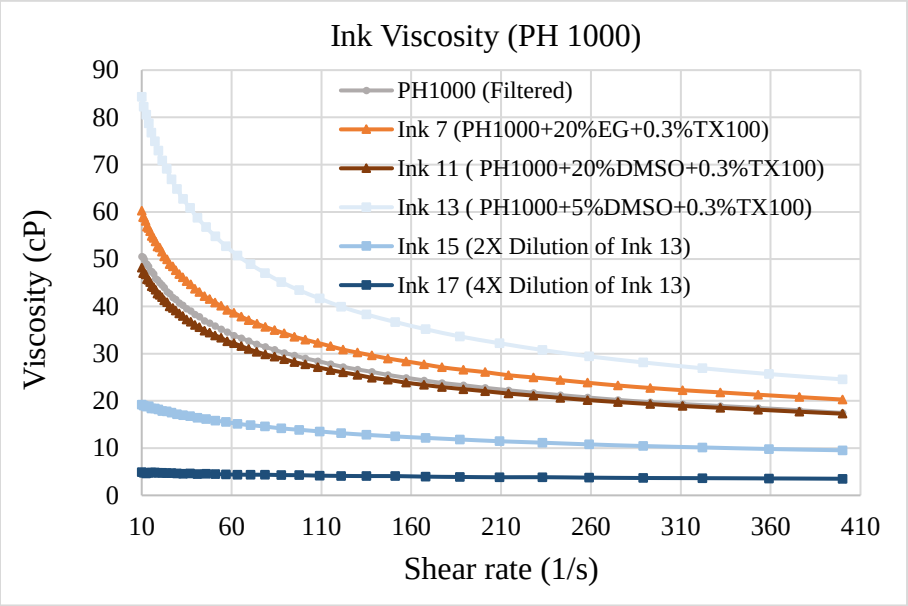

Figure D2. Viscosity measurements of PEDOT:PSS based inks.

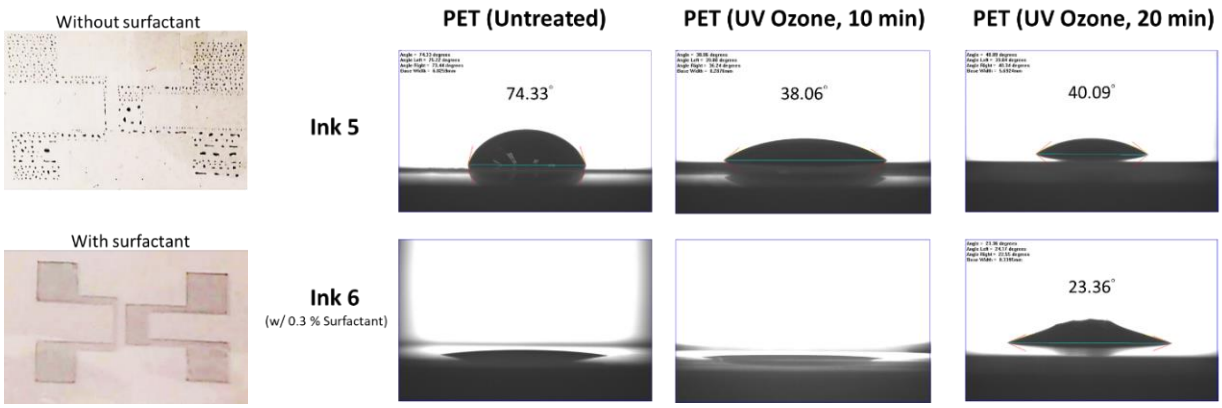

Figure D3. Printing results on PET (left) and contact angle measurements (right).

Table D1. Ink Composition

Ink (Vol %)	Unfiltered 4083	Filtered 4083	Unfiltered PH1000	Filtered PH1000	DI Water	DMSO	EG	Triton-X 100	Note
5	0	80	0	0	0	0	20	0	P VP AI 4083
6	0	80	0	0	0	0	20	0.3	
7	0	0	0	80	0	0	20	0.3	PH100 + Different EG%
8	0	0	0	90	0	0	10	0.3	
9	0	0	0	95	0	0	5	0.3	
10	0	0	0	99	0	0	1	0.3	
11	0	0	0	80	0	20	0	0.3	PH100 + Different DMSO%
12	0	0	0	90	0	10	0	0.3	
13	0	0	0	95	0	5	0	0.3	
14	0	0	0	99	0	1	0	0.3	
15	0	0	0	47.5	47.5	5	0	0.3	2X Dilution of Ink 13
16	0	0	0	47.5	47.5	0	5	0.3	2X Dilution of Ink 14
17	0	0	0	23.75	71.25	5	0	0.3	2X Dilution of Ink 15
18	0	0	0	23.75	71.25	0	5	0.3	2X Dilution of Ink 16

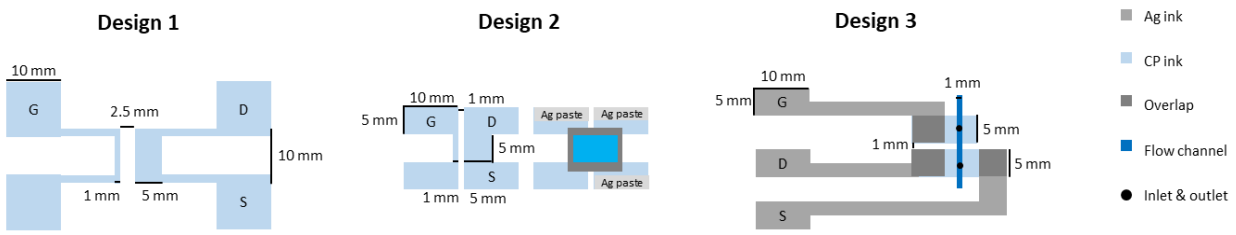

Figure D4. Designs of planar PEDOT:PSS based OECTs.

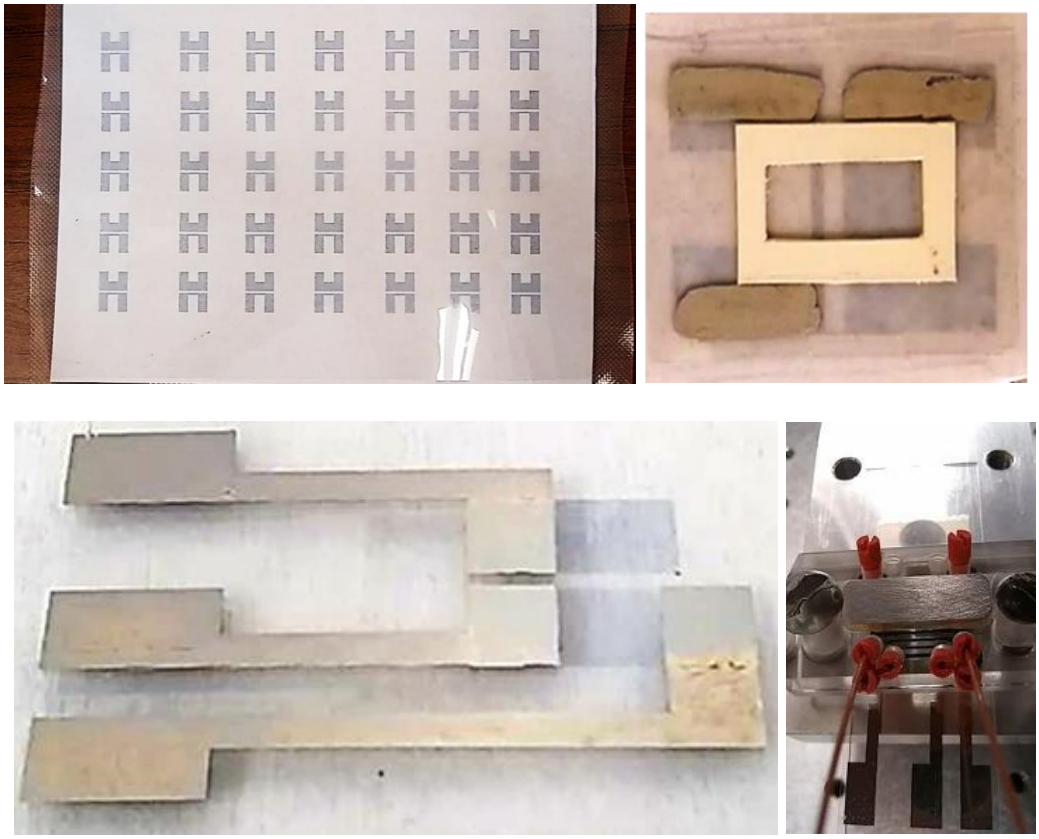

Figure D5. OECTs printed on A4-size PET by Canon office printer (upper left) and a single transistor with silver paste (to minimize contact resistance) and the white reservoir to hold the electrolyte (upper right). An OECT with silver electrode printed by Fujifilm printer (bottom left) and coupled with the flow channel (bottom right).

BIBLIOGRAPHY

1. Guo, K. *et al.* Rapid single-molecule detection of COVID-19 and MERS antigens via nanobody-functionalized organic electrochemical transistors. *Nat. Biomed. Eng. 2021 57* **5**, 666–677 (2021).
2. Bischak, C. G., Flagg, L. Q. & Ginger, D. S. Ion Exchange Gels Allow Organic Electrochemical Transistor Operation with Hydrophobic Polymers in Aqueous Solution. *Adv. Mater.* **32**, 2002610 (2020).
3. Pappa, A. M. *et al.* Organic Transistor Arrays Integrated with Finger-Powered Microfluidics for Multianalyte Saliva Testing. *Adv. Healthc. Mater.* **5**, 2295–2302 (2016).
4. Strakosas, X., Bongo, M. & Owens, R. M. The organic electrochemical transistor for biological applications. *J. Appl. Polym. Sci.* **132**, 41735 (2015).
5. Huang, W. *et al.* Vertical organic electrochemical transistors for complementary circuits. *Nature* **613**, 496–502 (2023).
6. Andersson Ersman, P. *et al.* All-printed large-scale integrated circuits based on organic electrochemical transistors. *Nat. Commun.* **10**, 1–9 (2019).
7. Harikesh, P. C. *et al.* Ion-tunable antiambipolarity in mixed ion–electron conducting polymers enables biorealistic organic electrochemical neurons. *Nat. Mater.* **22**, 242–248 (2023).
8. Sarkar, T. *et al.* An organic artificial spiking neuron for in situ neuromorphic sensing and biointerfacing. *Nat. Electron.* **5**, 774–783 (2022).
9. Fuller, E. J. *et al.* Parallel programming of an ionic floating-gate memory array for scalable neuromorphic computing. *Science.* **364**, 570–574 (2019).
10. Chen, S. E., Giridharagopal, R. & Ginger, D. S. Artificial neuron transmits chemical signals. *Nat. Mater.* **22**, 416–418 (2023).
11. Khodagholy, D. *et al.* High transconductance organic electrochemical transistors. *Nat. Commun.* **4**, 2133 (2013).
12. Van De Burgt, Y., Melianas, A., Keene, S. T., Malliaras, G. & Salleo, A. Organic electronics for neuromorphic computing. *Nat. Electron.* **1**, 386–397 (2018).

13. Paulsen, B. D., Tybrandt, K., Stavrinidou, E. & Rivnay, J. Organic mixed ionic–electronic conductors. *Nat. Mater.* **19**, 13–26 (2020).
14. Kroon, R. *et al.* Thermoelectric plastics: from design to synthesis, processing and structure–property relationships. *Chem. Soc. Rev.* **45**, 6147–6164 (2016).
15. Paudel, P. R., Dahal, D., Radha Krishnan, R. K., Skowrons, M. & Lüssem, B. Top-contact organic electrochemical transistors. *AIP Adv.* **12**, 45310 (2022).
16. Bihar, E. *et al.* A Disposable paper breathalyzer with an alcohol sensing organic electrochemical transistor. *Sci. Rep.* **6**, 2–7 (2016).
17. Ersman, P. A. *et al.* Screen printed digital circuits based on vertical organic electrochemical transistors. *Flex. Print. Electron.* **2**, 045008 (2017).
18. Donahue, M. J. *et al.* High-Performance Vertical Organic Electrochemical Transistors. *Adv. Mater.* **30**, 1–5 (2018).
19. Ohayon, D., Druet, V. & Inal, S. A guide for the characterization of organic electrochemical transistors and channel materials. *Chem. Soc. Rev.* 1001–1023 (2023).
20. Flagg, L. Q. *et al.* P-Type Electrochemical Doping Can Occur by Cation Expulsion in a High-Performing Polymer for Organic Electrochemical Transistors. *ACS Mater. Lett.* **2**, 254–260 (2020).
21. Laiho, A., Herlogsson, L., Forchheimer, R., Crispin, X. & Berggren, M. Controlling the dimensionality of charge transport in organic thin-film transistors. *Proc. Natl. Acad. Sci. U. S. A.* **108**, 15069–15073 (2011).
22. Huang, L. *et al.* Porous Semiconducting Polymers Enable High-Performance Electrochemical Transistors. *Adv. Mater.* **33**, (2021).
23. Flagg, L. Q., Giridharagopal, R., Guo, J. & Ginger, D. S. Anion-Dependent Doping and Charge Transport in Organic Electrochemical Transistors. *Chem. Mater.* **30**, 5380–5389 (2018).
24. Flagg, L. Q. *et al.* Polymer Crystallinity Controls Water Uptake in Glycol Side-Chain Polymer Organic Electrochemical Transistors. *J. Am. Chem. Soc.* **141**, 4345–4354 (2019).
25. Chen, S. E. *et al.* Impact of varying side chain structure on organic electrochemical transistor performance: a series of oligoethylene glycol-substituted polythiophenes †. *J. Mater. Chem. A* **10**, 10738–10749 (2022).
26. Rivnay, J. *et al.* Organic electrochemical transistors. *Nat. Rev. Mater.* **3**, 17086 (2018).

27. Zeglio, E. & Inganäs, O. Active Materials for Organic Electrochemical Transistors. *Adv. Mater.* **30**, 1800941 (2018).
28. Rivnay, J. *et al.* High-performance transistors for bioelectronics through tuning of channel thickness. *Sci. Adv.* **1**, 1400251 (2015).
29. Inal, S., Malliaras, G. G. & Rivnay, J. Benchmarking organic mixed conductors for transistors. *Nat. Commun.* **8**, 1767 (2017).
30. Savva, A. *et al.* Balancing Ionic and Electronic Conduction for High-Performance Organic Electrochemical Transistors. *Adv. Funct. Mater.* **30**, (2020).
31. Schmode, P. *et al.* High-Performance Organic Electrochemical Transistors Based on Conjugated Polyelectrolyte Copolymers. *Chem. Mater.* **31**, 5286–5295 (2019).
32. Szumska, A. A. *et al.* Reversible Electrochemical Charging of n-Type Conjugated Polymer Electrodes in Aqueous Electrolytes. *J. Am. Chem. Soc.* **143**, 14795–14805 (2021).
33. Moser, M. *et al.* Side Chain Redistribution as a Strategy to Boost Organic Electrochemical Transistor Performance and Stability. *Adv. Mater.* **32**, 2002748 (2020).
34. Li, P., Shi, J., Lei, Y., Huang, Z. & Lei, T. Switching p-type to high-performance n-type organic electrochemical transistors via doped state engineering. *Nat. Commun.* **13**, 5970 (2022).
35. Kim, Y. *et al.* Strain-Engineering Induced Anisotropic Crystallite Orientation and Maximized Carrier Mobility for High-Performance Microfiber-Based Organic Bioelectronic Devices. *Adv. Mater.* **2007550**, 1–10 (2021).
36. Tropp, J., Meli, D. & Rivnay, J. Organic mixed conductors for electrochemical transistors. *Matter* **6**, 1–33 (2023).
37. Bernards, D. A. & Malliaras, G. G. Steady-state and transient behavior of organic electrochemical transistors. *Adv. Funct. Mater.* **17**, 3538–3544 (2007).
38. Rivnay, J. *et al.* Organic electrochemical transistors for cell-based impedance sensing. *Appl. Phys. Lett.* **106**, (2015).
39. Li, P. & Lei, T. Molecular design strategies for high-performance organic electrochemical transistors. *J. Polym. Sci.* **60**, 377–392 (2022).
40. Easley, A. D. *et al.* A practical guide to quartz crystal microbalance with dissipation monitoring of thin polymer films. *J. Polym. Sci.* **60**, 1090–1107 (2022).
41. Wu, R., Matta, M., Paulsen, B. D. & Rivnay, J. Operando Characterization of Organic

Mixed Ionic/Electronic Conducting Materials. *Chem. Rev.* **122**, 4493–4551 (2022).

42. Xie, M. *et al.* Cycling stability of organic electrochemical transistors. *Org. Electron.* **117**, 106777 (2023).
43. Yamamoto, S. & Malliaras, G. G. Controlling the Neuromorphic Behavior of Organic Electrochemical Transistors by Blending Mixed and Ion Conductors. *ACS Appl. Electron. Mater.* **2**, 2224−2228 (2020).
44. Moia, D. *et al.* Design and evaluation of conjugated polymers with polar side chains as electrode materials for electrochemical energy storage in aqueous electrolytes. *Energy Environ. Sci.* **12**, 1349–1357 (2019).
45. White, H. S., Kittlesen, G. P. & Wrighton, M. S. Chemical Derivatization of an Array of Three Gold Microelectrodes with Polypyrrole: Fabrication of a Molecule-Based Transistor. *J. Am. Chem. Soc.* **106**, 5375–5377 (1984).
46. Bronstein, H., Nielsen, C. B., Schroeder, B. C. & McCulloch, I. The role of chemical design in the performance of organic semiconductors. *Nat. Rev. Chem.* **4**, 66–77 (2020).
47. Kim, S. M. *et al.* Influence of PEDOT:PSS crystallinity and composition on electrochemical transistor performance and long-term stability. *Nat. Commun.* **9**, 3858 (2018).
48. Wu, H. Y. *et al.* Influence of Molecular Weight on the Organic Electrochemical Transistor Performance of Ladder-Type Conjugated Polymers. *Adv. Mater.* **34**, 2106235 (2022).
49. Feng, K. *et al.* Organic Semiconductors Hot Paper Fused Bithiophene Imide Dimer-Based n-Type Polymers for High-PerformanceO rganic ElectrochemicalT ransistors. *Angew.Chem.* **133**, 24400– 24407 (2021).
50. Moser, M. *et al.* Ethylene Glycol-Based Side Chain Length Engineering in Polythiophenes and its Impact on Organic Electrochemical Transistor Performance. *Chem. Mater.* **32**, 6618–6628 (2020).
51. Bischak, C. G., Flagg, L. Q., Yan, K., Li, C. Z. & Ginger, D. S. Fullerene Active Layers for n-Type Organic Electrochemical Transistors. *ACS Appl. Mater. Interfaces* **11**, 28138–28144 (2019).
52. Ohayon, D. *et al.* Influence of Side Chains on the n-Type Organic Electrochemical Transistor Performance. *ACS Appl. Mater. Interfaces* **13**, 4253–4266 (2021).
53. Giridharagopal, R., Guo, J., Kong, J. & Ginger, D. S. Nanowire Architectures Improve Ion Uptake Kinetics in Conjugated Polymer Electrochemical Transistors. *ACS Appl. Mater.*

Interfaces **13**, 34616–34624 (2021).

54. Wu, X. *et al.* Ionic-Liquid Induced Morphology Tuning of PEDOT:PSS for High-Performance Organic Electrochemical Transistors. *Adv. Funct. Mater.* **32**, 2108510 (2022).
55. Moser, M. *et al.* Polaron Delocalization in Donor–Acceptor Polymers and its Impact on Organic Electrochemical Transistor Performance. *Angew. Chemie - Int. Ed.* **60**, 7777–7785 (2021).
56. Luo, X. *et al.* Designing Donor–Acceptor Copolymers for Stable and High-Performance Organic Electrochemical Transistors. *ACS Macro Lett.* **10**, 1061–1067 (2021).
57. Wang, Y. *et al.* The effect of the donor moiety of DPP based polymers on the performance of organic electrochemical transistors. *J. Mater. Chem. C* **9**, 13338–13346 (2021).
58. Schmode, P. *et al.* The Key Role of Side Chain Linkage in Structure Formation and Mixed Conduction of Ethylene Glycol Substituted Polythiophenes. *ACS Appl. Mater. Interfaces* **12**, 13029–13039 (2020).
59. Giridharagopal, R. *et al.* Electrochemical strain microscopy probes morphology-induced variations in ion uptake and performance in organic electrochemical transistors. *Nat. Mater.* **16**, 737–742 (2017).
60. Onorato, J. *et al.* Side Chain Engineering Control of Mixed Conduction in Oligoethylene Glycol-Substituted Polythiophenes. *J. Mater. Chem. A* **9**, 21410–21423 (2021).
61. Gruz, E. J -. *Discuss. Faraday Soc.* **1**, 11–19 (1947).
62. Chang, J. H., Park, J., Pak, Y. K. & Pak, J. J. Fitting improvement using a new electrical circuit model for the electrode-electrolyte interface. in *Proceedings of the 3rd International IEEE EMBS Conference on Neural Engineering* 572–574 (2007).
63. Kovacs Gregory T. A. Introduction to the theory, design, and modeling of thin-film microelectrodes for neural interfaces. in *Introduction to the theory, design, and modeling of thin-film microelectrodes for neural interfaces* (eds. D. A. Stenger & T. McKenna) 121–165 (Academic Press, 1994).
64. Thomas, E. M. *et al.* X-Ray Scattering Reveals Ion-Induced Microstructural Changes During Electrochemical Gating of Poly(3-Hexylthiophene). *Adv. Funct. Mater.* **28**, 1803687 (2018).
65. Guardado, J. O. & Salleo, A. Structural Effects of Gating Poly(3-hexylthiophene) through an Ionic Liquid. *Adv. Funct. Mater.* **27**, 1701791 (2017).

66. Savva, A. *et al.* Balancing Ionic and Electronic Conduction for High-Performance Organic Electrochemical Transistors. *Adv. Funct. Mater.* **30**, 1907657 (2020).
67. Huang, L. *et al.* Porous Semiconducting Polymers Enable High-Performance Electrochemical Transistors. *Adv. Mater.* **33**, 2007041 (2021).
68. Nicolini, T. *et al.* A Low-Swelling Polymeric Mixed Conductor Operating in Aqueous Electrolytes. *Adv. Mater.* **33**, 2005723 (2020).
69. Sauerbrey, G. Verwendung von Schwingquarzen zur W~igung diinner Schichten und zur Mikrow~igung*. *Zeitschrift fiir Phys.* **55**, 206–222 (1959).
70. Yamagata, H., Pochas, C. M. & Spano, F. C. Designing J-and H-aggregates through wave function overlap engineering: Applications to poly(3-hexylthiophene). *J. Phys. Chem. B* **116**, 14494–14503 (2012).
71. Murbach, M., Gerwe, B., Dawson-Elli, N. & Tsui, L. impedance.py: A Python package for electrochemical impedance analysis. *J. Open Source Software.* **5**, 2349 (2020).
72. Lin, P., Yan, F. & Chan, H. L. W. Ion-Sensitive Properties of Organic Electrochemical Transistors. *Appl. Mater. Interfaces* **2**, 1637–1641 (2010).
73. Ghittorelli, M. *et al.* High-sensitivity ion detection at low voltages with current-driven organic electrochemical transistors. *Nat. Commun.* **9**, 1441 (2018).
74. Gualandi, I. *et al.* Selective detection of dopamine with an all PEDOT:PSS Organic Electrochemical Transistor. *Sci. Rep.* **6**, 35419 (2016).
75. Xie, K. *et al.* Organic electrochemical transistor arrays for real-time mapping of evoked neurotransmitter release in vivo. *Elife* **9**, 1–19 (2020).
76. Khodagholy, D. *et al.* In vivo recordings of brain activity using organic transistors. *Nat. Commun.* **4**, (2013).
77. Go, G.-T., Lee, Y., Seo, D.-G. & Lee, T.-W. Organic Neuroelectronics: From Neural Interfaces to Neuroprosthetics. *Adv. Mater.* **34**, 2201864 (2022).
78. Tang, X., Shen, H., Zhao, S., Li, N. & Liu, J. Flexible brain-computer interfaces. *Nat. Electron.* **6**, 109–118 (2023).
79. Berggren, M., Głowacki, E. D., Simon, D. T., Stavrinidou, E. & Tybrandt, K. In Vivo Organic Bioelectronics for Neuromodulation. *Chem. Rev.* **122**, 4826–4846 (2022).
80. Gumyusenge, A., Melianas, A., Keene, S. T. & Salleo, A. Materials Strategies for Organic Neuromorphic Devices. *Annu. Rev. Mater. Res.* **51**, 1–25 (2021).

81. He, Y., Kukhta, N. A., Marks, A. & Luscombe, C. K. The effect of side chain engineering on conjugated polymers in organic electrochemical transistors for bioelectronic applications. *J. Mater. Chem. C* **10**, 2314–2332 (2022).
82. Kukhta, N. A., Marks, A. & Luscombe, C. K. Molecular Design Strategies toward Improvement of Charge Injection and Ionic Conduction in Organic Mixed Ionic-Electronic Conductors for Organic Electrochemical Transistors. *Chem. Rev.* **122**, 4325–4355 (2022).
83. Gentile, F. *et al.* A theoretical model for the time varying current in organic electrochemical transistors in a dynamic regime. *Org. Electron.* **35**, 59–64 (2016).
84. Faria, G. C., Duong, D. T. & Salleo, A. On the transient response of organic electrochemical transistors. *Org. Electron.* **45**, 215–221 (2017).
85. Paudel, P. R. *et al.* The Transient Response of Organic Electrochemical Transistors. *Adv. Theory Simul.* 2100563 (2022).
86. Ersman, P. A. *et al.* Screen printed digital circuits based on vertical organic electrochemical transistors. *Flex. Print. Electron.* **2**, 045008 (2017).
87. Butler, J. A. V. Studies in heterogeneous equilibria. Part II. - The kinetic interpretation of the nernst theory of electromotive force. *Trans. Faraday Soc.* **19**, 729–733 (1924).
88. Butler, J. A. V. Studies in heterogeneous equilibria. Part III. A kinetic theory of reversible oxidation potentials at inert electrodes. *Trans. Faraday Soc.* **19**, 734–739 (1924).
89. Erdey-Grúz, T. & Volmer, M. Zur Theorie der Wasserstoff Überspannung. *Zeitschrift für Phys. Chemie* **150A**, 203–213 (1930).
90. Giovannitti, A. *et al.* Controlling the mode of operation of organic transistors through side-chain engineering. *Proc. Natl. Acad. Sci. U. S. A.* **113**, 12017–12022 (2016).
91. Jia, H. *et al.* Engineering donor-acceptor conjugated polymers for high-performance and fast-response organic electrochemical transistors. *J. Mater. Chem. C* **9**, 4927–4934 (2021).
92. Giovannitti, A. *et al.* Energetic Control of Redox-Active Polymers toward Safe Organic Bioelectronic Materials. *Adv. Mater.* **32**, 1908047 (2020).
93. Wu, X. *et al.* All-Polymer Bulk-Heterojunction Organic Electrochemical Transistors with Balanced Ionic and Electronic Transport. *Adv. Mater.* **34**, 2206118 (2022).
94. Luo, X. *et al.* Designing Donor-Acceptor Copolymers for Stable and High-Performance Organic Electrochemical Transistors. *ACS Macro Lett.* **10**, 1061–1067 (2021).
95. Wang, Y. *et al.* Hybrid Alkyl-Ethylene Glycol Side Chains Enhance Substrate Adhesion

and Operational Stability in Accumulation Mode Organic Electrochemical Transistors. *Chem. Mater.* **31**, 9797–9806 (2019).

96. Chen, J. *et al.* Backbone coplanarity manipulation via hydrogen bonding to boost the n-type performance of polymeric mixed conductors operating in aqueous electrolyte. *Mater. Horizons* **10**, 607–618 (2023).
97. Shi, J. *et al.* Revealing the Role of Polaron Distribution on the Performance of n-Type Organic Electrochemical Transistors. *Chem. Mater.* **34**, 864–872 (2022).
98. Feng, K. *et al.* Cyano-Functionalized n-Type Polymer with High Electron Mobility for High-Performance Organic Electrochemical Transistors. *Adv. Mater.* **34**, 2201340 (2022).
99. Wang, Y. *et al.* n-Type Organic Electrochemical Transistors with High Transconductance and Stability. *Chem. Mater.* **35**, 405–415 (2022).
100. Guo, J. *et al.* Hydration of a Side-Chain-Free n-Type Semiconducting Ladder Polymer Driven by Electrochemical Doping. *J. Am. Chem. Soc.* **145**, 1866–1876 (2023).
101. Feng, K. *et al.* Fused Bithiophene Imide Dimer-Based n-Type Polymers for High-Performance Organic Electrochemical Transistors. *Angew. Chemie Int. Ed.* **60**, 24198–24205 (2021).
102. Sun, H. *et al.* Complementary Logic Circuits Based on High-Performance n-Type Organic Electrochemical Transistors. *Adv. Mater.* **30**, 1704916 (2018).
103. Bischak, C. G. *et al.* A Reversible Structural Phase Transition by Electrochemically- Driven Ion Injection into a Conjugated Polymer. *J. Am. Chem. Soc.* **142**, 7434−7442 (2020).
104. Gkoupidenis, P., Schaefer, N., Garlan, B. & Malliaras, G. G. Neuromorphic Functions in PEDOT:PSS Organic Electrochemical Transistors. *Adv. Mater.* **27**, 7176–7180 (2015).
105. Friedlein, J. T., Shaheen, S. E., Malliaras, G. G. & McLeod, R. R. Optical Measurements Revealing Nonuniform Hole Mobility in Organic Electrochemical Transistors. *Adv. Electron. Mater.* **1**, 1500189 (2015).
106. Tanase, C., Meijer, E. J., Blom, P. W. M. & De Leeuw, D. M. Unification of the Hole Transport in Polymeric Field-Effect Transistors and Light-Emitting Diodes. *Phys. Rev. Lett.* **9**, 216601 (2003).
107. Wu, R., Paulsen, B. D., Ma, Q. & Rivnay, J. Mass and Charge Transport Kinetics in an Organic Mixed Ionic−Electronic Conductor. *Chem. Mater.* **34**, 9699–9710 (2022).
108. Colucci, R., Barbosa, H. F. D. P., Günther, F., Cavassin, P. & Faria, G. C. Recent advances

in modeling organic electrochemical transistors. *Flex. Print. Electron.* **5**, 013001 (2020).

109. West, S. M. *et al.* Phenazine-Substituted Poly(benzimidazobenzophenanthrolinedione): Electronic Structure, Thin Film Morphology, Electron Transport, and Mechanical Properties of an n-Type Semiconducting Ladder Polymer. *Macromolecules* **56**, 2081–2091 (2023).
110. Zhang, Z. *et al.* Modulate Molecular Interaction between Hole Extraction Polymers and Lead Ions toward Hysteresis-Free and Efficient Perovskite Solar Cells. *Adv. Mater. Interfaces* **5**, 1800090 (2018).
111. Kiriy, A., Senkovskyy, V. & Sommer, M. Kumada Catalyst-Transfer Polycondensation: Mechanism, Opportunities, and Challenges. *Macromol. Rapid Commun.* **32**, 1503–1517 (2011).
112. Stokes, K. K., Heuzé, K. & McCullough, R. D. New phosphonic acid functionalized, regioregular polythiophenes. *Macromolecules* **36**, 7114–7118 (2003).
113. Lobez, J. M., Andrew, T. L., Bulović, V. & Swager, T. M. Improving the performance of P3HT-fullerene solar cells with side-chain-functionalized poly(thiophene) additives: A new paradigm for polymer design. *ACS Nano* **6**, 3044–3056 (2012).
114. Page, Z. A., Liu, F., Russell, T. P. & Emrick, T. Rapid, facile synthesis of conjugated polymer zwitterions in ionic liquids. *Chem. Sci.* **5**, 2368–2373 (2014).
115. Lameijer, L. N., Le Roy, J., Van Der Vorm, S. & Bonnet, S. Synthesis of O-1- O-6 Substituted Positional Isomers of d -Glucose-Thioether Ligands and Their Ruthenium Polypyridyl Conjugates. *J. Org. Chem.* **83**, 12985–12997 (2018).
116. Allcock, H. R. & Olmeijer, D. L. Polyphosphazenes functionalized with sulfone or sulfoxide groups: Synthesis, characterization, and possible polymer electrolyte applications. *Macromolecules* **31**, 8036–8046 (1998).
117. Cheng, S., Ye, S., Apte, C. N., Yudin, A. K. & Seferos, D. S. Improving the Kumada Catalyst Transfer Polymerization with Water-Scavenging Grignard Reagents. *ACS Macro Lett.* **10**, 697–701 (2021).
118. Wang, X. *et al.* Polythiophene with oligopeptide side chain: Preparation and nano-structure. *Supramol. Chem.* **25**, 842–847 (2013).
119. Tropp, J. *et al.* Revealing the Impact of Molecular Weight on Mixed Conduction in Glycolated Polythiophenes through Electrolyte Choice. *ACS Mater. Lett.* **5**, 1367–1375

(2023).

120. Flagg, L. Q. *et al.* In Situ Studies of the Swelling by an Electrolyte in Electrochemical Doping of Ethylene Glycol-Substituted Polythiophene. *ACS Appl. Mater. Interfaces* **14**, 29052–29060 (2022).
121. Page, Z. A., Duzhko, V. V. & Emrick, T. Conjugated thiophene-containing polymer zwitterions: Direct synthesis and thin film electronic properties. *Macromolecules* **46**, 344–351 (2013).
122. Hsu, C. H. & Mansfeld, F. Concernng the conversion of the constant phase element parameter Y0 into a capacitance. *Corrosion* **57**, 747–748 (2001).
123. Chang, B. Y. Conversion of a constant phase element to an equivalent capacitor. *J. Electrochem. Sci. Technol.* **11**, 318–321 (2020).
124. Nakano, K., Kaji, Y. & Tajima, K. Highly Sensitive Evaluation of Density of States in Molecular Semiconductors by Photoelectron Yield Spectroscopy in Air. *ACS Appl. Mater. Interfaces* **13**, 28574–28582 (2021).
125. Bässler, H., Kroh, D., Schauer, F., Nádaždy, V. & Köhler, A. Mapping the Density of States Distribution of Organic Semiconductors by Employing Energy Resolved–Electrochemical Impedance Spectroscopy. *Adv. Funct. Mater.* **31**, 2007738 (2021).
126. Hase, H., Berteau-Rainville, M., Charoughchi, S., Orgiu, E. & Salzmann, I. Doping-related broadening of the density of states governs integer-charge transfer in P3HT. *Appl. Phys. Lett.* **118**, 203301 (2021).
127. Friedlein, J. T., McLeod, R. R. & Rivnay, J. Device physics of organic electrochemical transistors. *Org. Electron.* **63**, 398–414 (2018).
128. Paudel, P. R., Tropp, J., Kaphle, V., Azoulay, J. D. & Lüssem, B. Organic electrochemical transistors-from device models to a targeted design of materials. *J. Mater. Chem. C* **9**, 9761–9790 (2021).
129. Lago, N. *et al.* A physical-based equivalent circuit model for an organic/electrolyte interface. *Org. Electron.* **35**, 176–185 (2016).
130. Wustoni, S. *et al.* An organic electrochemical transistor integrated with a molecularly selective isoporous membrane for amyloid-β detection. *Biosens. Bioelectron.* **143**, 111561 (2019).
131. Rivnay, J. *et al.* Structural control of mixed ionic and electronic transport in conducting

polymers. *Nat. Commun. 2016 71* **7**, 1–9 (2016).

132. Wu, J. & Lin, L. Y. Inkjet printable flexible thin-film NCQD photodetectors on unmodified transparency films. *IEEE Photonics Technol. Lett.* **26**, 737–740 (2014).

133. Wang, Y. *et al.* A highly stretchable, transparent, and conductive polymer. *Sci. Adv.* **3**, (2017).

VITA

EDUCATION

University of Washington

Ph.D. in Molecular Engineering (2023)

University of Washington

M.S. in Molecular Engineering (2020)

National Taiwan University

B.S. in Chemical Engineering (2016)

PUBLICATIONS

1. S. M. West, D. K. Tran, J. Guo, **S. E. Chen**, D. S. Ginger, S. A. Jenekhe. p-Type Semiconducting Ladder Poly(pyrrolobenzothiazine)s: Effects of N-Alkyl Side Chains on the Chain Conformation, Electronic Structure, and Charge Transport Properties (**In Preparation**)
2. J. Guo*, **S. E. Chen***, R. Giridharagopal, C. G Bischak, J. W. Onorato, K. Y., Z. Shen, C.-Z. Li, C. K Luscombe, D. S. Ginger. Why accumulation mode organic electrochemical transistors turn off much faster than they turn on. (**Submitted**)
3. **S. E. Chen**, R. Giridharagopal, D. S. Ginger. Artificial neuron transmits chemical signals. **Nat. Mater. 2023**.
4. S. M. West, D. K. Tran, J. Guo, **S. E. Chen**, D. S. Ginger, S. A. Jenekhe. Hydration of a side-chain-free n-type semiconducting ladder polymer driven by electrochemical doping. **Macromolecules 2023**.
5. J. Guo, L. Q. Flagg, D. K. Tran, **S. E. Chen**, R. Li, N. B. Kolhe, R. Giridharagopal, S. A. Jenekhe, L. J. Richter, D. S. Ginger. Hydration of a side-chain-free n-type semiconducting ladder polymer driven by electrochemical doping. **J. Am. Chem. Soc. 2023**.
6. **S. E. Chen**, L. Q. Flagg, J. W. Onorato, L. J. Richter, J. Guo, C. K. Luscombe, and D. S. Ginger. Impact of varying side chain structure on organic electrochemical transistor performance: a series of oligoethylene glycol-substituted polythiophenes. **J. Mater. Chem. A, 2022**.
7. E. Zheng, P. Jain, H. Dong, Z. Niu, **S. Chen**, S. Zhong, and Q. Yu. Chemical polymerization of hydroxymethyl and chloromethyl functionalized PEDOT: PSS. **ACS Appl. Polym. Mater. 2019**.

AWARDS AND HONORS

Graduate Fellowship (University of Washington Clean Energy Institute)	2020-2021
Presidential Award (National Taiwan University)	2012-2013